

PITTING CORROSION OF AA5005 SHEETS PRODUCED BY DC CASTING AND  
TWIN-ROLL CASTING TECHNIQUES

by

Öykü Gizem Zalođlu

Submitted to Graduate School of Natural and Applied Sciences  
in Partial Fulfillment of the Requirements  
for the Degree of Master of Science in  
Chemical Engineering


Yeditepe University

2019

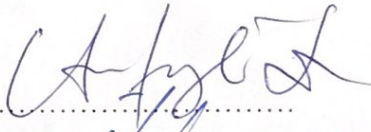
PITTING CORROSION OF AA5005 SHEETS PRODUCED BY DC CASTING AND  
TWIN-ROLL CASTING TECHNIQUES

APPROVED BY:

Assist. Prof. Dr. Levent Organ  
(Thesis Supervisor)  
(Yeditepe University)



Assoc. Prof. Dr. Ahmet Yılmaz  
(Yalova University)



Assist. Prof. Dr. Murat Oluş Özbek  
(Yeditepe University)



DATE OF APPROVAL: ...../...../2019

## ACKNOWLEDGEMENTS

First of all, I would like to express my special thanks and deepest appreciation to my supervisor, Assist. Prof. Dr. Levent Organ who gave me the opportunity to do my M.Sc. thesis. Due to his continuous support and his helpful advices, I managed to remain focused and stayed close to the essence of my work. Also, I record my sincere thanks to all the faculty members of the Department of Chemical Engineering for everything they have earned to me.

Secondly, thanks to my precious parents Deha and Şeyda for giving encouragement, enthusiasm and invaluable assistance to me. I am so grateful to have such parents who have guided me with absolute trust and love. Without all this, I might not be able to complete this study properly. Thirdly, I would like to thank my sister Ezgi. She is always been more than a sister for me. I know she is always with me and supportive in whatever I do in my life. I love her more than anything in my life.

Besides, I also like to thank my dearest girls; İlayda Acaroğlu Degitz, Sera Erkeçoğlu and Şelale Gülyuva Yanç. They have always supported me by giving me morale. They taught me that the distances do not matter in true friendship. I know that they are always as far away as a phone. I am very lucky to have them.

Last but not least I would like to thank my colleague Berk Gazioğlu. He is the best hearted person I have ever met in the world. Thanks to this project, I realized once again how valuable he was to me. I thank him very much for enduring all my moods, for knowing that he will be with me in all circumstances, for being in my life. I cannot imagine a life without him.

This study was supported by Scientific and Technological Research Council of Turkey, TÜBİTAK with the project no 315M232. The help of TUBITAK Marmara Research Center (TUBITAK-MAM) in examination of microstructures and examination of surfaces after immersion tests is acknowledged. The help of Erzurum Technical University in optical profilometry examinations is acknowledged.

## ABSTRACT

### PITTING CORROSION OF AA5005 SHEETS PRODUCED BY DC CASTING AND TWIN-ROLL CASTING TECHNIQUES

In this study, the pitting corrosion susceptibilities of AA5005 alloy sheets produced by the direct chill casting (DCC) technique and hot-rolling and the twin-roll casting (TRC) technique were investigated and compared. In order to compare the pitting corrosion resistances of the sheets, immersion tests, cyclic potential polarization (CPP) measurements, potentiostatic tests for the repassivation potential ( $E_{\text{repass}}$ ), galvanostatic cyclic polarization (GSCP) measurements, metastable pitting measurements under potentiostatic conditions and electrochemical noise measurements were performed in NaCl solutions at various concentrations. Depending on the microstructure studies, larger intermetallics were found in the DCC alloy. On the other hand, the number of intermetallics were higher in the alloy produced by the TRC technique. The immersion tests have shown that the DCC alloy have larger pits than the TRC alloy. From the CPP experiments, generally pitting potentials ( $E_{\text{pit}}$ ) of the DCC alloys were higher than TRC alloys, but the differences between the two alloy sheets were below 20 mV. Potentiostatic tests for the repassivation potential results have shown that, in general,  $E_{\text{repass}}$  potentials were more positive for the DCC alloys. From the GSCP measurements, breakdown ( $E_{\text{b}}$ ) potentials and protection potentials ( $E_{\text{prot}}$ ) of the DCC and the TRC alloy sheets were found to be close to each other. At 0.001 M concentration, the formation rate of metastable pits in the AA5005 sheet produced by the DCC technique was found to be higher than that of the TRC technique. The total charge of metastable pits in DCC alloys were generally higher. Depending on the electrochemical noise measurement, differences were found in the localized corrosion activity of the alloys of the two production techniques.

## ÖZET

### DOĞRUDAN SOĞUK DÖKÜM VE İKİZ MERDANE DÖKÜM TEKNİKLERİYLE ÜRETİLMİŞ ALÜMİNYUM 5005 ALAŞIM LEVHALARININ ÇUKURCUK KOROZYONU

Bu çalışmada, doğrudan soğuk döküm (DCC) ve sıcak hadde tekniği ve ikiz merdane döküm (TRC) tekniği ile üretilen AA5005 alaşımlı levhaların çukurcuk korozyon dayanımları incelenmiştir. Levhaların çukur korozyon dirençlerini, daldırma testleri, çevrimsel potansiyel polarizasyon (CPP) ölçümleri, yeniden dinginleşme potansiyeli ( $E_{\text{repass}}$ ), galvano-merdiven döngüsel polarizasyon (GSCP) ölçümleri için potansiyostatik testler, potansiyostatik koşullar altında yarı kararlı çukurcuk ölçümleri ve elektrokimyasal gürültü ölçümleri, NaCl çözeltilerinde çeşitli konsantrasyonlarda gerçekleştirilmiştir. Mikro yapı çalışmalarına bağlı olarak, DCC alaşımında daha büyük intermetalikler bulunmuştur. Öte yandan, TRC tekniğiyle üretilen alaşımlarda intermetalik sayısı daha yüksektir. Daldırma testleri DCC alaşımlarının TRC alaşımlarından daha büyük çukurlara sahip olduğunu göstermiştir. CPP deneylerine bağlı olarak, genellikle DCC alaşımlarının çukurcuk potansiyelleri ( $E_{\text{pit}}$ ) TRC alaşımlarından daha yüksektir, ancak iki alaşım arasındaki fark 20 mV'nin altındadır. Yeniden dinginleşme potansiyeli için yapılan potansiyostatik testlerin sonucunda, genel olarak,  $E_{\text{repass}}$  potansiyellerinin DCC alaşımları için daha pozitif olduğu görülmüştür. GSCP ölçümleri sonucunda DCC ve TRC alaşımlı levhaların bozulma ( $E_b$ ) koruma potansiyelleri ( $E_{\text{prot}}$ ) birbirine yakın bulunmuştur. 0.001 M konsantrasyonda, DCC tekniğiyle üretilen alüminyum alaşımında yarı kararlı çukurcukların oluşum oranının TRC tekniğinden daha yüksek olduğu bulunmuştur. DCC alaşımlarındaki yarı kararlı çukurcukların toplam yükü genellikle daha yüksektir. Elektrokimyasal gürültü ölçümü sonuçlarına bağlı olarak, iki üretim tekniğinin alaşımlarının yerel korozyon aktivitesinde farklılıklar görülmüştür.

## TABLE OF CONTENTS

ACKNOWLEDGEMENTS .....	iii
ABSTRACT.....	iv
ÖZET .....	v
LIST OF FIGURES .....	ix
LIST OF TABLES.....	xiii
LIST OF SYMBOLS/ABBREVIATIONS.....	xiv
1. INTRODUCTION.....	1
2. THEORETICAL BACKGROUND .....	2
2.1. CORROSION.....	2
2.1.1. Classification of Corrosion .....	2
2.1.2. Electrochemical Nature of Corrosion .....	4
2.1.2.1. Anodic and Cathodic Processes.....	4
2.1.2.2. Faraday’s Law .....	5
2.1.3. Factors Affecting the Corrosion .....	6
2.2. THERMODYNAMICS AND KINETICS OF CORROSION .....	7
2.2.1. Thermodynamics of Corrosion .....	7
2.2.1.1. Gibbs Free Energy .....	7
2.2.1.2. Standard Electrode Potential .....	8
2.2.1.3. Nernst Equation .....	9
2.2.2. Kinetics of Corrosion.....	10
2.2.2.1. Electrochemical Polarization.....	10
2.2.2.2. Mixed Potential Theory and Evans Diagram .....	10
2.2.2.3. Polarization Curves .....	13
2.3. PASSIVITY .....	14
2.4. PITTING CORROSION .....	16
2.5. PITTING CORROSION OF ALUMINIUM AND ITS ALLOYS.....	17
2.6. ALUMINIUM AND ITS ALLOYS.....	20
2.6.1. General Properties of Aluminium.....	20
2.6.2. Classifications of Aluminium .....	21

2.6.3.	Production of Aluminium and Its Alloys.....	23
3.	MATERIALS AND METHODS .....	26
3.1.	MATERIALS .....	26
3.1.1.	Electrochemical System for Electrochemical Tests.....	26
3.1.1.1.	Working Electrode (WE).....	27
3.1.1.2.	Reference Electrode (RE).....	28
3.1.1.3.	Counter Electrode (CE) .....	29
3.1.1.4.	Electrolytic Solution .....	30
3.1.1.5.	Potentiostat / Galvanostat .....	30
3.1.2.	Chemicals.....	31
3.2.	METHODS .....	32
3.2.1.	Microstructure Studies .....	32
3.2.2.	Immersion Tests.....	32
3.2.3.	Open Circuit Potential (OCP) Measurements.....	33
3.2.4.	Cyclic Potential Polarization (CPP) Measurements .....	33
3.2.5.	Potentiostatic Measurements (PSM) for Repassivation Potential ( $E_{\text{repass}}$ ) Determination .....	34
3.2.6.	Galvano-staircase Cyclic Polarization (GSCP) Measurements .....	35
3.2.7.	Metastable Pitting Corrosion Measurements under Potentiostatic Conditions.....	35
3.2.8.	Electrochemical Noise (EN) Measurements of Galvanic Couple .....	36
4.	RESULTS AND DISCUSSION.....	38
4.1.	MICROSTRUCTURE STUDIES .....	38
4.2.	IMMERSION TESTS .....	41
4.3.	OPEN CIRCUIT POTENTIAL (OCP) MEASUREMENTS .....	44
4.4.	CYCLIC POTENTIAL POLARIZATION (CPP) MEASUREMENTS .....	45
4.5.	POTENTIOSTATIC MEASUREMENTS (PSM) FOR REPASSIVATION POTENTIAL ( $E_{\text{REPASS}}$ ) DETERMINATION.....	58
4.6.	GALVANO-STAIRCASE CYCLIC POLARIZATION (GSCP) MEASUREMENTS .....	72
4.7.	METASTABLE PITTING CORROSION MEASUREMENTS UNDER POTENTIOSTATIC CONDITIONS.....	79

4.8. ELECTROCHEMICAL NOISE (EN) MEASUREMENTS OF GALVANIC  
COUPLE .....87

5. CONCLUSION .....96

REFERENCES .....98

APPENDIX A .....108

APPENDIX B .....115

APPENDIX C .....121





## LIST OF FIGURES

Figure 2.1. Half-cell reactions present simultaneously in corroding aluminium surface ....	12
Figure 2.2. Evans diagram for aluminium in neutral medium.....	13
Figure 2.3. Polarization curve of aluminium in a neutral solution at 25°C .....	14
Figure 2.4. Schematic representation of an anodic curve for a passive metal .....	15
Figure 2.5. Schematic representation of possible cathodic polarization curves; A, B and C .....	16
Figure 2.6. Schematic representation of various aluminium alloy combinations.....	21
Figure 2.7. Schematic representation of direct chill casting process.....	24
Figure 2.8. Schematic representation of twin-roll casting process .....	24
Figure 3.1. Image of the flat cell.....	26
Figure 3.2. Image of the test surface.....	28
Figure 3.3. Image of the reference electrode .....	29
Figure 3.4. Counter electrode .....	29
Figure 3.5. Potentiostat/galvanostat system.....	30
Figure 3.6. Image of the Faraday cage.....	31
Figure 3.7. Image of the three-electrode round cell. Working electrode 1 (WE 1) and the working electrode 2 (WE 2) are coupons of the same alloy. Seen between the two is the salt bridge tube containing the reference electrode. ....	37
Figure 4.1. Optical microscope images .....	38
Figure 4.2. SEM images after etching with HF .....	39
Figure 4.3. EDS analyses of intermetallics .....	40

Figure 4.4. SEM images after 7 days of immersion in 0.01 M NaCl solution .....	42
Figure 4.5. Optical profilometer images after 7 days of immersion in 0.01 M NaCl solution .....	43
Figure 4.6. OCP results for the AA5005 DCC and the TRC alloy.....	45
Figure 4.7. Schematic illustration of some quantities related to corrosion on a representative CPP curve .....	46
Figure 4.8. CPP curves in 1 M solution.....	47
Figure 4.9. CPP curves in 0.1 M solution.....	48
Figure 4.10. CPP curves in 0.01 M NaCl solution .....	49
Figure 4.11. CPP curves in 0.001 M solution.....	50
Figure 4.12. Normal cumulative probability plots of pitting potentials in 1 M, 0.1 M, 0.01 M and 0.001 M NaCl solutions .....	53
Figure 4.13. $E_{pit}$ versus chloride ion concentration graph .....	54
Figure 4.14. Representative pit image after a CPP experiment at 500x magnification.....	56
Figure 4.15. Optical images of working electrode after a CPP run .....	57
Figure 4.16. Image of the test surface after a CPP cut run .....	58
Figure 4.17. Applied potential versus time graph in 1 M NaCl solution.....	60
Figure 4.18. Applied potential versus time graph in 0.1 M NaCl solution.....	61
Figure 4.19. Applied potential versus time graph in 0.01 M NaCl solution.....	62
Figure 4.20. IR corrected potential, $E_{IR}$ , versus time graph in 0.01 M NaCl solution.....	63
Figure 4.21. Current density vs time graph for DCC alloy in 1 M NaCl solution.....	64
Figure 4.22. Current density vs time graph for TRC alloy in 1 M NaCl solution .....	65
Figure 4.23. Current density vs time graph for DCC alloy in 0.1 M NaCl solution.....	66

Figure 4.24. Current density vs time graph for TRC alloy in 0.1 M NaCl solution .....	67
Figure 4.25. Current Density vs time graph for DCC alloy in 0.01M NaCl solution .....	68
Figure 4.26. Current Density vs time graph for TRC alloy in 0.01 M NaCl solution .....	69
Figure 4.27. Representative current density graph for a GSCP measurement .....	73
Figure 4.28. Potential versus time graph for a TRC sample in 0.1 M NaCl solution .....	74
Figure 4.29. GSCP plot in 1 M NaCl solution.....	75
Figure 4.30. GSCP plot in 0.1 M NaCl solution.....	76
Figure 4.31. GSCP plot in 0.01 M NaCl solution.....	77
Figure 4.32. Metastable pitting corrosion measurement results in 0.01 M NaCl solution ..	81
Figure 4.33. Metastable pitting corrosion measurement results in 0.001 M NaCl solution	82
Figure 4.34. Zoom of current density data seen on Figure 4.32 in 0.01 M NaCl solution ..	83
Figure 4.35. Zooming of current density data seen on Figure 4.33 in 0.001 M NaCl solution .....	84
Figure 4.36. Schematic representation of a peak .....	85
Figure 4.37. Metastable Pitting Rate (MPR) versus potential graph .....	86
Figure 4.38. Total charge versus potential graph.....	87
Figure 4.39. EPN and ECN results collected after 10 minutes of immersion in 0.1 M NaCl solution.....	89
Figure 4.40. EPN and ECN results collected after 10 minutes of immersion in 0.01 M NaCl solution.....	90
Figure 4.41. EPN and ECN results collected after 24 hours of waiting at open circuit potential 0.1 M NaCl solution.....	91
Figure 4.42. EPN and ECN results collected after 24 hours of waiting at open circuit potential 0.01 M NaCl solution.....	91

Figure 4.43. Current PSD versus frequency graphs for DCC and TRC alloys.....95



## LIST OF TABLES

Table 2.1. Standard reversible potentials of some common reactions.....	8
Table 2.2. Some melting points with respect to degree of purity of aluminium .....	20
Table 2.3. Classifications of aluminium alloys.....	22
Table 3.1. Compositions of AA5005 DCC and TRC alloy sheets .....	27
Table 3.2. Applied activation potentials .....	35
Table 4.1. Size and number of intermetallic alloys .....	39
Table 4.2. $E_{\text{pit}}$ values and their standard deviations.....	51
Table 4.3. $E_{\text{repass}}$ and $i_{\text{pass}}$ values and their standard deviations.....	54
Table 4.4. Repassivation potential range results.....	70
Table 4.5. Optical microscopy results after potentiostatic measurements.....	71
Table 4.6. Results obtained from GSCP measurement.....	78
Table 4.7. Comparison of GSCP and CPP results .....	78
Table 4.8. Optical microscopy results done after the GSCP measurements.....	79
Table 4.9. Applied potentials ( $E_{\text{app}}$ ) depending on the pitting potentials .....	80
Table 4.10. Number of metastable pits .....	85

## LIST OF SYMBOLS/ABBREVIATIONS

$a$	Activity of each species
$E_{app}$	Applied potential
$E_{corr}$	Corrosion potential
$E_{IR}$	IR corrected potential
$E_{pit}$ or $E_{bd}$	Pitting or breakdown potential
$E_r$	Reversible potential under non-standard conditions
$E_r^0$	Standard reversible potential
$E_{ref}$	Reference electrode potential
$E_{repass}$ or $E_{prot}$	Repassivation or protection potential
$E_{zf}$	Potential for zero current flow
$f$	Frequency
$i$	Current density
$i_a$	Anodic current density
$i_{app}$	Applied current density
$i_c$	Cathodic current density
$i_{corr}$	Corrosion current density
$i_{crit}$	Critical current density
$i_{max}$	Maximum point of a peak
$i_{pass}$	Passive current density
$i_{vertex}$	Vertex current density
$I_a$	Anodic current
$I_c$	Cathodic current
$m$	Mass
$n$	Total electron numbers transported
$q$	Charge density
$Q_a$	Total anodic charge
$Q_c$	Total cathodic charge
$R$	Gas law constant
$R_{soln}$	Solution resistance

s	Stoichiometric coefficient of the species
t	Time
$t_i$	Starting time of a pit (pit initiation)
$t_f$	Finishing time (pit termination)
$\eta$	Overtoltage
$\rho$	Density of a metal
$\dot{m}$	Mass loss rate
$\Delta E_{\text{soln}}$ or $IR_{\text{drop}}$	Solution drop
$\Delta G$	Gibbs free energy change
$\Delta G^0$	Standard Gibbs free energy
$\Delta m$	Mass loss
A	The exposed area
AA	Aluminum alloy
CE	Auxiliary or counter electrode
CPP	Cyclic potential polarization
CPT	Critical pitting temperature
DCC	Direct chill casting
E	Potential
ECN	Electrochemical current noise
EN	Electrochemical noise
EPN	Electrochemical potential noise
F	Faraday's constant
FFT	Fast Fourier transform
GSCP	Galvano-staircase cyclic polarization
HER	Hydrogen evolution reaction
I	Current
LI or PI	Localization or pitting index
M	Atomic or molecular weight
MPR	Metastable pitting rate
NHE	Normal hydrogen electrode

OCP	Open circuit potential
ORR	Oxygen reduction reaction
PSD	Power spectrum density
PSM	Potentiostatic measurement
R	Gas law constant, solution resistance
RE or REF	Reference electrode
SCE	Saturated calomel electrode
SHE	Standard hydrogen electrode
SEM	Scanning electron microscopy
T	Temperature
TRC	Twin-roll casting
WE	Working electrode
ZRA	Zero resistance ammeter



## 1. INTRODUCTION

Corrosion is a reaction of a material with the interaction of the medium. Corrosion such as natural disasters, can also cause dangerous and expensive damages to everything such as automobiles, pipelines, bridges etc. According to the corrosion research done by United States, the direct cost of corrosion occurred on metals is \$276 billion per year [1]. Therefore, corrosion should be kept under controlled. There are several corrosion types such as uniform, pitting, crevice etc. In this study, pitting corrosion of AA5005 sheets produced by two techniques; direct chill casting (DCC) and twin-roll casting (TRC) were investigated. Differences were determined by several electrochemical measurements: open circuit potential, cyclic potential polarization, potentiostatic measurements for repassivation potential determination, galvanostatic cyclic polarization, metastable pitting corrosion measurements under potentiostatic conditions, electrochemical noise measurements and immersion tests.

In theoretical background section, basics of corrosion, thermodynamics and kinetics of it, the passivity and detailed information about aluminium and its alloys and the theory of DCC and TRC production techniques are explained. In the experimental section, materials that were used in the experiment and the methodologies of the experiments are given. Then, experimental results are presented and discussed in the results and discussion sections, respectively. Finally, conclusion of this study are given.

## **2. THEORETICAL BACKGROUND**

In this section, firstly basics of corrosion were explained. Secondly, thermodynamics and kinetics of corrosion were summarized. Then, passivity were discussed. Afterwards, pitting corrosion of aluminium and its alloys were explained. Then, general properties and classifications of aluminium alloys were described. Lastly, production methods of aluminium and its alloys were explained.

### **2.1. CORROSION**

Corrosion is the degeneration of a material such as metal or a metal alloy and its properties due to the interaction with its environment. Definition indicates that the changes in the material's property may weaken the metal itself. This leads to failures in the systems. The serious outcomes of the corrosion attacks have become a vital problem. Corrosion causes plant shutdowns, waste of valuable resources, loss or contamination of product, reduction in efficiency, costly maintenance, and expensive overdesign [2]. Therefore, it is needed to understand the causes and choose the right strategies to decrease it to minimum level.

Many of us are familiar with the corrosion from everyday life experiences, such as rusting of an iron fence or a steel rim of a wheel degeneration. However, some forms of corrosion cannot be seen by the naked eye. In the next section, forms of corrosion are explained in detail.

#### **2.1.1. Classification of Corrosion**

Corrosion types can be divided into several categories depending on different criteria. Before investigating these classifications, first of all some corrosion types should be explained. These are:

- **Uniform corrosion:** In uniform corrosion, entire surface of the metal or an alloy will corrode. Thus, the surface becomes thinner and finally it fails. This corrosion type is the most common one.

- Crevice corrosion: This is one type of a local corrosion which means that the surface of the metal or an alloy will corrode locally within cracks.
- Pitting corrosion: This is another localized corrosion type that occurs as holes on the surface of the metal or an alloy. This is the most challenging corrosion type because it may be hard to detect, predict and to overcome.
- Galvanic corrosion: It occurs when two separate metals or alloys are coupled in a corrosive medium. The less noble metal acts as an anode and the more noble one acts like a cathode.
- Intergranular corrosion: This localized corrosion type will occur in the grain boundaries or regions near the grain boundaries.
- Stress corrosion cracking: It means to a cracking due to the presence of tensile stress at the same time. During stress corrosion cracking, fine cracks progress while the metal or an alloy surface is not being deformed.

Depending on the visual examination, Dillon et al. [3] grouped forms of corrosion in three categories. Group I contains some corrosion types that can be identified easily by visual examination like uniform, crevice, pitting and galvanic corrosion. Group II involves other forms of corrosion that can be examined by using extra tools with visual examination such as erosion, cavitation, intergranular corrosion and dealloying. Other forms of corrosion that cannot be identified by visual examination are included in Group III such as cracking and high temperature attack.

On the other point of consideration, corrosion can be classified depending on the medium. Corrosion occurs in all environments; dry or wet conditions. Therefore, it can be categorized into two: Dry (or chemical) corrosion and wet (or electrochemical) corrosion.

Chemical (dry) corrosion takes place in the dry surface of a metal in the presence of atmospheric gases. It means that, a chemical reaction occurs between the metal surface and the gas such as oxygen, hydrogen etc. On the other hand, in electrochemical (wet) corrosion, there is a conductive aqueous medium. So, electrochemical reactions (anodic and cathodic reactions) take place on the electrode surface.

In this study, electrochemical corrosion of a specific aluminium alloy was studied in different concentrations of sodium chloride solutions. Accordingly, electrochemical nature of the wet corrosion is discussed in the following section.

## 2.1.2. Electrochemical Nature of Corrosion

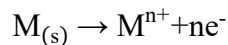
Electrochemical reactions appear when at least one material undergoes a net change in its valence. When the material loses its electron(s) it is called as an oxidation reaction and the material is called as anode. If the material gains electron(s) it is known as a reduction reaction and it is called as cathode. It should be noted that in corrosion processes, oxidation and reduction reactions occur on the same material.

### 2.1.2.1. Anodic and Cathodic Processes

When corrosion occurs, an anode loses its valence. Thus, oxidation number of that material increases. For example;



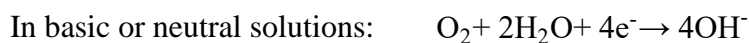
General equation of an anodic process is;



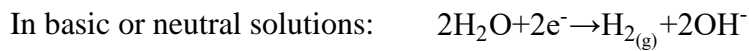
where M is a symbol of a metal and n is the valance charge of the metal.

On the other side of the system, a cathode gains an electron(s). Two common cathodic reactions are; oxygen reduction reaction (ORR) and hydrogen evolution reaction (HER). Depending on the pH of the system, these two common cathodic reactions can be written as follows:

Oxygen Reduction Reaction (ORR):



Hydrogen Evolution Reaction (HER):



### 2.1.2.2. Faraday's Law

Michael Faraday is the one who analysed the relationship between the charge passed through the substance and the oxidized/reduced amount of that substance. Faraday stated two laws:

- i. Amount of product formed is directly proportional to the charge passed (Faraday's first law).
- ii. There is a direct proportion to the masses of products formed and electrochemical equivalent weights of the products for a certain amount of charged transferred (Faraday's second law).

One equation combines these two as:

$$m = \frac{s M I t}{n F} \quad (2.1)$$

electrochemical equivalent weight is  $sM/nF$ . Generally, the electrode reaction has a stoichiometric coefficient equal to one. Thus, the term  $s$  in Equation 2.1 will be equal to one. It is important that, the Equation 2.1 could be used only under constant current processes. If the  $s$  term is omitted and dividing both sides to the unit area, then above equation becomes,

$$\Delta m = \frac{q M}{n F} \quad (2.2)$$

where  $\Delta m$  is the mass loss per unit area and  $q$  is the charge density (charge/area). When time derivative of the Equation 2.2 is taken, it gives the mass loss rate,  $\dot{m}$ , and its relation to the current density,  $i$  in mA/cm<sup>2</sup> is given as:

$$\dot{m} = \frac{i M}{n F \rho} \quad (2.3)$$

where  $\rho$  is the density of the metal with a unit of gram per cubic meter.

Understanding the distinction between the current,  $I$ , and the current density,  $i$  is essential. The current has a unit of amperes whilst the current density has the unit of amperes per unit area.

Note that in a closed system, electrons lost in oxidation reactions (at anodic locations) must be consumed in reduction reactions (at cathodic places). In other words, the total anodic charge,  $Q_a$ , must be equal to the total cathodic charge,  $Q_c$  [4–6].

In terms of charges; 
$$\sum_i Q_a = \sum_j Q_c \quad (2.4)$$

In terms of currents; 
$$\sum_i I_a = \sum_j I_c \quad (2.5)$$

Since the current density can be found as the current ( $I$ ) over the exposed area ( $A$ ):

$$i_i = \frac{I_i}{A} \quad (2.6)$$

One can write:

$$\sum_i i_a A_a = \sum_j i_c A_c \quad (2.7)$$

### 2.1.3. Factors Affecting the Corrosion

There are some crucial parameters that affect the corrosion and its rate. These factors can be divided in two major groups: (1) internal and (2) external.

Internal factors are the factors that caused by the material itself. Grain size, impurities, inclusions, stress, stability and surface roughness are some of the examples for the internal affecting factors. Furthermore, impurities in the material increases the rate of corrosion. For instance, Foroulis et al. [7] studied the effect of impurities in iron. They found that adding sulphur into an iron increases the corrosion rate.

External factors are factors related to the corroding environment such as concentration of an aggressive ion, temperature and pH. Temperature is one of the most important parameter affecting the corrosion rate. It is well known that the reaction rate and the temperature have a direct proportion. Corrosion processes are likewise. On the other hand, pH of the environment changes the electrochemical reactions on corroding material as written in the cathodic and anodic processes part (Section 2.1.2.1). Therefore, it is important to know and to stabilize all the parameters that may affect the electrochemical reactions while studying the corrosion.

## **2.2. THERMODYNAMICS AND KINETICS OF CORROSION**

### **2.2.1. Thermodynamics of Corrosion**

Thermodynamics in electrochemistry make it possible to determine whether a reaction can happen spontaneously which means without any external energy. In addition, it is the basis for many electrochemical measurements carried out in corrosion science and engineering. This section deals with the three major thermodynamic subjects in corrosion. These are: Gibbs free energy, standard electrode potential and the Nernst equation.

#### **2.2.1.1. Gibbs Free Energy**

In the nature, all spontaneous processes have a negative Gibbs free energy change ( $\Delta G$ ). This negativity stands for the stability of products is higher than the stability of reactants. In other words, the more negative  $\Delta G$  means the reaction has a higher tendency to go spontaneously.

When an electrochemical system is at equilibrium and under standard conditions; standard Gibbs free energy ( $\Delta G^0$ ) has a direct relationship between the standard reversible electrode potential across the cell ( $E_r^0$ ).

$$\Delta G^0 = -nFE_r^0 \quad (2.8)$$

Where  $F$  is the Faraday's constant and  $n$  is the total electron numbers transported in the reaction. Electrode potential is a specific parameter for each electrochemical reaction.

### 2.2.1.2. Standard Electrode Potential

In an electrochemical system, electrons are transferred from most negative side to the less negative one to reach the equilibrium. While electrons are going that way, current is flowing to the opposite direction. Potential difference between these two side of the electrochemical system is called as standard electrode potential. Standard stands for a certain temperature; 298 K and all species (reactants and products) are unit activity. Table 2.1 shows some common electrochemical reactions and their electrode potential. It is highlighted that the standard potential of the hydrogen evolution reaction (HER or NHE) is 0.00 Volts in literature.

Table 2.1. Standard reversible potentials of some common reactions

<b>Electrochemical reaction</b>	<b>Standard reversible potential, <math>E_r^0</math> (V vs. NHE)</b>
$\text{Au}^{3+} + 3e^- \leftrightarrow \text{Au}$	1.42
$\text{Cl}_2 + 2e^- \leftrightarrow 2\text{Cl}^-$	1.36
$\text{O}_2 + 4\text{H}^+ + 4e^- \leftrightarrow 2\text{H}_2\text{O}$	1.229
$\text{O}_2 + 2\text{H}_2\text{O} + 4e^- \leftrightarrow 4\text{OH}^-$	0.401
$\text{Cu}^{2+} + 2e^- \leftrightarrow \text{Cu}$	0.34
$2\text{H}^+ + 2e^- \leftrightarrow \text{H}_2$	0.000
$\text{Ni}^{2+} + 2e^- \leftrightarrow \text{Ni}$	-0.23
$\text{Fe}^{2+} + 2e^- \leftrightarrow \text{Fe}$	-0.44
$\text{Zn}^{2+} + 2e^- \leftrightarrow \text{Zn}$	-0.763

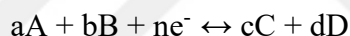


$\text{Al}^{3+} + 3\text{e}^- \leftrightarrow \text{Al}$	-1.706
$\text{Mg}^{2+} + 2\text{e}^- \leftrightarrow \text{Mg}$	-2.375
$\text{Na}^+ + \text{e}^- \leftrightarrow \text{Na}$	-2.712

For example, at 1.30 V vs. NHE, chlorine is reduced in the electrochemical reaction. At more positive potentials, chlorine is oxidized in a 1 molar solution of its salt.

### 2.2.1.3. Nernst Equation

Table 2.1 illustrates the reversible electrode potentials of some electrochemical reactions under standard conditions. When non-standard conditions occur, the Nernst equation calculates the reversible electrode potential of that reaction. Suppose the following electrochemical reaction:



where  $a$  and  $b$  is the stoichiometric coefficients of reactant A and B, respectively. Using the Nernst equation, the reversible potential under non-standard conditions can be calculated from activities as follows:

$$E_r = E_r^0 - \frac{R T}{n F} \ln \frac{a_C^c a_D^d}{a_A^a a_B^b} \quad (2.9)$$

where  $a$  is the activity of each species,  $E_r$  is the reversible electrode potential in Volts and  $E_r^0$  is the standard reversible potential. Remembering that when all the species are unit activity,  $\ln$  term becomes zero. Thus, reversible electrode potential equals to the standard reversible potential (Table 2.1). The Nernst equation is very useful in electrochemical analysis.

### 2.2.2. Kinetics of Corrosion

Thermodynamics explain the corrosion situation in terms of stability of reactants and products. It cannot be helpful for determining the rate of a reaction. But kinetics can do. Kinetics of corrosion gives information in terms of corrosion rates. Corrosion rate is a fundamental factor for determining the life span of materials. It can be analysed by using several techniques such as weight loss or gain but the most common ones are the electrochemical ones.

#### 2.2.2.1. Electrochemical Polarization

Electrochemical polarization is one of the most commonly used technique to determine the system corrosion rate. Polarization is the difference in potential of the electrode due to the flowing of a current.

The term overvoltage (denoted by  $\eta$ ) is the difference between the electrode potential ( $E$ ) and the electrode potential for zero current flow ( $E_{zf}$ ). Polarization degree can be determined by overvoltage and it is expressed as:

$$\eta = E - E_{zf} \quad (2.10)$$

Anodic polarization occurs when the electrode acts more anodic after the displacement of the electrode potential in the positive direction. Oppositely, cathodic polarization occurs when the electrode potentials move to the more negative direction. Thus, anodic overvoltage is positive while the cathodic overvoltage is negative.

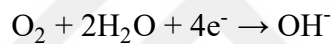
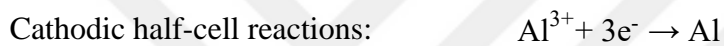
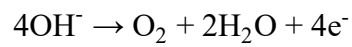
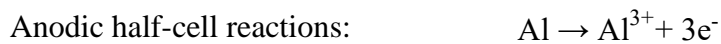
#### 2.2.2.2. Mixed Potential Theory and Evans Diagram

When corrosion occurs, both reactions (cathodic and anodic) occur on the same surface; surface of the material. Mixed potential theory indicates that the material should be at a potential where the total amount of cathodic current equals to the total amount of anodic current. If the test surface areas are equal, then it can be said in terms of current densities,  $i$ .

$$|i_a| = |i_c| \quad (2.11)$$

Where  $i_0$  stands for the exchange current density.

Now, consider a reaction of aluminium metal into a neutral solution. Four possible half-cell reactions are:



Electrochemical reaction which will proceed is oxygen reduction at cathodic site and aluminium oxidation at anodic site. These reactions take place at the same time on the corroding metal surface and they have their own electrode potentials and exchange current densities as shown in Figure 2.1. 0.401 V represents the reversible electrode potential of oxygen and -1.706 V represents the reversible electrode potential of aluminium metal.

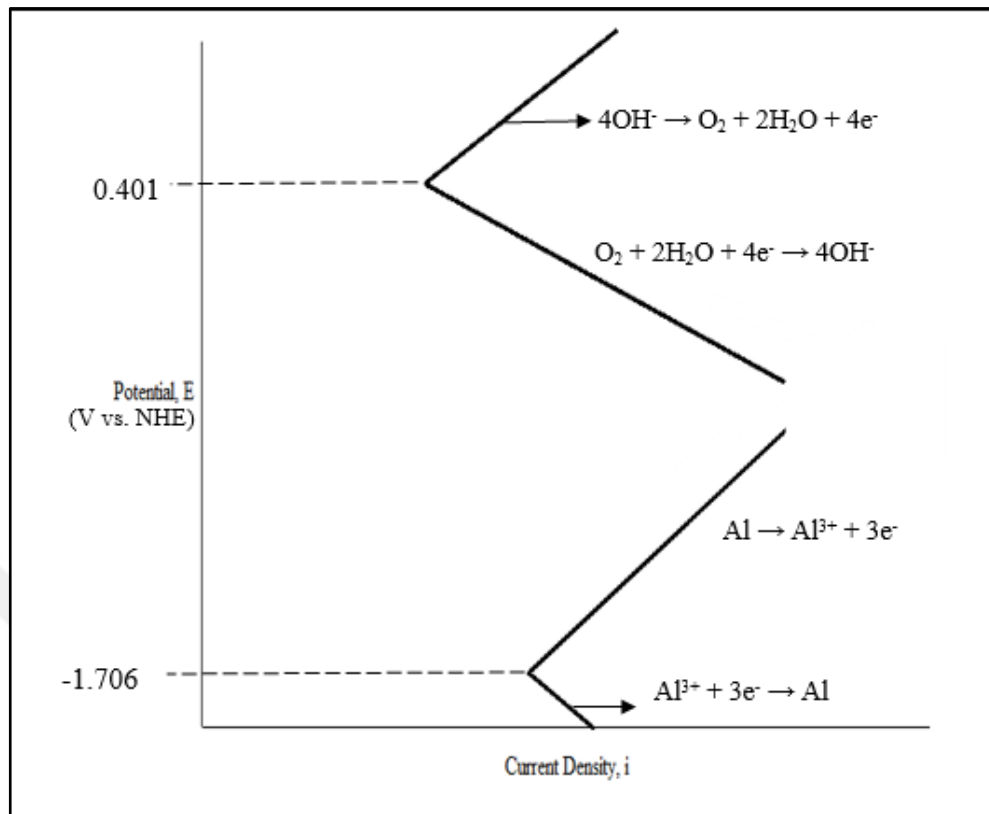


Figure 2.1. Half-cell reactions present simultaneously in corroding aluminium surface

However, the two half-cell electrode potentials cannot exist on the metal surface. They change the potential to a value as corrosion potential ( $E_{\text{corr}}$ ) according to mixed potential theory. Figure 2.2 which is called as Evans diagram shows the  $E_{\text{corr}}$  and corrosion current density ( $i_{\text{corr}}$ ) for the aluminium surface. At that point, the anodic rate,  $i_a$ , equals to the cathodic rate,  $i_c$ , in terms of charge is:

$$i_a = i_c = i_{\text{corr}} \quad (2.12)$$

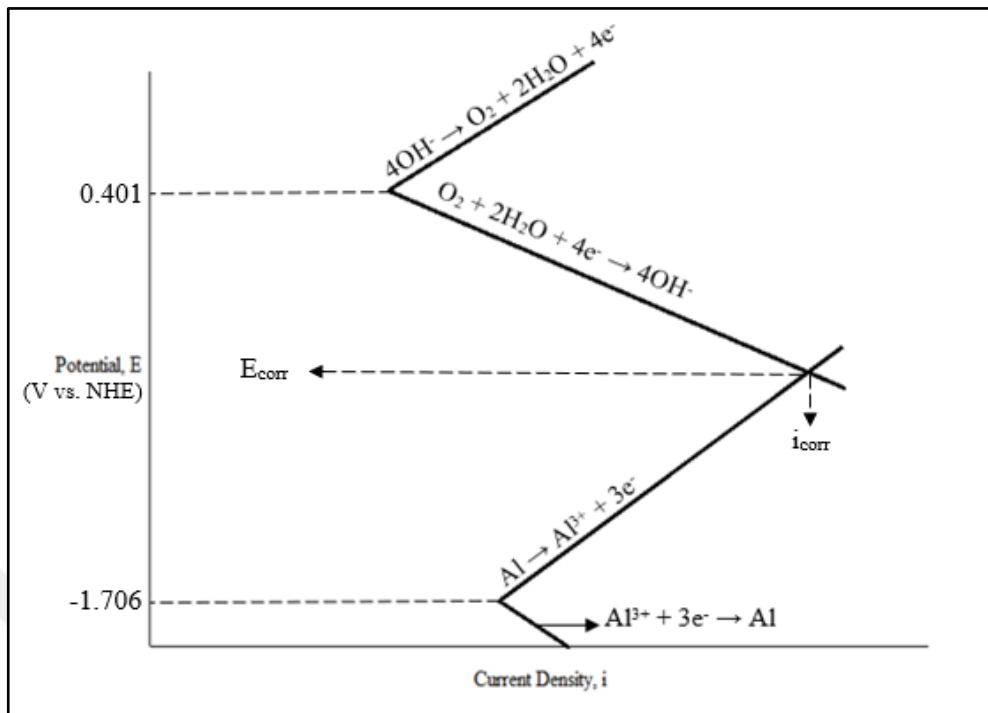


Figure 2.2. Evans diagram for aluminium in neutral medium

### 2.2.2.3. Polarization Curves

Polarization curve is a common measurement method in electrochemical corrosion studies. It uses the applied current density,  $i_{\text{app}}$  which could be found as the difference between the total anodic current densities and the total cathodic current densities at a specific potential. Figure 2.3 is a polarization curve of previous example; aluminium metal in a neutral medium. In the Figure 2.3, the solid line is the applied current (or current density) collected by a device which is called as a potentiostat/galvanostat.

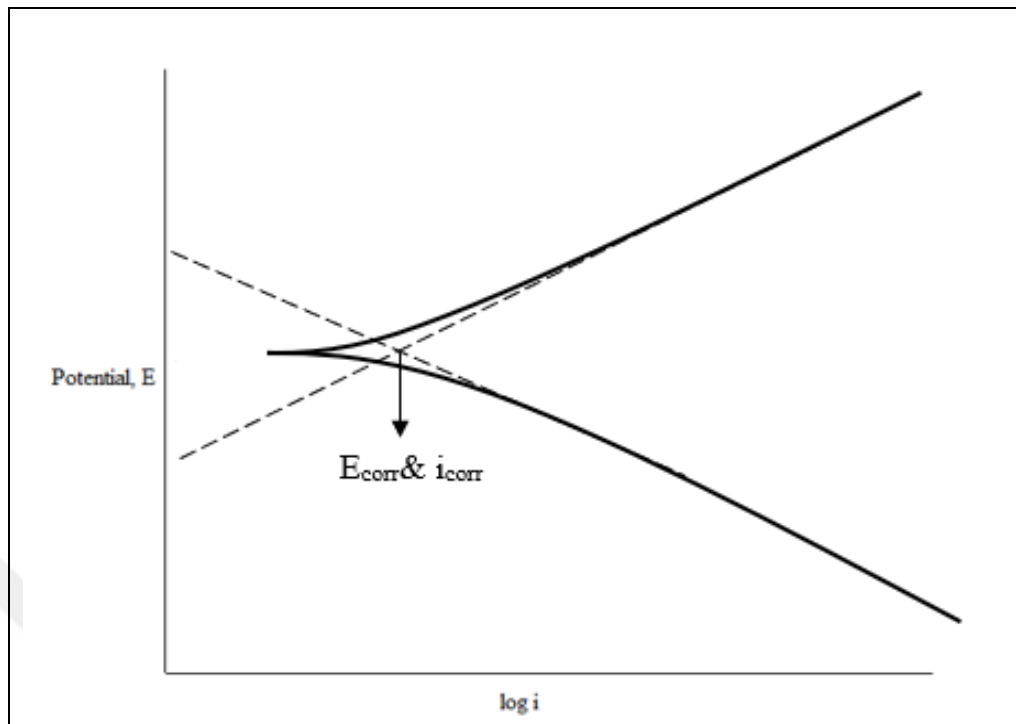


Figure 2.3. Polarization curve of aluminium in a neutral solution at 25°C

### 2.3. PASSIVITY

When a metal or an alloy resists to corrode at noble potentials in a given environment, it can be said that the metal or alloy is passive. It is also the characteristic property of all corrosion resistance alloys (such as aluminium, nickel, stainless steel etc.). Passivity is a critical factor for controlling the corrosion processes. Because, it is well established that mostly, passivity lowers the rate of corrosion [8].

Figure 2.4 shows a schematic description of an anodic curve for a passive metal. When the potential is increased in the anodic direction (active region) a potential, passivation potential,  $E_p$ , where the current density decreases by orders of magnitude (from the critical current density,  $i_{crit}$ , to a passive current density,  $i_{pass}$ ) is reached. This decline is due to the passive film formation on the metal surface. Above the passivation potential, the system is in the passive region and exhibits a very low current density. When the potential beyond the passive region increases, the passive film demolish and the current density increases in the transpassive region.

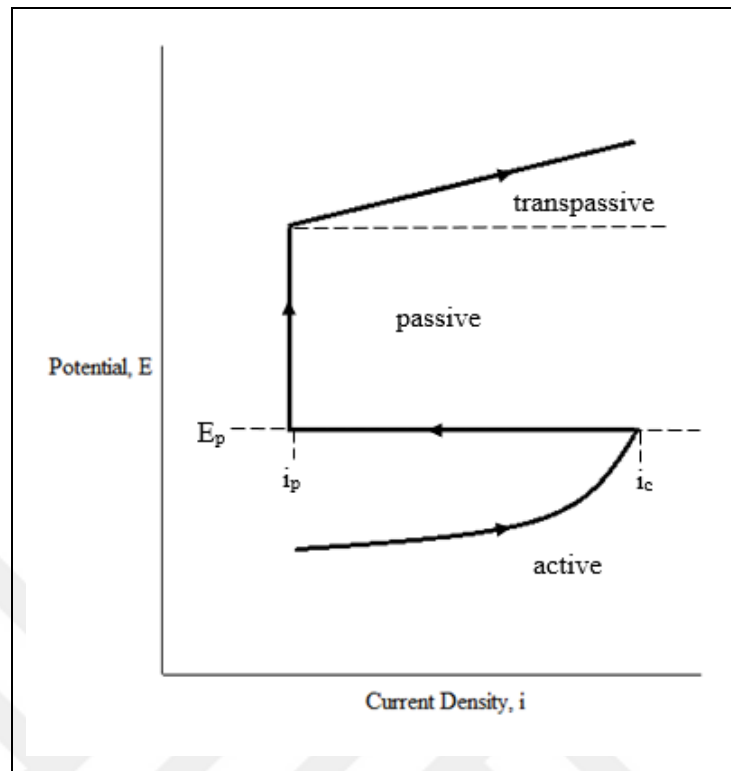


Figure 2.4. Schematic representation of an anodic curve for a passive metal

There are two types of passive film in the nature. One is called thin film and the other one is thick film. In thick film passivity, the material is protected through a visible thick film. This film could be an oxide layer or a salt film layer. For instance, surface of titanium is covered by a  $\text{TiCl}_3$  precipitate in hydrochloric acid solution [9]. In thin film passivity, the film that covers the surface of the material could not be seen by eyes. In brief, passivity and its characteristic parameters ( $E_p$ ,  $i_{\text{pass}}$  etc.) depend both on the exposed material and the environment.

$E_{\text{corr}}$  can be determined as the intersection of the anodic and cathodic polarization curves (Figure 2.2 and 2.3). As mentioned in previous sections, at this intersection point, cathodic and anodic reaction rates are equal. In order to determine the corrosion state of a system, the location of  $E_{\text{corr}}$  relative to passivation potential,  $E_p$ , is crucial. Figure 2.5 shows three possibilities can appear from the intersection of cathodic curves with the schematic passive anodic curve previously seen in Figure 2.4. When the cathodic curve A intersects the anodic curve;  $E_{\text{corr}}$  will be in the passive region. The metal will be protected (low corrosion rate). When the cathodic curve is like curve C;  $E_{\text{corr}}$  will be in the active region. It means that, the metal will dissolve uniformly (high corrosion rate). When the cathodic curve is like curve

B, unstable conditions are occurred because the  $E_{\text{corr}}$  locates in both active and passive regions.

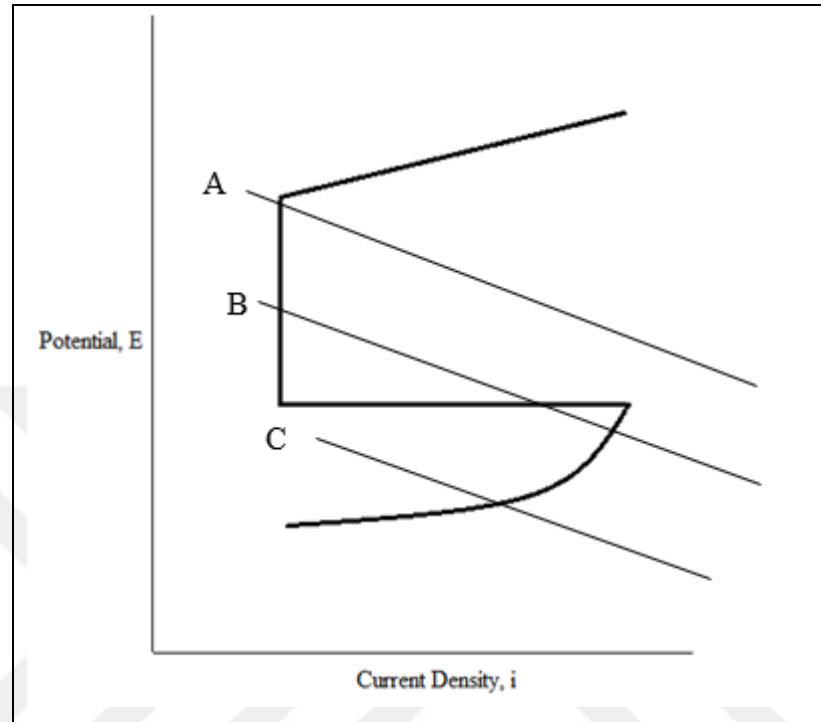


Figure 2.5. Schematic representation of possible cathodic polarization curves; A, B and C

## 2.4. PITTING CORROSION

Uniform or general corrosion corresponds to a corrosion attack to the whole surface of a material. However, in localized corrosion, corrosion attack occurs to a certain location (or locations) on the material surface. There are several types of localized corrosion in the nature such as; crevice, intergranular, galvanic etc. But the major form of it is pitting corrosion. It may occur in stagnant or slow-moving aqueous solutions. Pitting corrosion is much more dangerous than the uniform corrosion because it is hard to predict, understand the mechanism and overcome.

Depending on the book written by Roberge [10] pit may carry through four different stages:

- Initiation,
- Propagation,
- Termination and



- Re-initiation

Several models have been studied to define the pit initiation based on the passive film breakdown or on structural impurities or heterogeneities of a material. For instance, depending on the adsorption model which was first studied by Heusler and Fischer [11] localized adsorption of an aggressive ions such as chlorides activates dissolution of an oxide film at these local sites. Then the oxide film is thinning until a full removal is achieved and active dissolution begins. Moreover, some researchers have shown that the structural heterogeneities or defects also cause of the pit initiation [12][13]. In the propagation stage, there is a change in the environment. Anodic environment becomes more acidic while cathodic environment becomes more alkaline. Therefore, the rate of corrosion increases. A pit may stop due to increased internal resistance caused by either filling with corrosion products, filming of the cathode etc. If a pitted surface is dried out, it will prevent pitting corrosion. When rewetted, some of the pits may reinitiate. The solution's movement over a metal surface often reduces and may even prevent pitting. Localized corrosion of pitting is a complex issue and it is responsible for a lot of corrosion failures in engineering designs. Content of the material and the mechanism of the localized corrosion process should be carefully investigated and necessary precautions have to be taken.

## **2.5. PITTING CORROSION OF ALUMINIUM AND ITS ALLOYS**

Aluminium and its alloys can be used in different corrosive environments depending on their good heat and electrical conductivity, mechanical strength and such other properties. In nearly neutral solutions, it can be said that they are passive, because of the oxide film formation. In the other environments (acidic and alkaline media), they can be soluble [14,15]. Pits initiate at the most prone sites on a surface of metal, i.e. the weaknesses in the material surface. In pure aluminium, these often correspond to defects in the oxide film and grain boundaries [16,17]. Wang et al. [18] studied the electrochemical and the corrosion behaviour for the aluminium with a high purity in an alkaline environment. They found that the oxide layer on the surface of the aluminium becomes thinner because of the potassium chloride. Result of this, system open circuit potential (OCP) shifts in negative region. Another study was done with a pure aluminium by Doche et al. [19]. They concluded that in concentrated alkaline electrolyte, an initial alumina layer is dissolved rapidly. After

dissolution, breakdown of the film occurs. Then the film free aluminium surface dissolves with a higher rate. Which means that the aluminium corrosion rate increases.

Diversely, in aluminium alloys, the surface heterogeneities such as intermetallics and second phase particles are the weakness points that are tend to attack and initiate pits [20–23]. Intermetallics are the any class of substances composed of definite proportions of two or more elemental metals, rather than continuously variable proportions (as in solid solutions) [24]. Each intermetallic particle has its own electrochemical properties. Therefore, they have different level of intensity and types of attack. They can be categorized as anodic or cathodic depending on the matrix of the alloy. If the intermetallic particles have a more negative OCP value than that of bulk alloy these particles are anodic; if the particles have a more positive OCP; then they are cathodic. The OCP value of the all alloy results from the overall electrochemistry including the intermetallics, interactions between the intermetallics and the matrix, but the primarily determined from the solid solution [25,26]. Depending on the study done by Birbilis et al. [27] anodic intermetallic particles do not capable to maintain passive films, because the films are soluble in specific solution. Result of this, these particles are at risk for attack.

Electrochemical behaviour of the  $\delta$ AlFeSi,  $Al_3Fe$  and  $\alpha$ Al(Fe, Mn)Si in an alkaline environment was studied by Nişancıoğlu [28]. Nişancıoğlu concluded that  $Al_3Fe$  undergoes an aluminium dissolution when the applied potential,  $E_{app}$  is close to the  $E_{corr}$ . Another study was done by Zamin [29]. He found that the manganese increase in a solid solution results in the shift of the potential to the cathodic region for an aluminium-manganese alloys.

In this thesis, aluminium alloy 5005 produced by two different production techniques were studied. In 5xxx series, the main alloying element was magnesium. Magnesium is a frequently used alloying component in aluminium alloys. The electrochemical behaviour of second phase particles consist of magnesium plays a vital role while understanding the localized corrosion [30]. In literature, many researchers were studied the effect of magnesium to the pitting corrosion. Ren et al. [30] studied the mechanism of localized corrosion of aluminium alloys containing magnesium in neutrally aerated solution with a 3.5 per cent NaCl solution. They found that two different precipitates containing magnesium in aluminium alloy may occur; S and  $\beta$ . The  $\beta$  precipitate is anodic to the alloy. So, the anodic dissolution occurs on the surface of the alloy. Moreover, Ezuber et al. [31] studied the corrosion behaviour of AA5083 in seawater. They found that the surface of the alloy is not

very homogeneous and observed the irregularly shaped intermetallic particles. These particles have been also reported in literature such as Al(Si, Mg) and Al-Mg. They were also resulted that the high pitting susceptibility of the AA5083 is due to the high magnesium content. This content usually exhibits continuous intergranular  $\beta$  phase precipitates within the grains. These  $\beta$  phase precipitates are again anodic to alloy matrix; they enhance the susceptibility to localized attack to pitting corrosion. Pitting appears as a result of Al(Mn, Fe, Cr) particles being more cathodic than the alloy matrix [32–34]. Thus, since the intermetallic particles are the cause of the  $O_2$  reduction to occur as a choice on them, there is a localized increase of pH in the region around these particles, resulting in the dissolution of the oxide layer in the area surrounding the precipitate. This results in an intensive attack of the interfaces between the matrix and the precipitates resulting in the creation of hemispherical pits [35–37]. On the other hand, Engler et al. [38] studied the impact of copper additions on corrosion behaviour of different AA5xxx samples (AA 5182, AA5019, AA5023 and AA5754) in 5 per cent NaCl solution. They found that the AA5023 has comparable pitting corrosion resistance than other copper free alloys (AA5182 and AA5754).

In this work, localized corrosion behaviour of AA5005 produced by two different production techniques (DCC and TRC) were investigated. Studies on magnesium alloy sheet manufactured by TRC have been improved in latest years primarily for financial purposes. The alloy microstructure generated by these methods demonstrates significant variations in the distribution and the size of intermetallics owing primarily to variations in rate of solidification and thermal methods [39–41]. Oktay et al. [42] studied the corrosion behaviour of magnesium AZ31 alloy sheets produced by direct chill casting and twin-roll casting techniques. Results shows that the intermetallics size and distribution of them in the structure showed a dependency on the production method that utilized a powerful effect on their corrosion behaviour. Another research was done by Kurt et al. [43]. They compared the corrosion behaviour of TRC and DCC AA6061 and AA6082. It was found that the pitting potentials of aluminium alloys produced by DCC techniques are more positive than those of TRC ones. This is because of the nature of TRC technique causing segregation on the surface. Therefore, oxide layer is weakening in here and these regions are serving as preferred sites for pit initiation. Another study was done by Birol et al. [44]. They studied the corrosion behaviour of AA5754 and AA6061. They found that the pits were in a crystal form, alkaline type. These pits were initiated around AlFe particles in 5754 alloy.

Another critical factor that affect the pitting corrosion is temperature. Surface of the many materials will not form a pit below a specific temperature which is called a critical pitting temperature (CPT). Higher breakdown potentials are observed at lower temperatures. On the other hand, above the critical potential, pitting corrosion occurs [45]. According to Ernst et al. [46], there will be no pit formation below CPT because oxide passivation blocks the formation even in the most aggressive pit environment.

## 2.6. ALUMINIUM AND ITS ALLOYS

### 2.6.1. General Properties of Aluminium

Aluminium has become more and more widely used in the world due to its technical advantages. When the aluminium and its alloys are compared to iron and steel in consumption, increasing usage of them in the electric, chemical, medical, aircraft, construction and automotive industries in recent years increases the importance of aluminium day by day.

Aluminum is in the 3rd group of the periodic system, the atomic number is 13, the atomic weight is 26.97. Density of both liquid and solid aluminium decreases in proportion to the increasing degree of purity. It is reported that for 99.25 per cent purity of aluminium, density is 2.727 g/cm<sup>3</sup>, for 99.75 per cent purity of aluminium, density is 2.703 g/cm<sup>3</sup> [47]. The melting point of aluminium increases with increasing degree of purity. Table 2.2 shows some melting points are given in relation to the degree of purity reported by Beljajew et. al [47].

Table 2.2. Some melting points with respect to degree of purity of aluminium

Percent Al	Melting Point (°C)
99.2	657.0
99.5	658.0
99.6	658.7
99.97	659.8
99.996	660.14

Aluminium and its alloys conduct heat and electricity very well. Thermal conductivity is six times that of steel. In addition, the high purity aluminium is much softer and its mechanical strength is lower than the technical purity metal [47].

High corrosion resistance is another important feature of the aluminium. When aluminium surfaces are exposed to an atmospheric corrosion, a very thin, invisible oxide layer is formed which prevents further oxidation. If the degree of purity of aluminium decreases, the corrosion resistance decreases.

### 2.6.2. Classifications of Aluminium

Aluminium can be alloyed with other metals to improve both physical and mechanical properties of itself. Most commonly used alloying components are: copper (Cu), magnesium (Mg), silicon (Si), manganese (Mn) and zinc (Zn). Figure 2.6 shows the various aluminium alloy combinations.

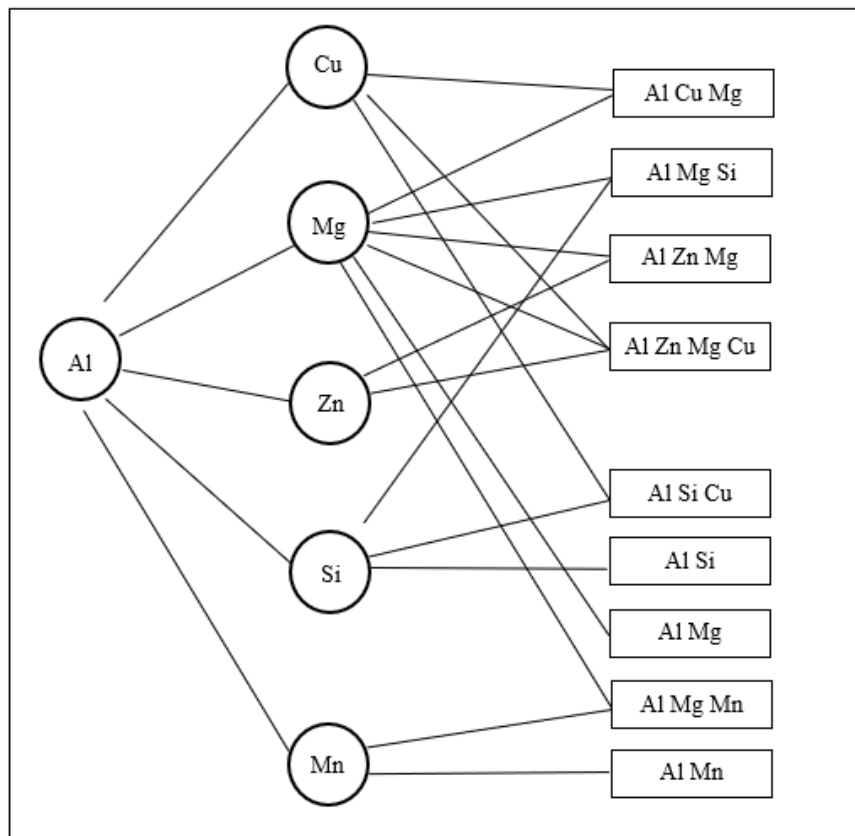


Figure 2.6. Schematic representation of various aluminium alloy combinations

While classifying the aluminium alloys, four-digit numbers are used after an abbreviation AA (aluminium alloy). First digit indicates the main alloying element in an alloy. Table 2.3 shows the classifications of aluminium alloys depending on the main alloying element.

Table 2.3. Classifications of aluminium alloys

1xxx	Al with minimum 99 percent purity
2xxx	Al-Cu alloy
3xxx	Al-Mn alloy
4xxx	Al-Si alloy
5xxx	Al-Mg alloy
6xxx	Al-Mg-Si alloy
7xxx	Al-Zn alloy
8xxx	Other alloys such as Al-Li, Al-Sn, Al-Zr

- 1xxx series: They include aluminium alloys containing aluminium with 99 per cent and higher purity. These alloys have perfect corrosion resistances, high thermal and electrical conductivity.
- 2xxx series: Main alloying element in these types of aluminium alloys is copper. This is one of the heat treatable aluminium alloy series. These alloys are generally used on aircraft wing surfaces and their tires.
- 3xxx series: Main alloying element is manganese. Addition of manganese increases the strength of the aluminium approximately 20 per cent. These alloys are generally used in on food cans, storage tanks and railway lines.
- 4xxx series: Main alloying element is silicon. If the necessary amount of silicon is added, melting point of the aluminium decreases without ant brittleness. Thus, these alloys are used as a welding wire.
- 5xxx series: Main alloying element in 5xxx series is magnesium. Addition of magnesium, increases the corrosion resistance of an aluminium with a higher strength. They have good welding ability. Therefore, they are mainly used in ships, crane parts and automotive industry. In this study, AA 5005 is used. The chemical composition of the alloy is given in material part.

- 6xxx series: These alloys include both silicon and magnesium. Result of this, heat treatment can be applied to these alloys. They have similar strength with 2xxx and 7xxx series but, 6xxx series are much better in formability, weldability, machinability and corrosion resistance. These alloys are used in architecture applications.
- 7xxx series: Main alloying element is zinc with a 1 to 8 per cent. Addition small amount of magnesium brings the heat treatment property of the alloy. These alloys have the highest strength than the other aluminium alloys.
- 8xxx series: When the other element(s) is added into the aluminium, it can be categorized as 8xxx series.

### 2.6.3. Production of Aluminium and Its Alloys

There are two main methods in the production of aluminium sheets [48]. These are:

- Traditional method: direct chill (DCC) casting
- Continuous sheet casting
  - Continuous thin slab casting with Hazelett method
  - Twin-roll continuous sheet casting (TRC)

In this thesis, two types of AA5005 produced by two different techniques (DCC and TRC) were studied. Therefore, production of aluminium by DCC and TRC techniques will be explained in detail.

Direct chill casting is the traditional technique of aluminium sheet production (Figure 2.7). Molten aluminium at about 700 °C is poured into a mold that is about 150 mm deep to form an ingot [49]. The mold has a water jacket for fastening the solidification rate. The cooling provides a solidified shell around the molten core of the ingot. As the bottom block is lowered and more molten aluminium is poured in, a large ingot is formed. The surface is further cooled by spraying water. Produced ingots have a rectangular shape, over 9 m long, 2300 mm wide and over 760 mm thick. After the casting of ingots, they are scalped with the aim of creating high quality surfaces for rolling. They are then preheated and homogenised. Subsequently, the desired plate thickness and dimensions are achieved by hot rolling and cold rolling.

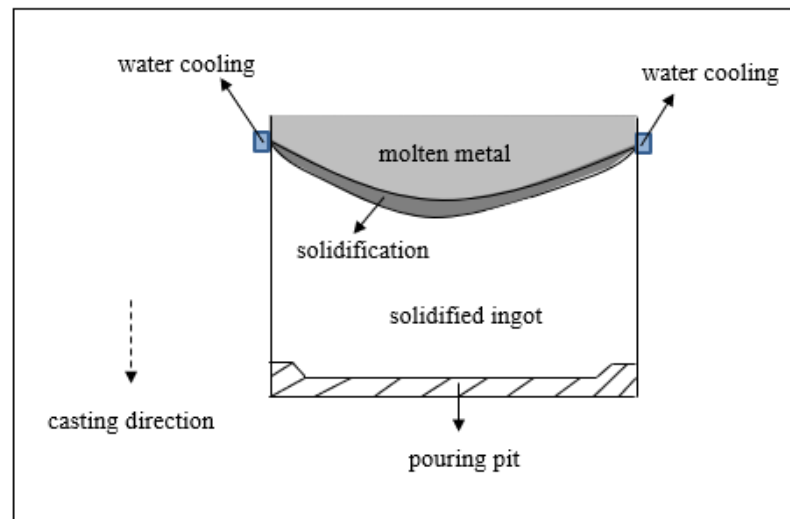


Figure 2.7. Schematic representation of direct chill casting process

The advantage of DCC casting is that it produces a homogeneous structure in terms of grain size, composition, mechanical properties and casting cavity throughout the entire ingot [50].

TRC is one of the continuous casting techniques and aluminium melt is not cast into a mold. Instead, the aluminium melt is directed to the space between two cold rollers rotating in the opposite direction (Figure 2.8). As a result of rapid cooling and pressing between the rollers, a 5-10 mm thick plate is obtained. This plate is then thinned to the desired thickness by cold rolling.

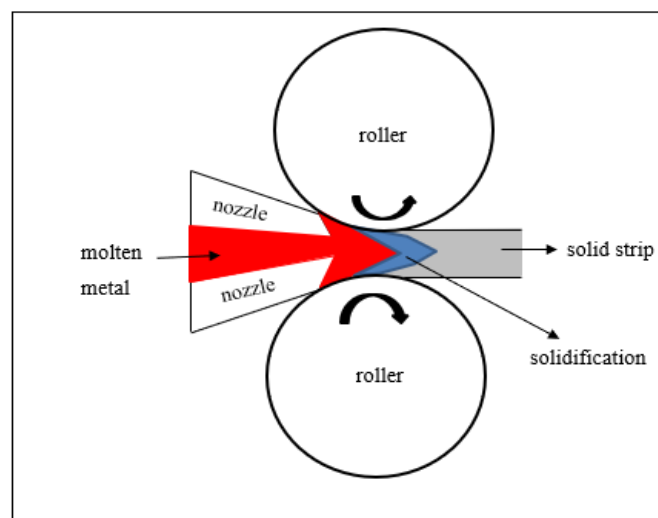


Figure 2.8. Schematic representation of twin-roll casting process



In both DCC and TRC plate production, annealing process can be performed according to the desired physical properties and hardness. In the final stage, the material is rolled or cut into rectangular plates. DCC technique is a more common technique [48]. The main reason for this is that it is an older technique and all aluminium alloy series can be produced with this technique. The TRC technique can only be used to produce alloys with a narrow solidification temperature range. However, TRC is rapidly becoming widespread among manufacturers [51]. The main reasons for this are less energy consumption in production and low investment cost. DCC alloy sheets are subjected to slow cooling speed in ingot form, to homogenization due to their heating prior to hot rolling and to high plastic deformation in hot rolling. These are not available in the TRC technique. Therefore, the thermal and mechanical process parameters applied in both techniques are different from each other and an alloy produced by TRC technique shows structural differences compared to the equivalent produced by DCC technique [48,52,53]. In general, products produced by the DCC and hot rolling technique have a more uniform structure, which is a desirable property for many metals and alloys [54,55]. Furthermore, the surface of aluminium sheets produced by the TRC technique may have defects such as surface stains or bleeds and defects such as centerline segregation in their internal structures. Lockyer et al. [56] and Yun et al. [57] reported that surface bleeds are formed due to sudden cooling of the melt and roller pressure between the twin rolls, and these bleeds contain a large number of intermetallic particles. Kim [55] showed in his study with AA5754 that melt conditioning creates a more uniform internal structure and reduces surface and centerline segregations. Das et al. [58] reported that micro-cracks, intergranular deposition and brittle intermetallic particles are the main problems in Al-Mg alloys (5000 series) produced by TRC technique. Intermetallic particles in alloys produced by TRC technique are generally smaller than those produced by DCC method [59]. Karlík et al. [60] compared both Al-Mg alloys (AA5754 and AA5182) produced by both techniques for both post-casting and final 1 mm and 3 mm thick plates. They found that the grains of the final plates for both alloys were coaxial and approximately the same size. However, they have found that intermetallic particles are smaller in plates produced by TRC technique. Similar results have been reported for AA5052 [53]. The authors reported that intermetallic particles in both AA5052 and AA5182 alloys produced by twin rollers were both smaller and more numerous than those seen in DCC alloys.

### 3. MATERIALS AND METHODS

#### 3.1. MATERIALS

This section consists of an electrochemical system that were used for electrochemical tests and chemicals that were used in thesis.

##### 3.1.1. Electrochemical System for Electrochemical Tests

Electrochemical tests were performed in a specific three-electrode cell (also called a flat cell, supplied from Biologic Instruments) except electrochemical noise measurements of galvanic couple. Image of the cell was shown in Figure 3.1.

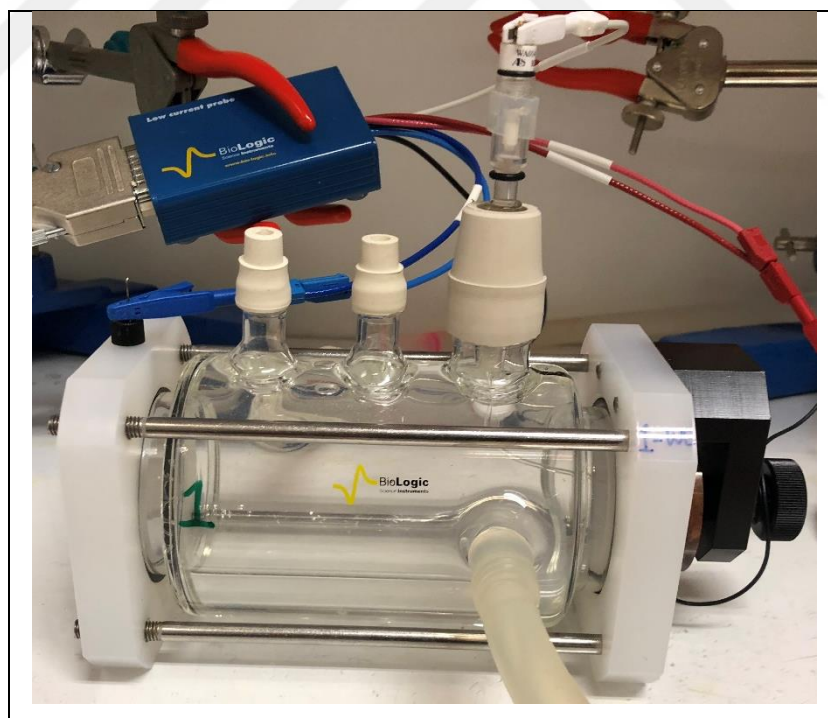


Figure 3.1. Image of the flat cell

This cell has a jacket for circulating water around the cell to adjust the electrolytic solution at a predetermined temperature; 25 °C. The volume of the cell is 350 mL.

All experiments consist of a reference electrode (RE), a working electrode (WE) a counter electrode (CE). Detailed information about electrodes are explained below.

### 3.1.1.1. Working Electrode (WE)

The electrode to be tested is called the working electrode. In this study, two aluminium alloy 5005 sheets produced by direct chill casting, DCC (H14- 1mm thickness) and twin-roll casting, TRC (H24, 1 mm thickness) were used as working electrodes. The only difference between H14 material and H24 material production processes is that H14 is produced by deformation in the last step and H24 is produced by partial annealing in the last step. These processes are not process steps that will make a difference in terms of intermetallics. Chemical compositions of these two samples were listed in Table 3.1.

Table 3.1. Compositions of AA5005 DCC and TRC alloy sheets

	Weight Percentage (%)					
	Mg	Fe	Si	Mn	Cu	Al
<b>AA5005 DCC, H14</b>	0.8	0.14	< 0.20	0.05	0.00	> 98.0
<b>AA5005 TRC, H24</b>	0.5	0.29	< 0.20	0.01	0.00	> 98.0

These aluminium alloy sheets were cut approximately 1cm x 1cm dimensions using guillotine machine. Then coupons were embedded in epoxy mixture. Epoxy mixture consists of an epoxy resin and an epoxy hardener with a 5:1 ratio. Cold mounting technique was used during the mounting process.

Before all electrochemical tests, working electrode surface was polished using the following polishing papers.

- P800, P1200 and P2500 SiC abrasive paper, supplied from Metkon Instruments Inc.

After polishing, working electrode was sonicated with high purity ethanol in sonicator for five minutes to remove the surface of it from foreign residues. After sonication, electroplating tape (Electroplating Tape 470; supplied from 3M) was stuck to the polished

surface to adjust the test surface area. For all experiments except metastable pitting measurements, test surface area was  $0.5 \text{ cm}^2$ . In metastable pitting measurements, smaller area was used which was  $0.03 \text{ cm}^2$  to decrease background current. Final images of the representative test surface is shown in Figure 3.2.

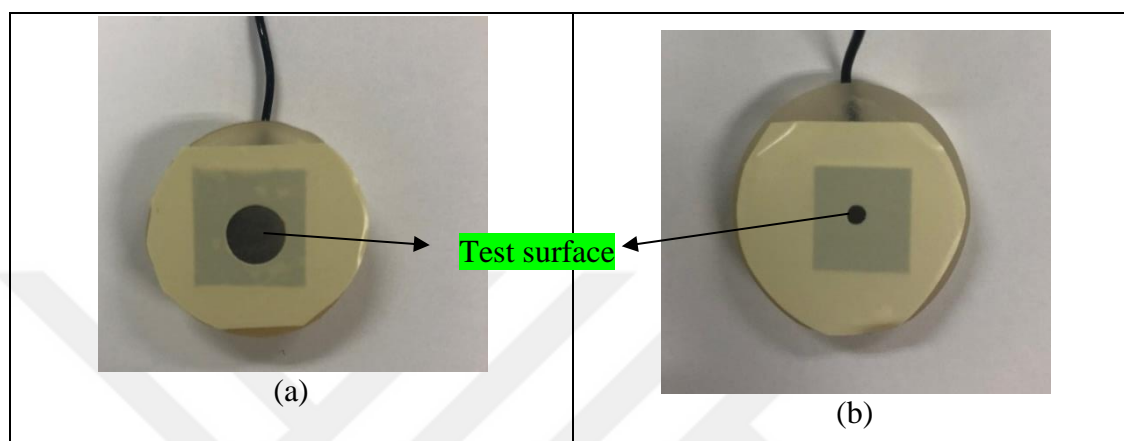


Figure 3.2. Image of the test surface with (a) larger test area;  $0.5 \text{ cm}^2$  (b) smaller test area;  $0.03 \text{ cm}^2$  for metastable pitting measurements

### 3.1.1.2. Reference Electrode (RE)

Reference electrode is necessary in all electrochemical test systems otherwise it is impossible to measure the potential of the working electrode. In this study, saturated calomel electrode, SCE (RE-2BP; supplied from ALS Company) was used and all potentials were reported with respect to this electrode. The RE was controlled every day with a lab reference (Ag/AgCl saturated KCl) to check if it is damaged. The deviation for the theoretical difference between lab reference and the working electrode should be in 2 or 3 mV range [61]. Figure 3.3 shows the reference electrode that was used in all experiments.

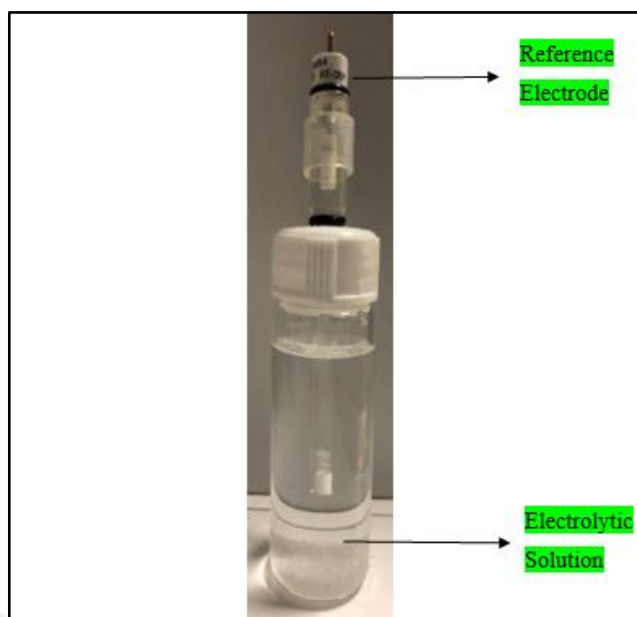


Figure 3.3. Image of the reference electrode

### 3.1.1.3. Counter Electrode (CE)

It is used for completing the electrochemical system in measurements. A large platinum gauze electrode 80 mesh (supplied from ALS company; dimensions: 35mm x 25mm) was used as a counter electrode in all experiments except EN measurements. EN technique was done using galvanically coupled of two identical working electrodes. Figure 3.4 shows the image of the Pt mesh.

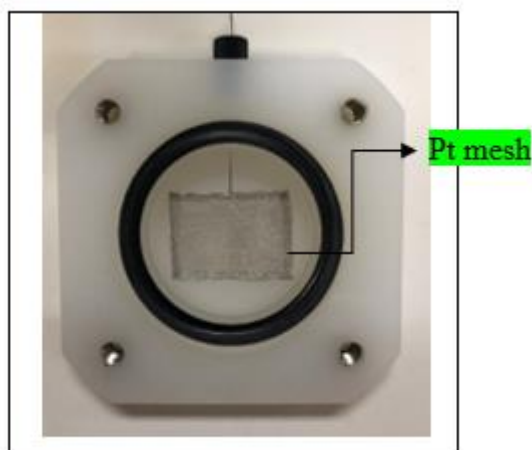


Figure 3.4. Counter electrode

#### 3.1.1.4. *Electrolytic Solution*

Sodium chloride solutions with four different chloride concentration (1 M, 0.1 M, 0.01 M and 0.001 M) were used in this study. During preparations of all solutions, deionized water (18.2 M $\Omega$ .cm) was used. Dissolved oxygen amount in the solution is one of the main parameters that affect the corrosion. Therefore, deaeration was done with high purity nitrogen gas (99.999 per cent, bought from HABAŞ) for exactly 1 hour in all experiments except electrochemical noise (naturally aerated NaCl solutions were used in EN).

#### 3.1.1.5. *Potentiostat / Galvanostat*



Figure 3.5. Potentiostat/galvanostat system

All electrochemical tests were conducted using SP-200 potentiostat/galvanostat device, manufactured by Biologic Instruments shown in Figure 3.5. This device is controlled by EC-Lab Software (v11.18 released on December 15, 2007) and EC-Lab Software Express (v5.56 released on August 26, 2014). All electrochemical experiments were conducted in Faraday cage (Figure 3.6). Faraday cage is used to eliminate external noises. It is crucial especially for electrochemical noise measurements. Figure 3.6 shows the image of the Faraday cage used in all experiments. The wooden box (70cm x 70cm x 52cm) was covered with copper plate. All sides of the box were connected to each other with an insulated copper cables.

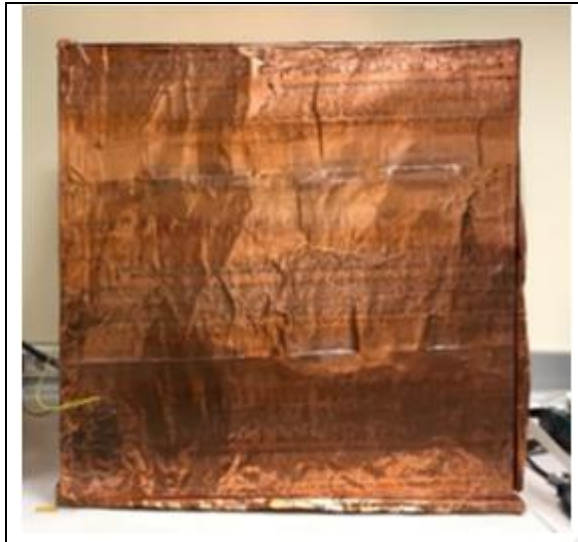


Figure 3.6. Image of the Faraday cage

### 3.1.2. Chemicals

The following chemicals were used in the study.

- Sodium Chloride, NaCl (puriss. p.a., ACS reagent, reag. ISO, reag. Ph. Eur.,  $\geq 99.8$  per cent, supplied from Sigma-Aldrich). It was used in the preparation of test solutions.
- Potassium Chloride, KCl (puriss. 99-100.5 per cent, supplied from Sigma-Aldrich). It was used to prepare the filling solution of the reference electrode.
- Ethanol, C<sub>2</sub>H<sub>5</sub>OH (absolute for analysis, EMSURE, ACS reagent, ISO, reag. Ph. Eur., supplied from Merck). It was used to degrease the coupon surface.
- Pure Nitrogen Gas, N<sub>2</sub> (99.999 per cent pure by volume, supplied from HABAŞ). It was used to deaerate test solutions.
- Deionized Water, H<sub>2</sub>O. Water was used to prepare test solutions.
- Epoxy Resin (supplied from Metkon Instruments Inc.)
- Epoxy Hardener (supplied from Metkon Instruments Inc.)

## **3.2. METHODS**

In this study, firstly, microstructure studies were done for each type of an alloy. Afterwards, immersion tests and then six different electrochemical tests were applied for each working electrode (DCC and TRC). This section explains the technical details (such as experimental parameters, measurement period etc.) about each test.

### **3.2.1. Microstructure Studies**

Microstructure investigations were performed on the outer surfaces of the plates. The sample surface was first wet-sanded with P1200 and P2500 SiC papers. It was then polished with 3  $\mu\text{m}$  diamond solution and 0.05  $\mu\text{m}$  colloidal silica. Then, it was etched with 0.5% HF. The intermetallics were examined by optical microscope (Nicon Eclipse L150) and scanning electron microscopy, SEM-EDS (Jeol JSM-6335F). The surface preparation and microstructure inspections were done at Tübitak MAM.

### **3.2.2. Immersion Tests**

Immersion tests were performed in naturally aerated 0.01 M NaCl solution. The surfaces to be examined by SEM were wet-sanded with P800, P1200 and P2500 grit SiC papers respectively. The samples to be examined by optical profilometer were polished with 1  $\mu\text{m}$  and 0.25  $\mu\text{m}$  diamond paste and 0.06  $\mu\text{m}$  colloidal silica. After sonication with 70% ethyl alcohol, they were allowed to dry spontaneously in the UV cabinet. Then, the electroplating tape with a hole corresponding to 2  $\text{cm}^2$  of diameter was applied to the surfaces to be examined in the UV cabinet. The other surfaces of the coupon were covered with electroplating tape. The jars and lids were autoclaved and the test solution was filtered using a 0.22  $\mu\text{m}$  filter to prevent biological growth for a waiting period of 1 week. The samples were placed into the solution with their surfaces facing upwards and the experiment was started by closing the jar lids. At the end of the waiting period, samples were removed from the solution. Afterwards, they were first washed with de-ionized water and then sonicated in a 70% nitric acid solution for 1 minute to clean the surface from corrosion products [62]. Samples were kept in desiccator until analysis. Prior to SEM (Jeol JSM-6335F), the surface



was coated with Pt for a better image. Surface morphology was obtained by optical profilometer (Bruker Contour GT-K). SEM examinations were performed at TUBITAK MAM and optical profilometer examinations were conducted at Erzurum Technical University.

### **3.2.3. Open Circuit Potential (OCP) Measurements**

In an OCP measurement, there is no external current or potential applied to the electrochemical system. Potentiostat/galvanostat records only the potential of the WE with respect to RE.

In this measurement, the test surface area was  $0.5 \text{ cm}^2$ . Experiment duration for each measurement was 3 hours. Potential data were recorded for every second. OCP measurements were conducted in three different deaerated NaCl solutions; 1 M, 0.1 M and 0.01 M. In each OCP measurement, a luggin capillary was used for decreasing the distance between the WE and the RE. The outside diameter of the capillary tip was 8 mm and the capillary tip distance between the capillary tip and the WE was 2 cm. Two experiments were conducted for each type of an alloy in each concentration.

### **3.2.4. Cyclic Potential Polarization (CPP) Measurements**

In CPP measurements, a potential sweep in the direction of more anodic (positive potentials) is applied to the WE with a predetermined scan rate. When the current reach a vertex current; the sweep direction is reversed and the potential is scanned until the initial potential is reached.

In this study, a CPP was started after 30 minutes of waiting at open circuit condition and an ohmic drop determination via impedance measurement at 100 kHz. Then, the anodic potential sweep was started at a potential 200 mV below the OCP. The anodic sweep was continued until a vertex current density is reached, after which the sweep was reversed. The cathodic sweep (in the direction of more negative potentials) was continued until the potential at which the CPP was started. The vertex current was  $1 \text{ mA/cm}^2$  for 1 M, 0.1 M, 0.01 M deaerated NaCl solutions and  $0.1 \text{ mA/cm}^2$  for CPP experiments in 0.001 M deaerated

NaCl solution. The sweep rate was 1 mV/s in all CPP measurements. The test surface area was 0.5 cm<sup>2</sup> and the data acquisition speed was 1 Hz for both sweeps. The RE was plugged in the luggin capillary tube. Outside diameter of the capillary tip was 8 mm and the distance between the capillary tip and WE in whole experiments was 2 cm. At least eight repetitive experiments were done for each alloy in 1 M, 0.1 M and 0.01 M solutions. For 0.001 M NaCl, at least 5 experiments were conducted.

### **3.2.5. Potentiostatic Measurements (PSM) for Repassivation Potential (E<sub>repass</sub>) Determination**

In a potentiostatic measurement, a constant potential is applied to the WE during a time interval and the potentiostat records the current. Experimental procedure consisted of the following steps:

- a) Before any potentiostatic measurement, solution resistance ( $R_{sol}$ ) was determined. Afterwards, 30 minutes were waited under open circuit conditions and the OCP was recorded.
- b) A potential higher than the pitting potential, called the activation potential, was applied until 0.06 Coulomb (0.12 C/cm<sup>2</sup>) of charge had passed through the working electrode. This was done to activate pits at the test surface. This step is called the activation step in this study.
- c) A potential lower than the activation potential was applied for 15 minutes and the current was recorded. This step is called the potentiostatic step in this work.
- d) Steps a to c was repeated with a new sample coupon but, in step c, a potential 50 mV lower than the potential of the previous potentiostatic step was applied. Measurements were continued until the average current density falls below 1  $\mu\text{A}/\text{cm}^2$  in the potentiostatic step. Once the potential at which the average current density falls below 1  $\mu\text{A}/\text{cm}^2$ , which is a typical passive current density, the potential applied in the potentiostatic step was changed with increments of 25 mV for a narrower determination of  $E_{repass}$ .

This enabled the determination of the repassivation potential. Table 3.2 shows the activation potentials for each concentration. These potentials are above the pitting potentials in each concentration to create pitting corrosion.

In these measurements, the surface area of the WE was also  $0.5 \text{ cm}^2$ . Distance between the WE and RE was 2 mm in 1 M, 2 cm in 0.1 M and 8 mm in 0.01 M experiments.

Table 3.2. Applied activation potentials

	1 M NaCl	0.1 M NaCl	0.01 M NaCl
<b>Initial Potential (mV)</b>	-650	-550	-500

### 3.2.6. Galvano-staircase Cyclic Polarization (GSCP) Measurements

In galvano-staircase cyclic polarization measurements (GSCP) predetermined currents are applied step by step and potentials are recorded [63]. Therefore, as opposed to the previous techniques, the current is controlled and the potential of the WE is recorded. In this technique, test surface area was also  $0.5 \text{ cm}^2$ . Before each measurement, solution resistance determination and OCP measurement for one minute were done. Then, current was applied starting from  $0 \mu\text{A}$  up to  $60 \mu\text{A}$  ( $120 \mu\text{A}/\text{cm}^2$ ) with  $10 \mu\text{A}$  ( $20 \mu\text{A}/\text{cm}^2$ ) increments. Then it is reversed from  $60 \mu\text{A}$  to  $0 \mu\text{A}$  with the same increment. Each current step lasted for 2 minutes and the potential was recorded. Data acquisition speed for was 2 Hz. In these experiments, the distance between the RE and the WE was 8 mm. Experiments were conducted in three different concentrations of sodium chloride (1 M, 0.1 M and 0.01 M). Each type of alloy (both DCC and TRC) were measured five times in each concentration. In each repeat, a new sample coupon was used.

### 3.2.7. Metastable Pitting Corrosion Measurements under Potentiostatic Conditions

Metastable pits are pits that can form at potentials below the pitting potential of the alloy. A metastable pitting event can be seen as a current rise and drop in a current versus time plot. Due their relation to the stable pitting they have been given much attention [12,64–66]. Metastable pitting experiments were conducted at constant applied potentials. Before the potentiostatic measurements, solution resistance determination was done. Then, a potential was applied for 30 minutes. The applied potentials were -50 mV, -75 mV and -100 mV below the  $E_{\text{pit}}$  of each alloy in the NaCl solution [64]. Experiments were done in 350 mL of

deaerated 0.01 M and 0.001 M NaCl solutions using the three electrode flat cell. Data acquisition speed was 10 Hz. Test surface area of the electrode was 0.03 cm<sup>2</sup> (see Figure 3.2 b). Three identical experiments were conducted for each alloy in each concentration. To make a comparison between the alloys, the rate of metastable pitting and the total charge of metastable pitting events were determined from the current versus time data.

### **3.2.8. Electrochemical Noise (EN) Measurements of Galvanic Couple**

Different from the previous techniques, two working electrodes were galvanically coupled in these measurements. Two working electrodes were placed in a custom made cell as shown in Figure 3.7. The RE was used to measure the potential of the couple. In this mode of experiment, the potentiostat measures the potentials of each working electrode and tries to equate them by injecting current to either WE. This current as a function of time is called the current noise. The potential of the couple with respect to the RE versus time is called the potential noise. 700 mL of naturally aerated 0.1 M and 0.01 M NaCl solutions were used as test solutions. Surface of each electrode of the couple was 0.5 cm<sup>2</sup>.

In this study, two different types of measurement were done. In the first type, the EN measurement was started right after immersion with a fixed current range for 9 minutes. Then, the system was waited at open circuit conditions for one minute. Afterwards, electrochemical noise measurement was recorded for 3 hours with a fixed current range. In the second type, measurement was lasted for 30 minutes after 24 hours waiting in open circuit conditions. A new pair of working electrodes were used in both types of measurement. Each type of measurement was repeated twice.

Electrochemical noise measurement was done using zero resistance ammeter, ZRA, method in EC-Lab Express software. A low pass 5 Hz filtering was used. This was done to eliminate aliasing since a data acquisition frequency of 10 Hz was used.

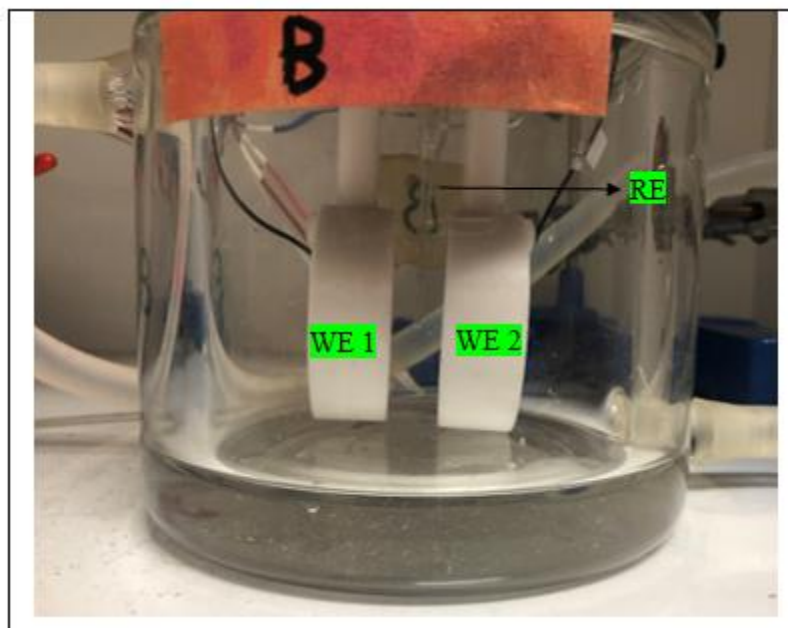


Figure 3.7. Image of the three-electrode round cell. Working electrode 1 (WE 1) and the working electrode 2 (WE 2) are coupons of the same alloy. Seen between the two is the salt bridge tube containing the reference electrode.

## 4. RESULTS AND DISCUSSION

### 4.1. MICROSTRUCTURE STUDIES

Intermetallics in the alloys were investigated using both optical microscope and SEM-EDS. The optical microscope images taken after polishing and etching with HF are given in Figure 4.1. Dark figures in the images show intermetallic particles. The rolling axis is the up-down direction. Larger intermetallic particles are seen in the DCC alloy. On the other hand, the TRC alloy has a greater number of intermetallics. In the TRC alloy, several intermetallics with a size of about  $5\ \mu\text{m}$  have also been identified (Figure 4.2b). Optical images were analysed with microscope software. The results obtained about the size and number of intermetallic particles are given in Table 4.1. Each particle size were determined by the optical microscopy software.

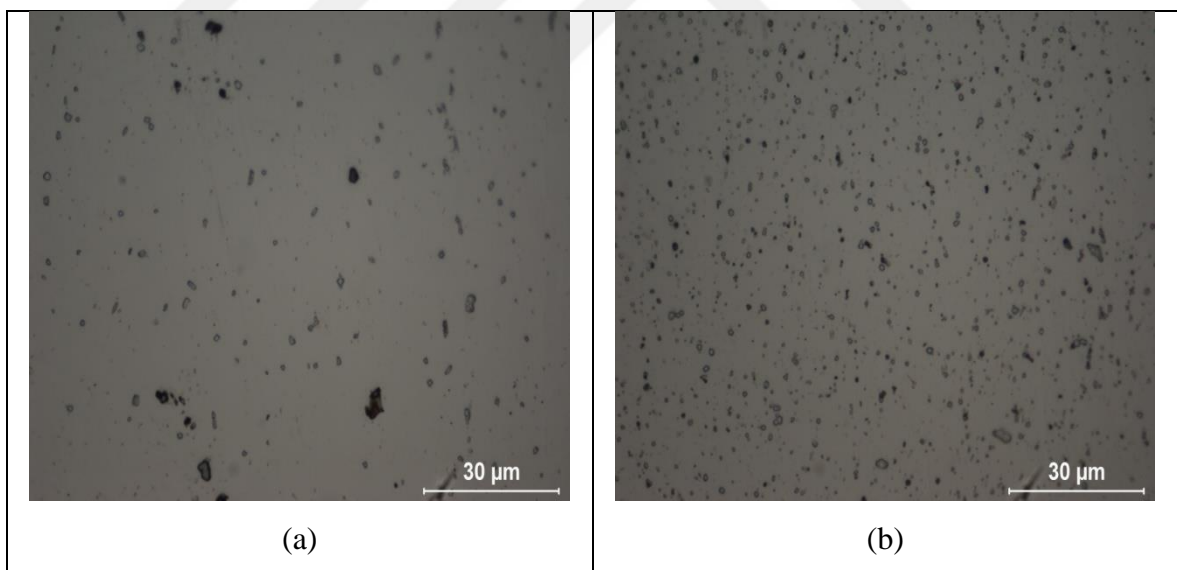


Figure 4.1. Optical microscope images of (a) DCC alloy (b) TRC alloy after etching with HF

Table 4.1. Size and number of intermetallic alloys

	<b>DCC alloy</b>	<b>TRC alloy</b>
<b>Maximum diameter, <math>\mu\text{m}</math></b>	6.4	4.8
<b>Average of max. diameter, <math>\mu\text{m}</math></b>	$0.9 \pm 0.9$	$0.8 \pm 0.6$
<b>Quantity</b>	279	974

HF etched samples were also examined by SEM-EDS. Figure 4.2 gives SEM images of alloys. Images are compatible with optical microscope results. The alloys produced by the DCC technique contain larger intermetallics than TRC alloys. It is seen that the alloys produced by TRC technique contain more intermetallics.

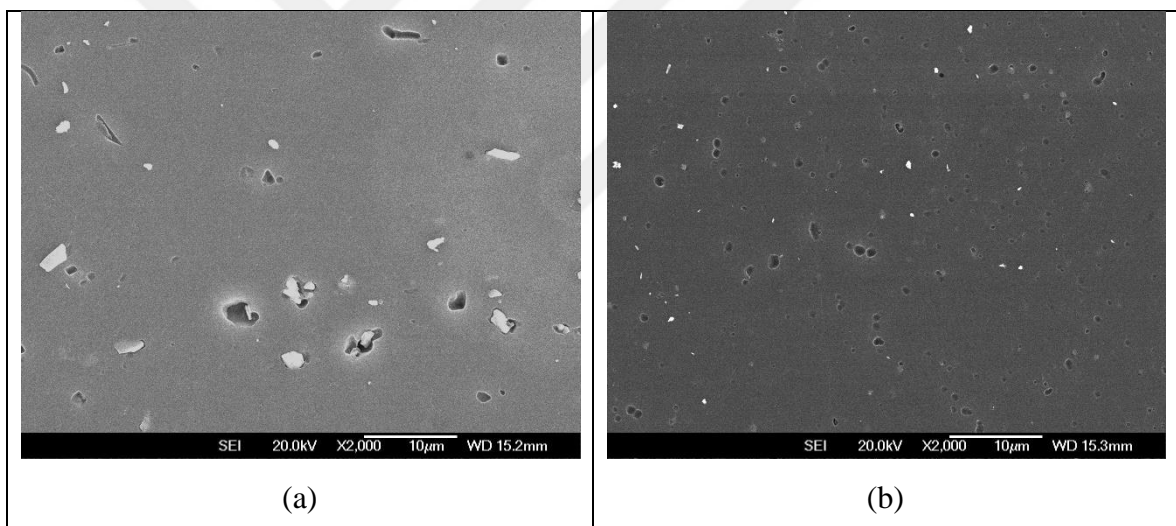


Figure 4.2. SEM images of (a) DCC alloy (b) TRC alloy after etching with HF

EDS analysis was conducted on the intermetallics and the elements they contained were determined. Examples and analysis of intermetallics in AA5005 alloys are shown in Figure 4.3. Intermetallics mainly contain Al, Fe and Si, but a small amount of Mg was also found. Although the main alloying element in the AA5005 alloy is Mg, it is known to have a high solubility in aluminium. The particles in both DCC and TRC alloys contain Fe and Si. Since Fe-containing particles are more cathodic than aluminium matrix, it has been reported in the literature that they are destructive to pitting corrosion [67–69].

There are differences in Fe, Mg and Mn contents of DCC and TRC alloys. Fe content is higher in TRC alloy. Ambat et al. [67] compared Al-0.11 percent Fe, Al-0.04 percent Fe and Al-0.42 percent Fe containing microstructures of the alloy model and reported that the number of intermetallics as Fe percentage increases. In addition to the production method, a higher Fe content is likely to contribute to a greater number of intermetallic formations in the TRC alloy. Magnesium has a high solubility in aluminium and is present in less than 1 percent solid solution [70].  $Mg_2Al_3$  and  $Mg_2Si$  intermetallics which are seen in higher Mg content alloys were not observed in this study. Therefore, the effect of different Mg content in two AA5005 alloys has no effect on intermetallics. Mn content of both alloys (0.05 percent and 0.01 percent) is quite low. Zamin [29] studied the impact of manganese on corrosion resistance of Al-Mn alloys in the range of 0.4 percent -1.2 percent Mn.

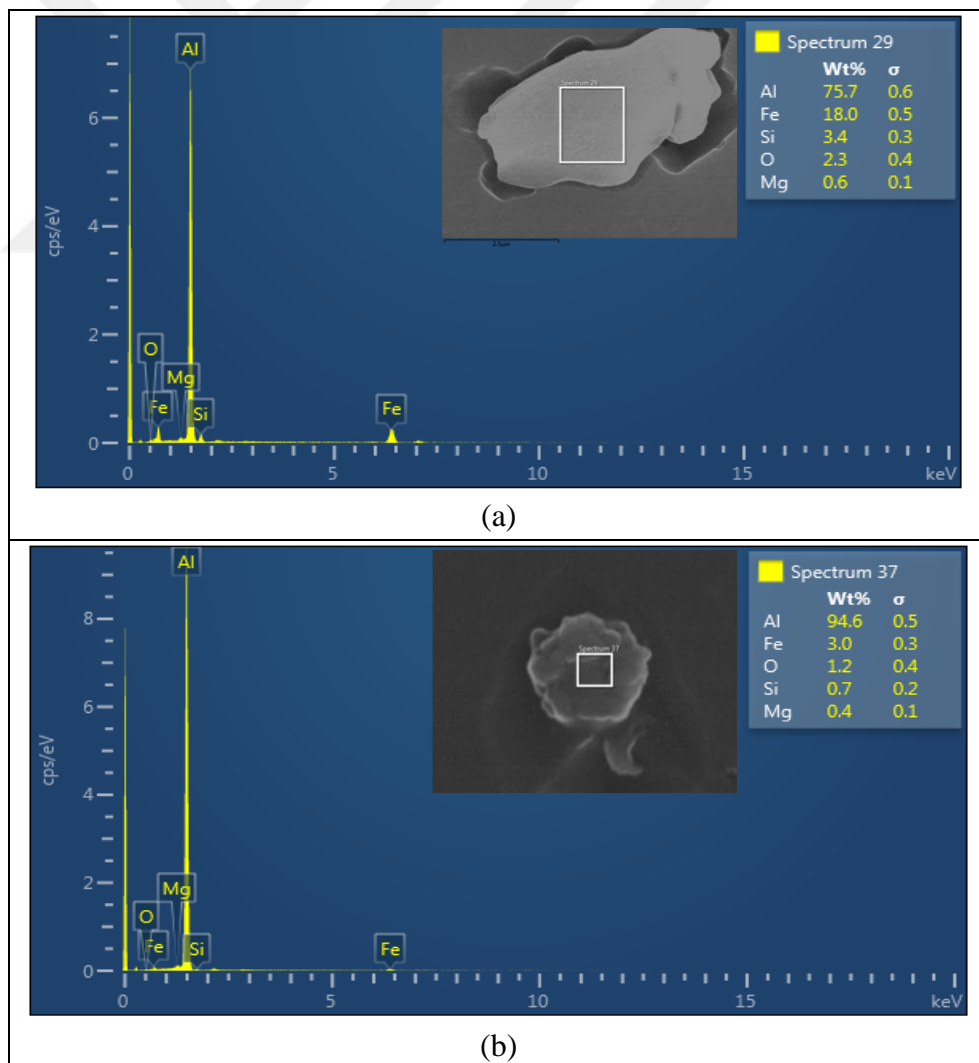
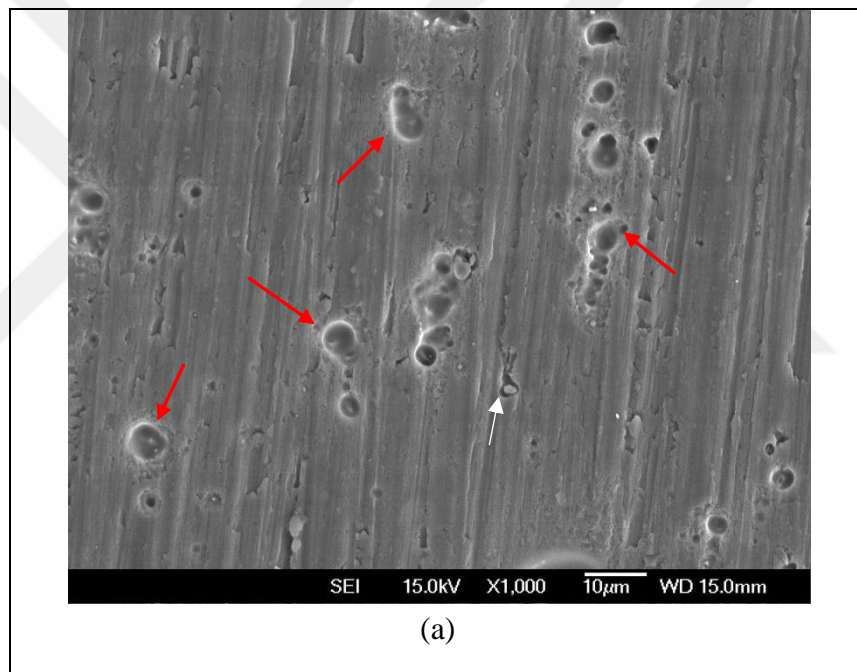


Figure 4.3. EDS analyses of intermetallics for (a) DCC and (b) TRC alloys



## 4.2. IMMERSION TESTS

In the immersion tests, AA5005 alloys produced by DCC and TRC techniques were kept in 0.01 M NaCl solution for 7 days at room temperature. After the surfaces were cleaned from corrosion products, scanning electron microscopy (SEM) and optical profilometry were conducted. Figure 4.4 shows SEM images of DCC and TRC alloys at 1000x magnification. White arrows in Figure 4.4 show the pits while red lines indicates larger pits. In the DCC alloy sheet, it is seen that there are much larger pits than TRC alloy. In both alloys, pits form around the intermetallics, so the matrix around them is dissolved.



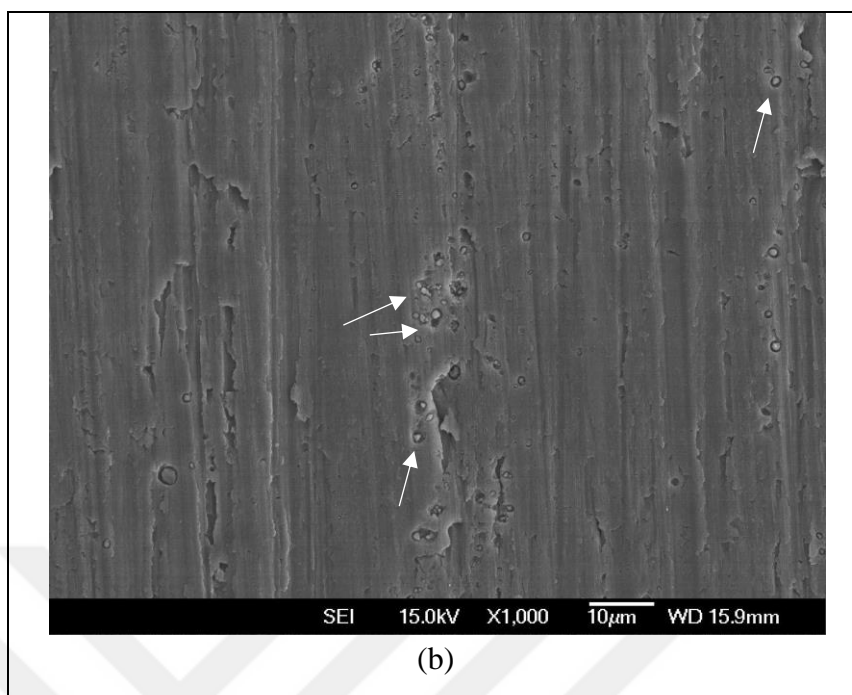


Figure 4.4. SEM images of the (a) DCC alloy (b) TRC alloy after 7 days of immersion in 0.01 M NaCl solution

The higher Mg content (hence the higher potential difference between the intermetallic particles and the aluminium matrix in this alloy) is likely to contribute to the formation of larger pits in the DCC alloy than to the TRC alloy, in addition to the presence of larger intermetallics in the DCC (Table 4.1). In the DCC alloy, it is seen that pits with dimensions of 4-5 microns are formed. Red arrows show examples of these pits.

Optical profilometry is one of the methods used to examine the pits formed on the alloy surfaces after the immersion tests [71–73]. Optical profilometry images were shown in Figure 4.5 for (a) DCC and (b) TRC alloys. The scale next to each picture shows the relative depth from the surface. Red means elevation and blue means pit. The upper part of Figure 4.5 (a) shows large pits which were indicated with white arrows. The DCC alloy shows larger pits..

As a result, both optical profilometer and SEM investigations showed that pits of larger diameter were found in DCC alloy than TRC alloy.

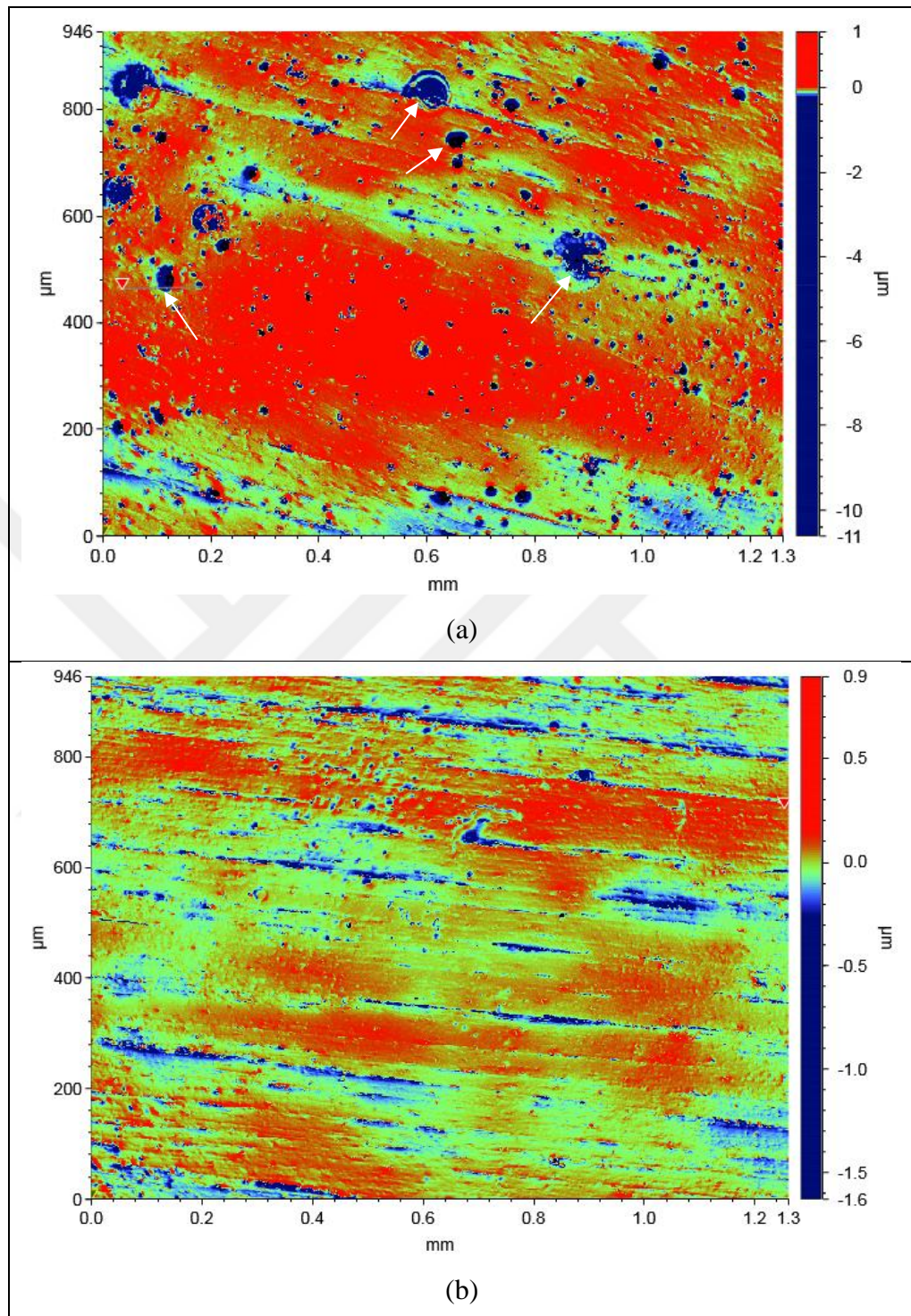
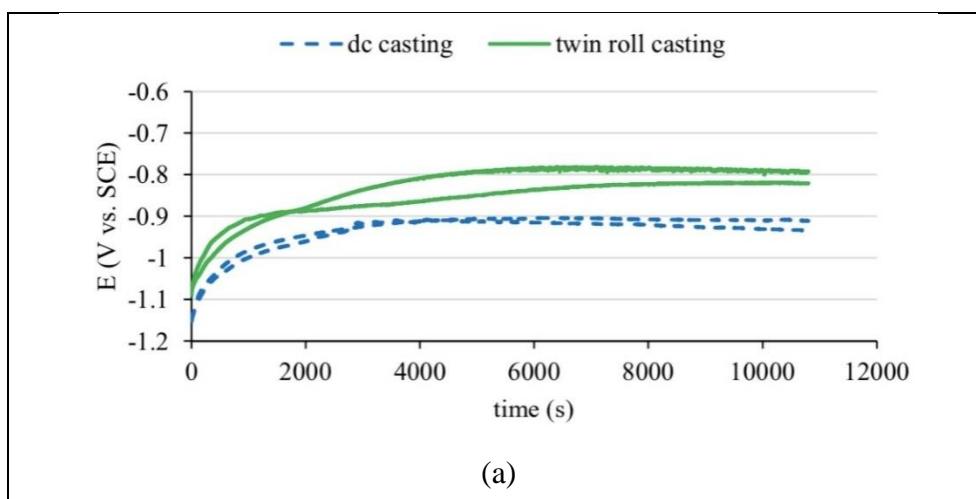


Figure 4.5. Optical profilometer images of (a) DCC (b) TRC alloy after 7 days of immersion in 0.01 M NaCl solution

### 4.3. OPEN CIRCUIT POTENTIAL (OCP) MEASUREMENTS

The aim of open circuit potential measurements is to determine a specific potential (called open-circuit potential,  $E_{ocp}$ , or the corrosion potential,  $E_{corr}$ , of the WE (AA5005 DCC and TRC). In an OCP measurement, there is no external potential or current applied to the WE. Potentiostat records only the potential evolution of the electrode in the solution. Under the open-circuit conditions, the rates of cathodic processes are equal to the rates of anodic ones on the WE surface. Generally, open-circuit potential changes rapidly right after the electrode is immersed into the solution. Depending on the alloy and the solution, a steady state open circuit potential may be attained. For instance, a steady state  $E_{ocp}$  of -750 mV vs. SCE was reported for AA6061 in 3.5% NaCl solution with pH=6 [74].

Experimental details of the OCP measurements done in this study were given in Section 3.2.3. Figure 4.6 shows the OCP results for AA5005 DCC and AA5005 TRC alloys in (a) 1 M, (b) 0.1 M and (c) 0.01 M NaCl solution. Two identical experiments were done in each concentration. For 1 M NaCl solution,  $E_{ocp}$  increased rapidly after the immersion for both the DCC and TRC alloy sheets. Steady  $E_{ocp}$  values were obtained with both alloys during the experiments (approximately after 5000 seconds for TRC alloy and 3000 seconds for DCC alloy). The TRC alloy exhibited more anodic potentials. This is probably due to the lower amount of Mg in the TRC alloy sheet (Table 3.1). Since Mg is a more active metal than aluminium, the alloy with less Mg content can be expected to have a more positive  $E_{corr}$ . At the lower concentrations (0.1 M and 0.01 M NaCl solution), the difference between the open-circuit potentials are lower. However, during the initial approximately 1000 s, the TRC alloy exhibited more anodic  $E_{ocp}$ .



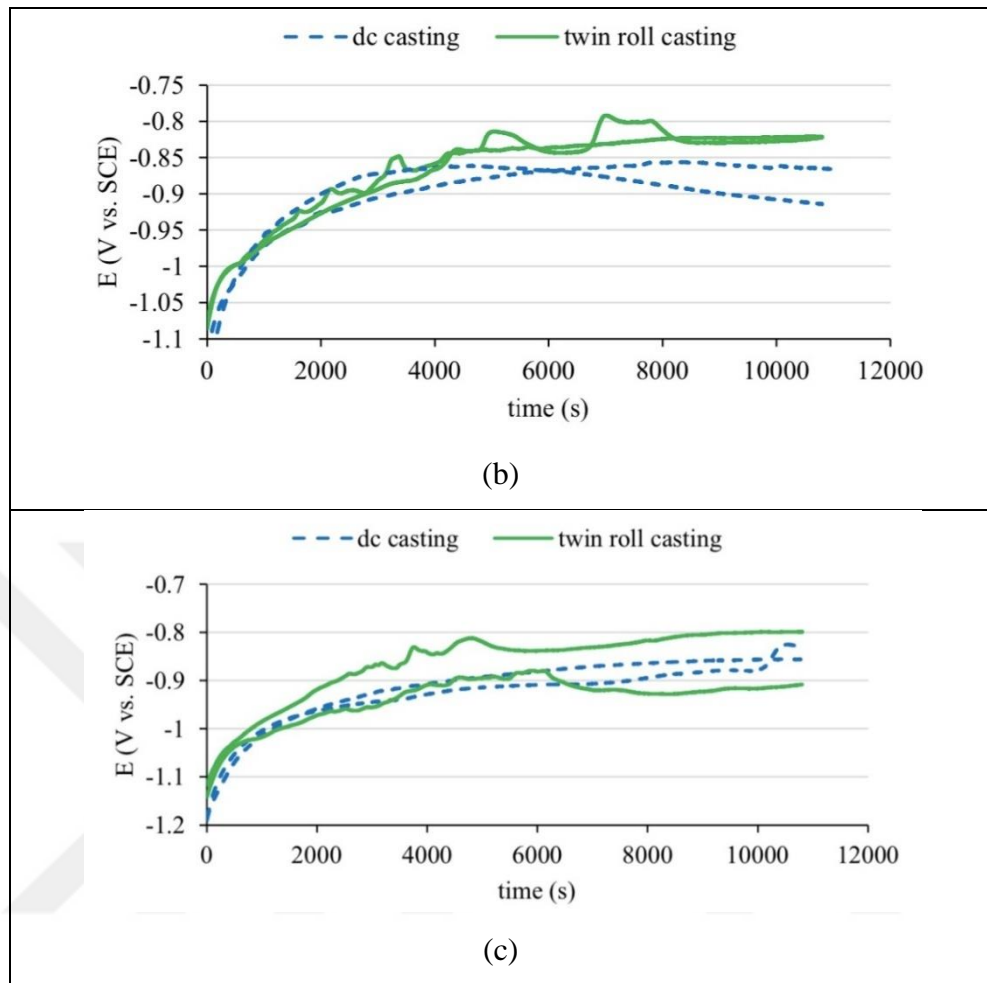


Figure 4.6. OCP results for the AA5005 DCC and the TRC alloy (a) 1 M, (b) 0.1 M and (c) 0.01 M NaCl solution

#### 4.4. CYCLIC POTENTIAL POLARIZATION (CPP) MEASUREMENTS

Cyclic potential polarization measurement is the most frequently used electrochemical tests in corrosion studies. It is used for the determination of important quantities such as pitting potential ( $E_{\text{pit}}$ ), repassivation potential ( $E_{\text{repass}}$ ) and passive current density ( $i_{\text{pass}}$ ). Figure 4.7 illustrates these parameters on a representative CPP curve.

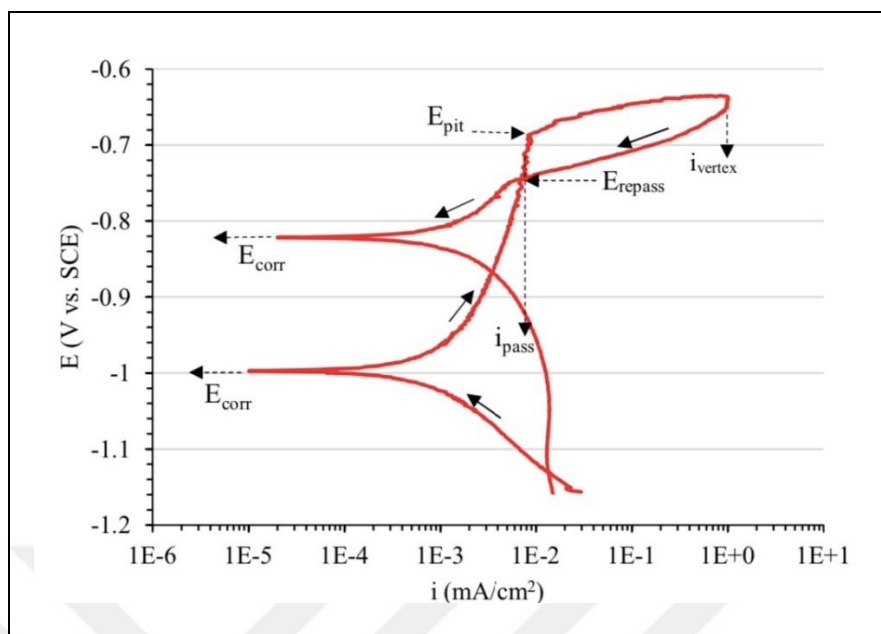


Figure 4.7. Schematic illustration of some quantities related to corrosion on a representative CPP curve

A CPP curve shows the potential as a function of the current density applied by the potentiostat. The applied current density is the difference between the anodic and cathodic current densities. In this study, the CPP experiments were started at a potential, which was 200 mV below the working electrode's open circuit potential (that is,  $E_{\text{corr}}$ ). Potential was increased by means of the potentiostat at a predetermined scan rate. Initially, there is net cathodic current (the cathodic branch), which decreases up to  $E_{\text{corr}}$ . At  $E_{\text{corr}}$ , the anodic current density is equal to the cathodic current density and, hence, the applied current density is very small. Above  $E_{\text{corr}}$ , the anodic branch is seen. As the potential is scanned in the positive direction (towards more positive potentials, anodic direction), once a pit(s) initiates on the electrode surface, a fast rise in current is seen. This potential is defined as the pitting potential,  $E_{\text{pit}}$ . The anodic sweep stops and the direction of the potential sweep is reversed at the vertex current density ( $i_{\text{vertex}}$ ). In the reverse scan (towards more negative potentials, cathodic direction), the applied current density decreases. The potential at which the backward sweep crossed the forward sweep is taken as the repassivation potential,  $E_{\text{repass}}$  (also known as the protection potential,  $E_{\text{prot}}$ ) in this study [75,76]. Furthermore, the average of the current densities on the forward sweep between the  $E_{\text{repass}}$  and the  $E_{\text{pit}}$  is taken as the passive current density,  $i_{\text{pass}}$ . As the potential is scanned in the cathodic direction, an  $E_{\text{corr}}$  more positive than that seen on the forward sweep is seen. This is likely to be due to the

changed surface conditions and pits formed on the surface. Afterwards, a cathodic current is seen until the end of the backward sweep.

Figures 4.8, 4.9, 4.10 and 4.11 show the CPP curves for 1 M, 0.1 M, 0.01 M and 0.001 M NaCl solutions, respectively. In each figure (a) shows representative CPP curves for the DCC alloy sheet and (b) shows representative CPP curves for the sheet produced by the TRC method. Black arrows on the figures show the direction of the scan.

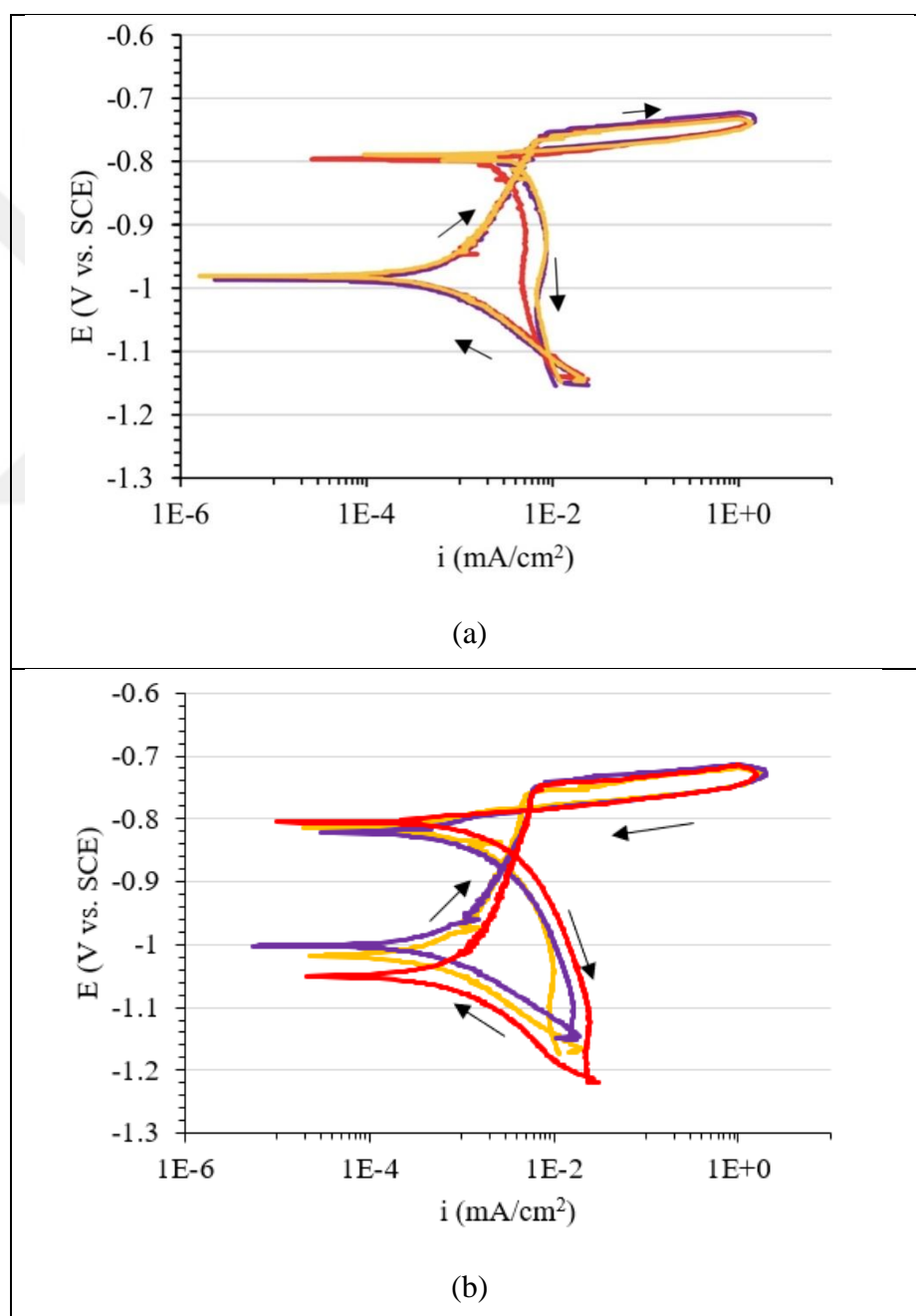


Figure 4.8. CPP curves in 1 M solution for the (a) DCC, (b) TRC alloy sheets

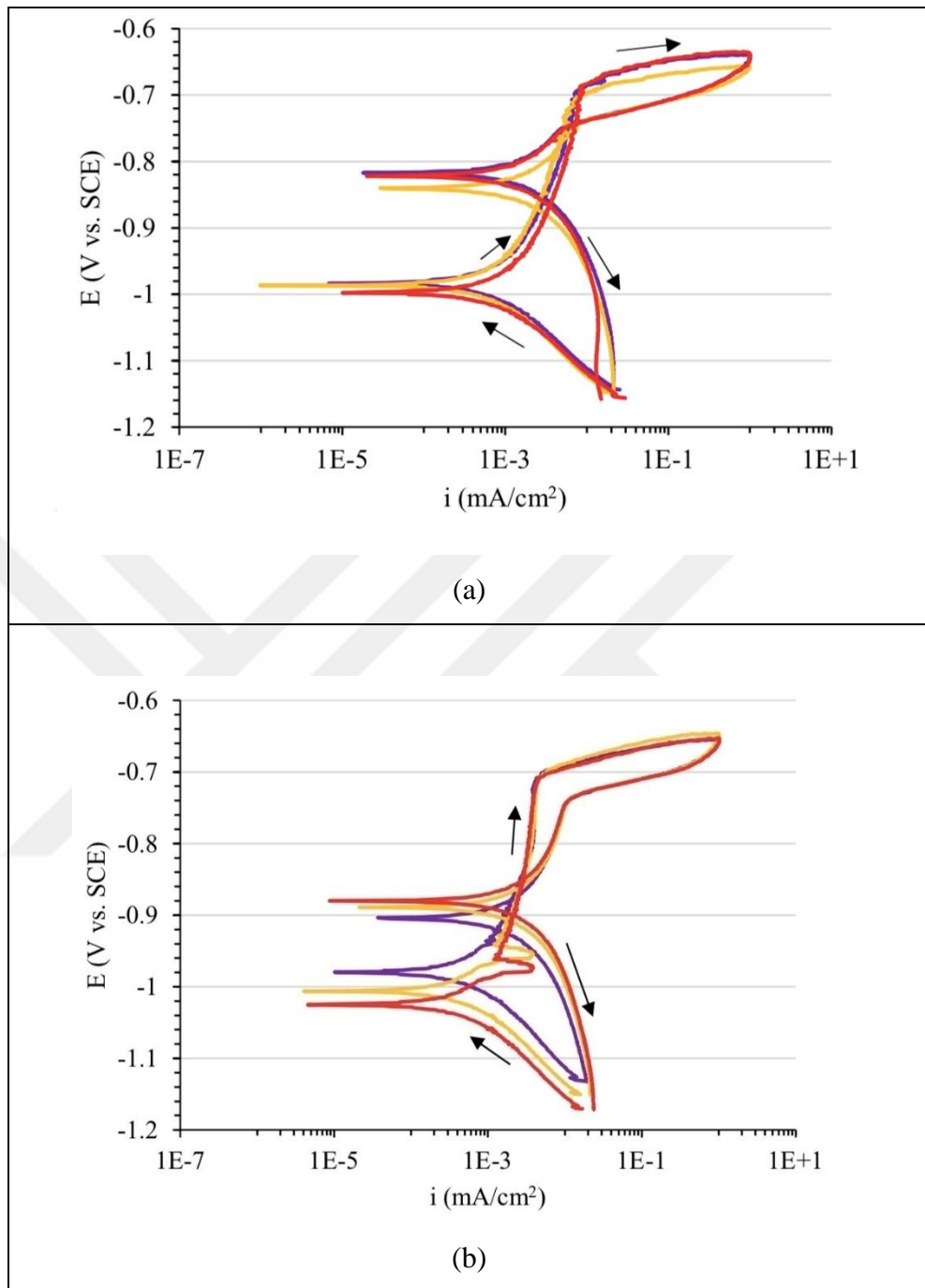


Figure 4.9. CPP curves in 0.1 M solution for the (a) DCC, (b) TRC alloy sheets



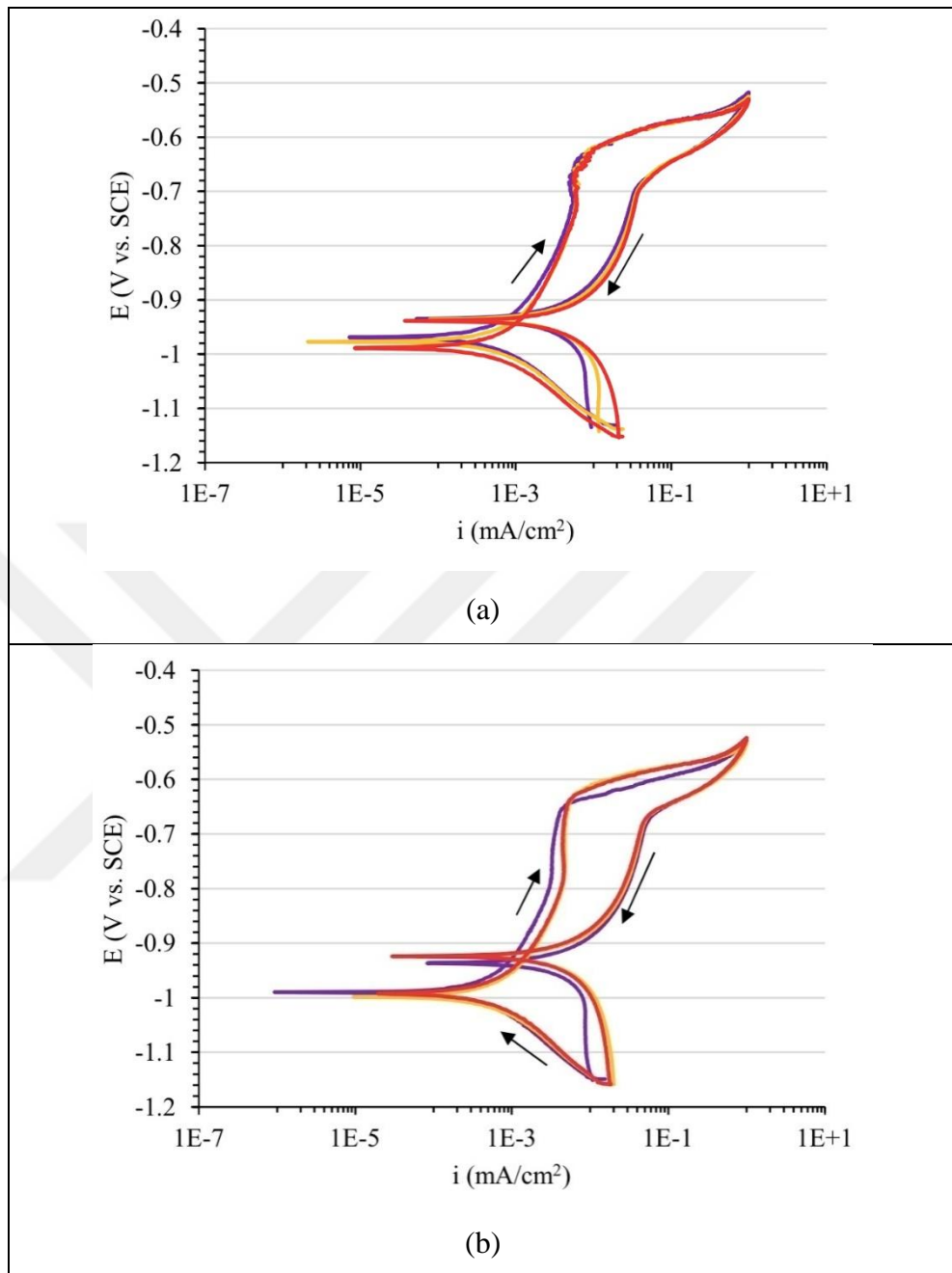


Figure 4.10. CPP curves in 0.01 M NaCl solution for the (a) DCC, (b) TRC alloy sheets

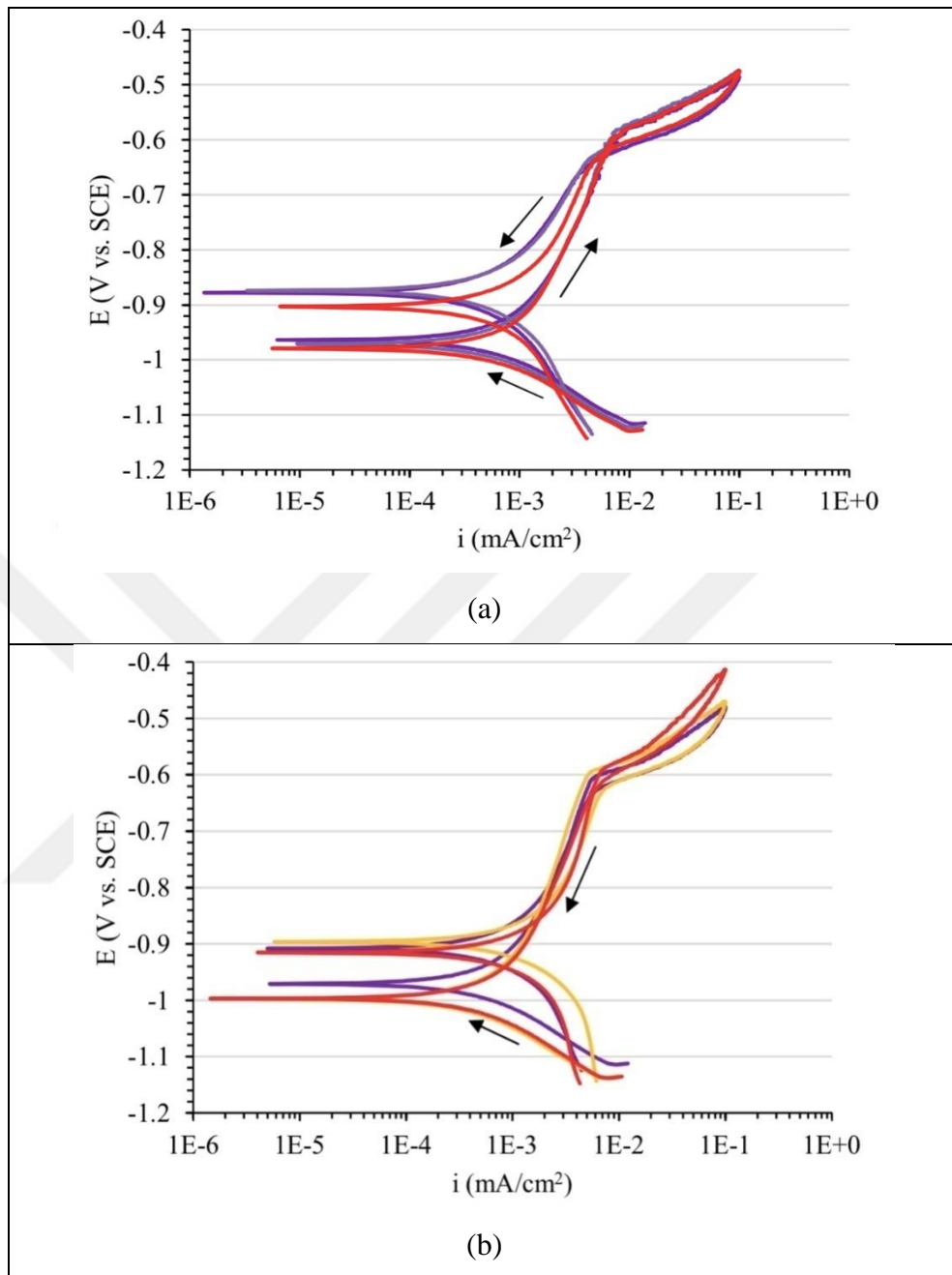


Figure 4.11. CPP curves in 0.001 M solution for the (a) DCC, (b) TRC alloy sheets

Note that nine identical CPP experiments for 1 M, 0.1 M and 0.01 M NaCl solutions and five identical CPP experiments for 0.001 M were carried out with freshly polished electrodes. For a clear presentation only three representative curves were plotted for each concentration. The measurements not shown in these figures are given in Appendix A.

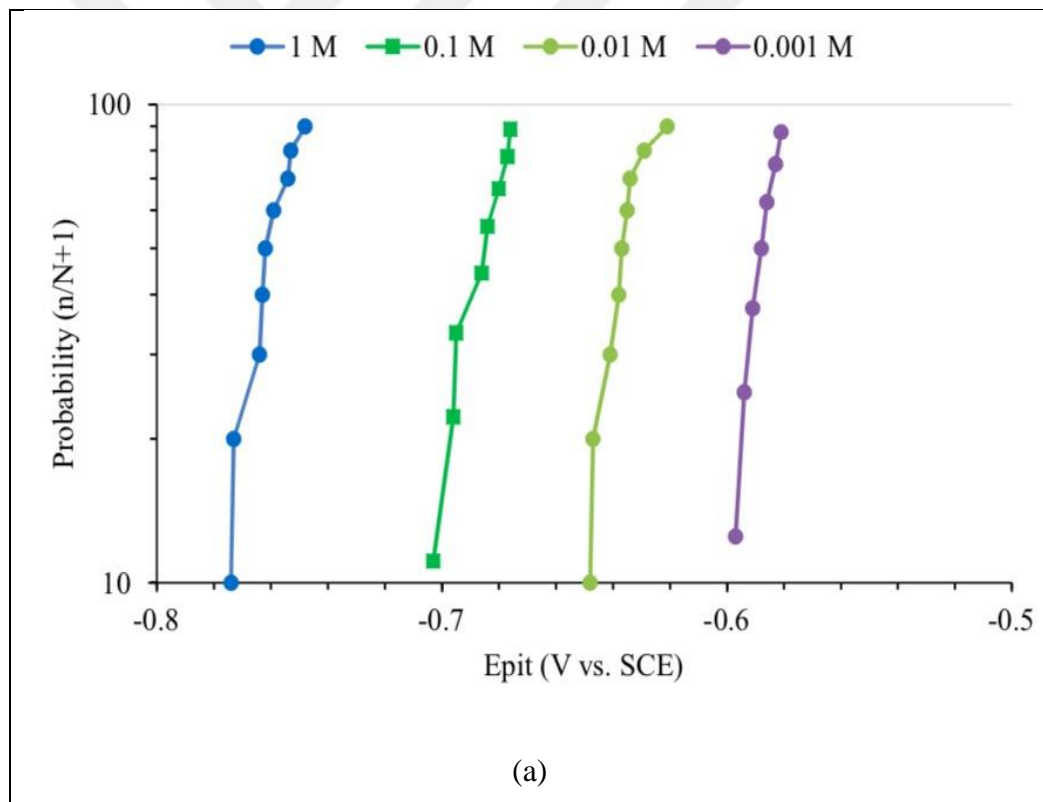
The tendency of a metal or an alloy to undergo pitting corrosion is related to the  $E_{\text{pit}}$  (sometimes called breakdown potential,  $E_{\text{bd}}$ ). It is generally accepted that the higher (more positive) the  $E_{\text{pit}}$ , the larger the resistance of the sample to the pitting corrosion [77]. In this study,  $E_{\text{pit}}$  values were determined by the inflection method [75,78]. Comotti et al. [75] found the  $E_{\text{pit}}$  values for different alloys by intersection of two extrapolated lines about the breakdown.

After the determinations of  $E_{\text{pit}}$  values for each measurement, arithmetic average were calculated. The average  $E_{\text{pit}}$  values are listed in Table 4.2. From Table 4.2, it is seen that as the chloride concentration decreases the  $E_{\text{pit}}$  becomes higher (more positive) for both alloys. That is, decreasing the chloride concentration makes the alloy less susceptible to pitting. Similar dependence of  $E_{\text{pit}}$  on chloride ion concentration are also reported [12,79,80]. Zaid et al. [74] found the similar behaviour for AA6061 in nearly neutral medium (pH=6). Comparing AA5005 DCC alloy with the AA5005 TRC alloy, there is not much difference between their  $E_{\text{pit}}$  values at the same concentration. The highest difference in  $E_{\text{pit}}$  values are at 0.1 M and is 16 mV. Except 1 M NaCl concentration, the DCC alloy has a slightly more positive  $E_{\text{pit}}$ . Therefore, it can be concluded that the DCC alloy and the TRC alloy have almost the same resistance the pitting corrosion based on their  $E_{\text{pit}}$  values calculated from the CPP measurements. Gupta et al. [64] found the pitting potential of AA5005-H34 sample as -0.433 V vs SCE in deaerated 10  $\mu\text{M}$  NaCl solution. Since their concentration (10  $\mu\text{M}$ ) is lower than the lowest chloride concentration tested in this study (1000  $\mu\text{M}$ ), it is reasonable that their  $E_{\text{pit}}$  is more positive than found in this study (Table 4.2). Moreover, Trueba and Trasatti [81] reported the  $E_{\text{pit}}$  of Al-0.77 Mg alloy as - 0.66 V vs. SCE in deaerated 0.1 M NaCl solution. This is also close to the  $E_{\text{pit}}$  found in this study (-0.686 V for DCC alloy and -0.702 V for TRC alloy).

Table 4.2.  $E_{\text{pit}}$  values and their standard deviations

NaCl concentration	AA5005 DCC	AA5005 TRC	$\Delta E$ (mV)
	V vs. SCE		
<b>1 M</b>	-0.761 $\pm$ 0.009	-0.754 $\pm$ 0.006	-7
<b>0.1 M</b>	-0.686 $\pm$ 0.010	-0.702 $\pm$ 0.006	16
<b>0.01 M</b>	-0.637 $\pm$ 0.008	-0.642 $\pm$ 0.012	5
<b>0.001 M</b>	-0.589 $\pm$ 0.006	-0.596 $\pm$ 0.006	7

Many researchers found that  $E_{\text{pit}}$  exhibits a normal probability distribution [25,65,68,69,82,83]. In order to see the suitability, probability plots were represented in Figure 4.12 for (a) DCC and (b) TRC alloy in 1 M, 0.1 M, 0.01 M and 0.001 M NaCl solutions. Probability of pitting potential is calculated using the formula “ $n/(N+1)$ ” in accordance with Shibata and Takeyema [83] where N is the total number of experiments and n is the number of samples pitted before a given potential. From Figure 4.12, it is seen that the pitting potentials exhibit approximately normal distributions for both alloys in all solutions. However, there are some deviations from linearity. Similar deviations were also reported [65,83]. For instance, Pride et al. reported the pitting potentials of pure aluminium as a function of various chloride ion concentrations. They reported that the larger deviations occur at the most dilute NaCl concentrations.



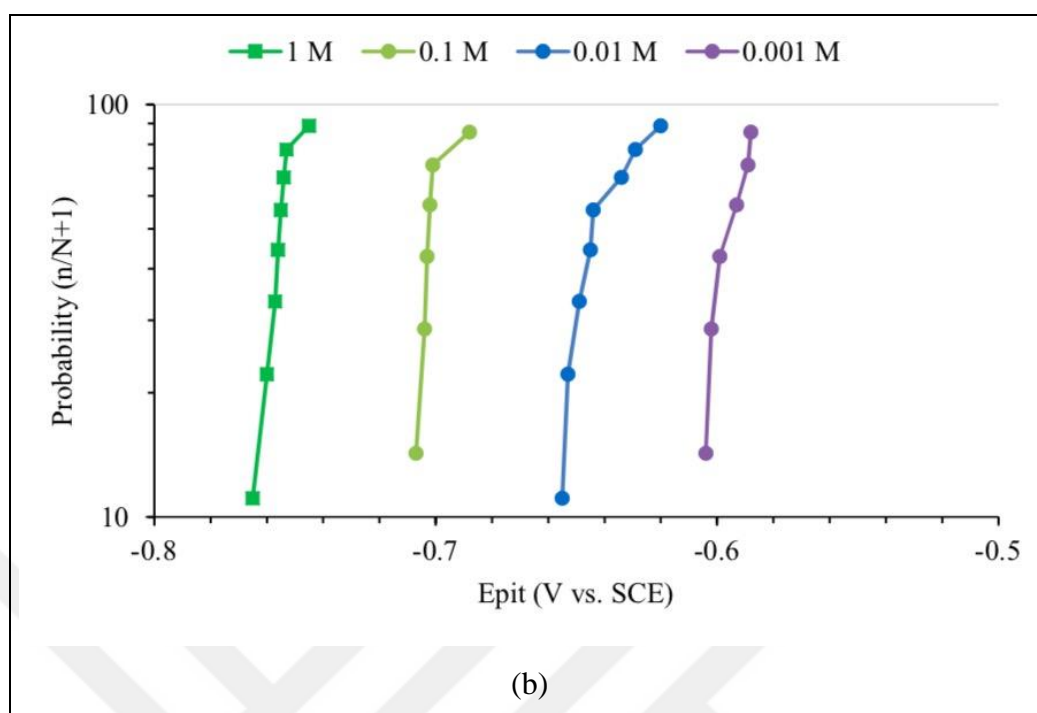


Figure 4.12. Normal cumulative probability plots of pitting potentials for the (a) DCC (b) TRC alloy plates in 1 M, 0.1 M, 0.01 M and 0.001 M NaCl solutions

The pitting potential is reported to depend on logarithm of the chloride ion concentration,  $[Cl^-]$  [65,68,70,74,84,85]. For instance, Pride et al. studied relationship between the chloride ion concentration and the pitting potential for high purity aluminium. They found a fit with a slope of approximately -0.11 V/decade [65]. McCafferty also reported a logarithmic dependence for pure aluminium foil. Slope was found as -0.08 V/decade [86]. In the light of this information,  $E_{pit}$  versus logarithm of  $[Cl^-]$  graphs were sketched in Figure 4.13. The linear fits in the figure show that, for both alloys,  $E_{pit}$  varies with the logarithm of  $[Cl^-]$  in agreement with the literature. The slopes were calculated as -0.058 V/decade for the DCC alloy and -0.053 V/decade for the TRC alloy.

Gupta et al. found a pitting potential value for an AA5005-H34 as -433 mV in 10  $\mu$ M deaerated NaCl solution [64]. When the linear equation for the DCC sample is used to calculate the pitting potential for 10  $\mu$ M, it is found as -465 mV which is close to the result found by Gupta et al.

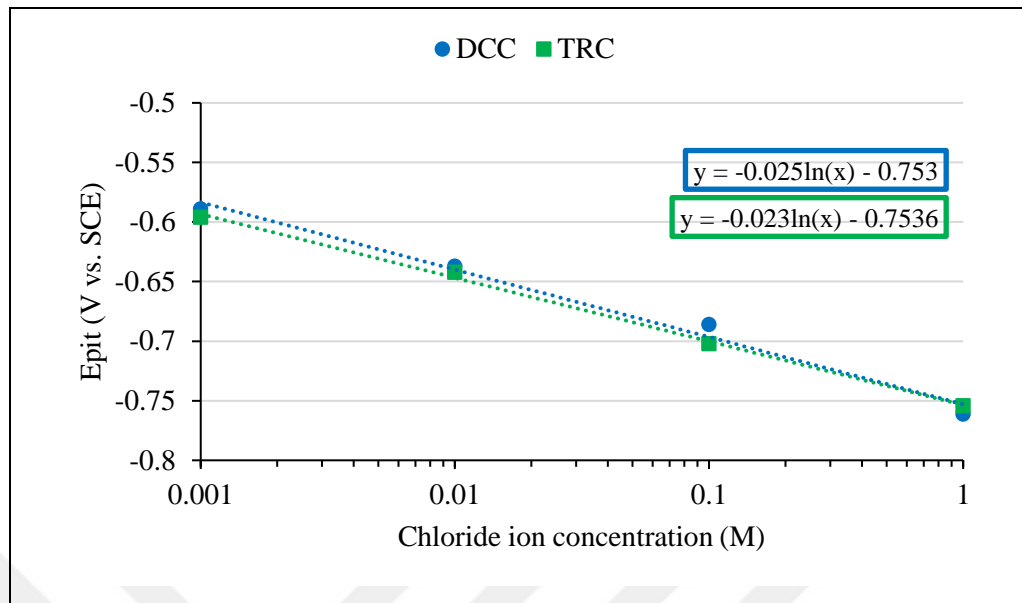


Figure 4.13.  $E_{pit}$  versus chloride ion concentration graph

Another critical potential that can be obtained from a CPP experiment is the repassivation potential ( $E_{repass}$ ). It is known that the growth of active pit(s) stops below the repassivation potential. A higher  $E_{repass}$  indicates that pits passivate at a more positive potential, thus, the material is more resistant to pit propagation. Table 4.3 shows average  $E_{repass}$  as well as  $i_{pass}$  for DCC and TRC aluminium samples.  $E_{repass}$  and  $i_{pass}$  values shown in the Table 4.3 are arithmetic averages of values found from experiments repeated under the same conditions.

Table 4.3.  $E_{repass}$  and  $i_{pass}$  values and their standard deviations

NaCl concentration	AA5005 DCC		AA5005 TRC	
	$E_{repass}$ (V)	$i_{pass}$ (mA/cm <sup>2</sup> )	$E_{repass}$ (V)	$i_{pass}$ (mA/cm <sup>2</sup> )
<b>1 M</b>	$-0.785 \pm 0.004$	$0.007 \pm 0.001$	$-0.787 \pm 0.004$	$0.005 \pm 0.001$
<b>0.1 M</b>	$-0.769 \pm 0.039$	$0.006 \pm 0.001$	$-0.861 \pm 0.013$	$0.003 \pm 0.001$
<b>0.01 M</b>	$-0.932 \pm 0.010$	$0.004 \pm 0.001$	$-0.918 \pm 0.01$	$0.003 \pm 0.001$
<b>0.001 M</b>	$-0.630 \pm 0.012$	$0.007 \pm 0.001$	$-0.817 \pm 0.115$	$0.004 \pm 0.001$

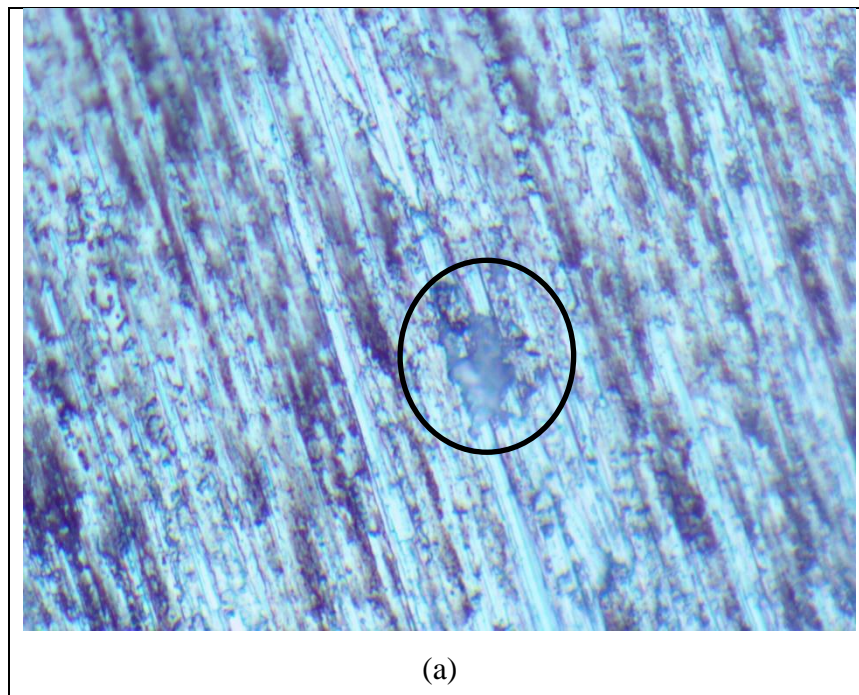
From the average  $E_{repass}$  results, it is seen that, generally, the repassivation potential decreases with decreasing chloride ion concentration between 1 M and 0.01 M for both AA5005 alloy sheets. Cicolin et al. [79] have also studied the chloride concentration impact on repassivation of 6082-T6 aluminium alloy. They have reported the same observation:

increasing the chloride ion concentration also increases the repassivation potential in nearly neutral medium (pH=6.5).

Brillas et al. [70] studied the electrochemical corrosion of homogeneous Al-Mg alloys in NaCl solutions. They studied with model alloys. It means that only alloying element is Mg and the alloy is totally homogeneous. They found the repassivation potential of an Al-Mg alloy containing 0.77 wt. per cent Mg as  $-0.715 \pm 0.1$  V vs. SCE in deaerated 0.1 M NaCl solution. However, aluminium alloys in this study have intermetallics in their structure. Such alloys have a heterogeneous structure. This may be the cause of the difference in the results.

If the 0.001 M CPP results are examined for both alloys (see Figure 4.11), it is seen that, for the TRC alloy, the forward and the reverse scans were very close to each other. The chosen method for  $E_{\text{repass}}$  determination depends on the intersection of these two curves. A much lower  $E_{\text{repass}}$  for the TRC alloy is likely to due to this (Table 4.3).

After the CPP measurements, surface of the electrodes were investigated by optical microscopy (NMM-800/820 Series Metallurgical Microscope). Figure 4.14 shows a representative pit image taken after a CPP measurement. Pit was marked with a black circle.



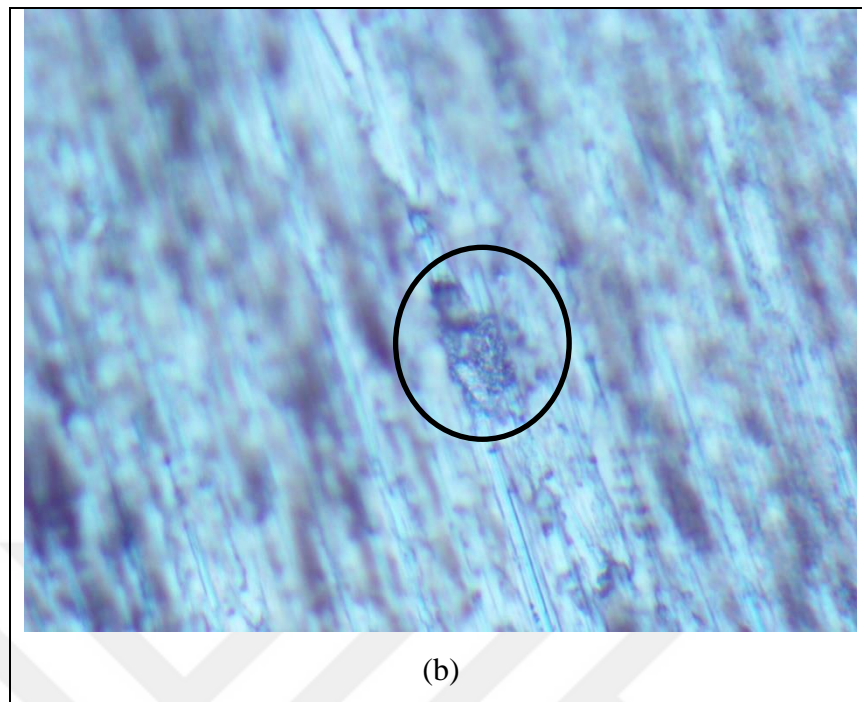
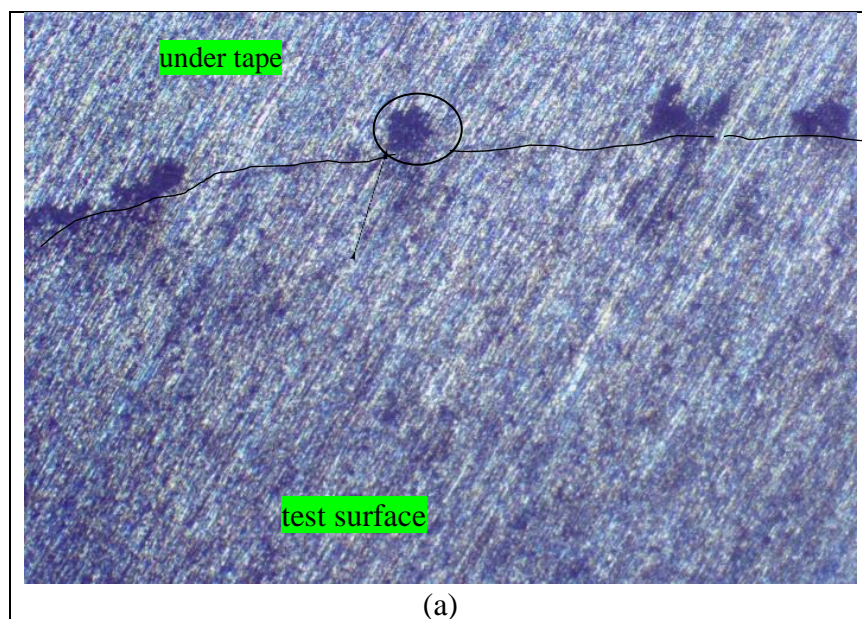


Figure 4.14. Representative pit image after a CPP experiment at 500x magnification (a) pit image (b) further zoom of pit

Tape boundary of working electrode was also analysed with an optical microscopy to check if there is any corrosion spots or not. This was done for checking whether the measurements were affected by the crevice corrosion. Figure 4.15 shows the optical images of a working electrode which contains corrosion spots on the tape boundary.





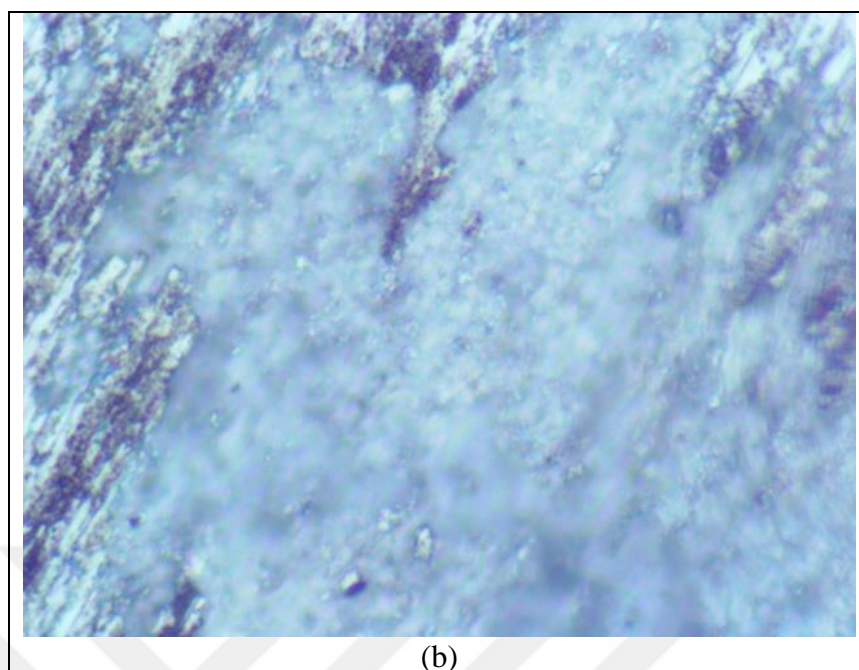


Figure 4.15. Optical images of working electrode after a CPP run (a) black line shows the tape boundary; magnification is 50x (b) image of the corrosion spot under the tape; magnification is 1000x

At 1000x, the spot (the foggy area seen in the image in Figure 4.15b) was seen as white structures, which are probably corrosion products. Afterwards, further CPP experiments were also performed to determine whether corrosion products form near the tape-test surface boundary after the current starts rising on the anodic sweep to check whether  $E_{\text{pit}}$  is effected by the crevice corrosion. In these measurements, the experiment was stopped at a given current value which was 20  $\mu\text{A}$  (after it was observed that the current increased rapidly) in the forward scan. Measurements were repeated three times to check the reproducibility. Figure 4.16 shows the surface image of the working electrode after such a CPP cut experiment. Black dash lines show the boundary of the electroplating tape. No corrosion spots were seen near or under the periphery of the electroplating tape. Thus, it could be said that  $E_{\text{pit}}$  values found from CPP measurements are not affected by the crevice effects; however  $E_{\text{repass}}$  values may be affected.

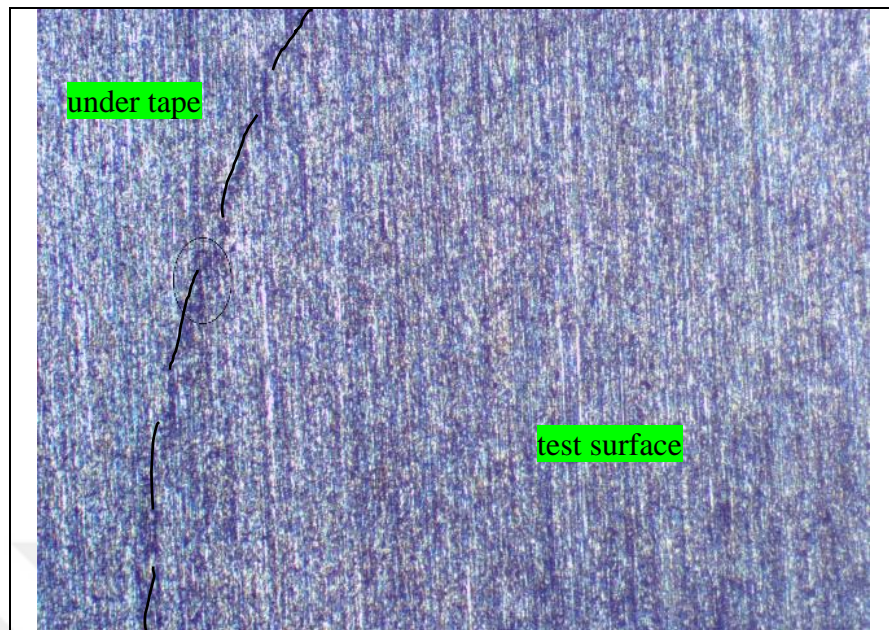


Figure 4.16. Image of the test surface after a CPP cut run

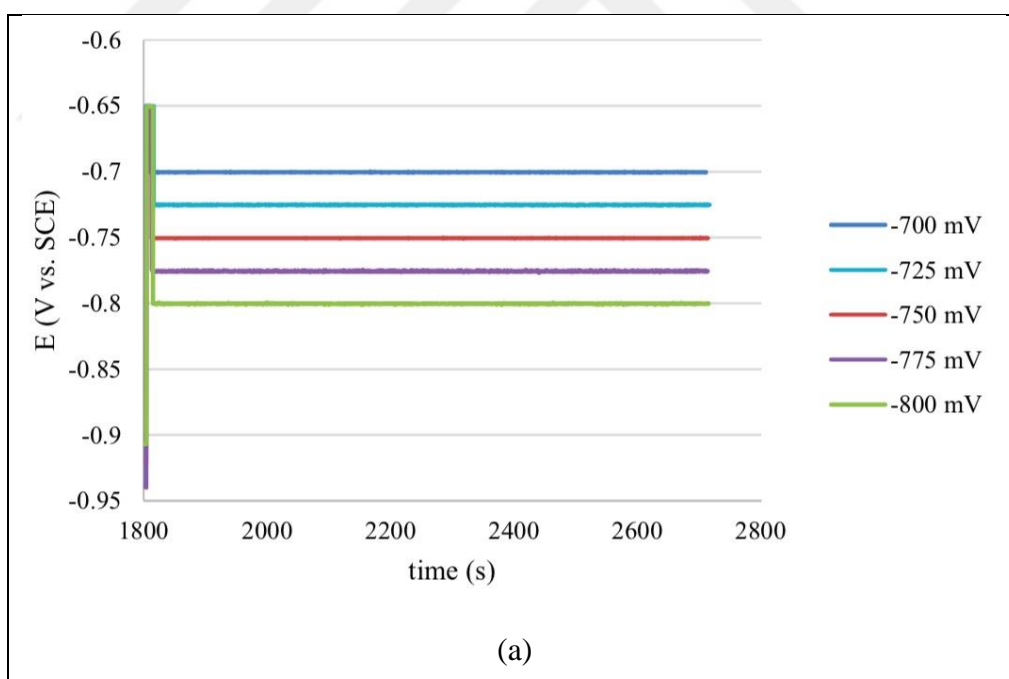
It is known that characteristic potentials found from CPP measurements such as  $E_{\text{pit}}$ ,  $E_{\text{repass}}$  etc. are affected by parameters such as potential scan rate and vertex current density [87]. Scully reported that the  $E_{\text{pit}}$  and  $E_{\text{repass}}$  are strong function of experimental test parameters. Another research established that when the vertex current (cut off limit or anodic current limit) increases, repassivation potential decreases [75].

#### 4.5. POTENTIOSTATIC MEASUREMENTS (PSM) FOR REPASSIVATION POTENTIAL ( $E_{\text{REPASS}}$ ) DETERMINATION

$E_{\text{repass}}$  is one of the characteristic potentials measured in localized corrosion studies. It is known that below the repassivation potential, growth of active pit stops. In this technique, firstly we applied an activation potential until 0.06 C charge passed. In the second step of the experiment, a lower potential was applied without any delay. When the average current density of the second step is below  $1 \mu\text{A}/\text{cm}^2$ , it could be said that growth of pits stopped [84]. Activation potentials for each chloride concentration was given in Table 3.2. These potentials are higher than the corresponding pitting potentials determined by the CPP measurement. From Figure 4.17 to Figure 4.19 show the applied potentials for 1 M, 0.1 M and 0.01 M NaCl solution, respectively. The loading times of the activation potentials vary according to the concentration. Chloride ion concentration prolongs the period of the

activation step. In other words, decreasing the chloride ion concentration increases the period of the activation step.

Before each experiment, the solution resistance,  $R_{\text{soln}}$ , was determined by impedance measurement. The solution resistance increases when the ion concentration decreases in the electrolytic solution. The measured  $R_{\text{soln}}$  values for both alloys in 0.01 M NaCl solution was around approximately 400 ~ 500 ohm while in 1 M NaCl it was 5 ~ 6 ohm. Figure 4.20 shows the potentials that are corrected for IR drop as a function of time for the DCC and TRC alloys in 0.01 M NaCl solution. Some differences in first two potentials (-550 and -600 mV) were observed between the Figure 4.19 and 4.20 due to high current. The pitting potentials for both alloys after the CPP experiments were found between -630 and -650 mV. First two applied potentiostatic steps (-550 mV and -600 mV) are more positive values than the pitting potentials. Thus, collected current data were high. As a result of this IR drop win solution was high too.



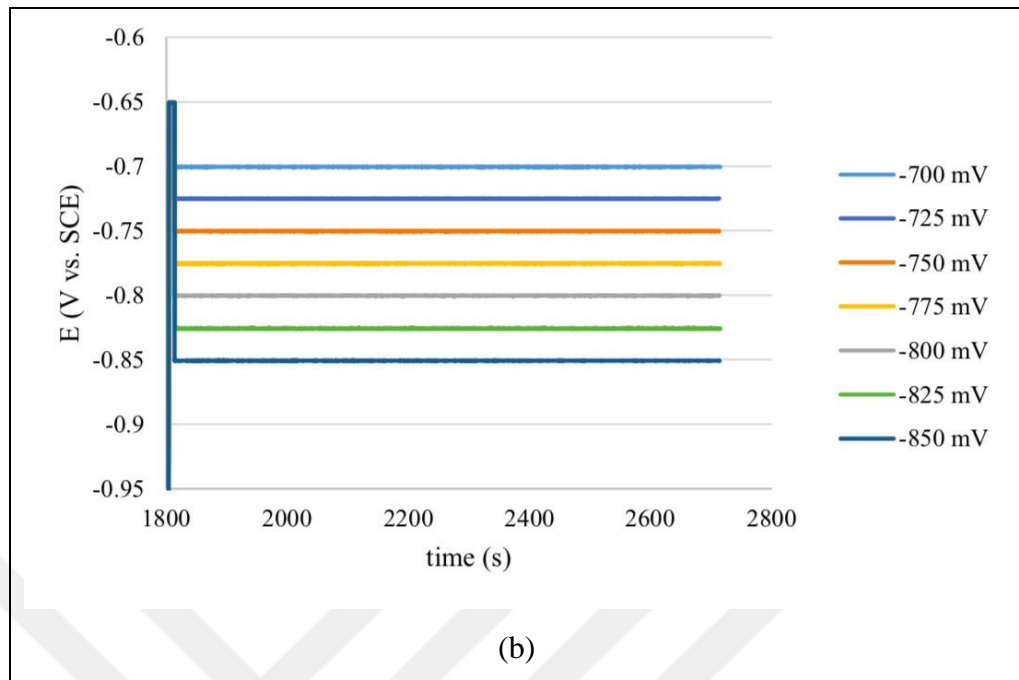
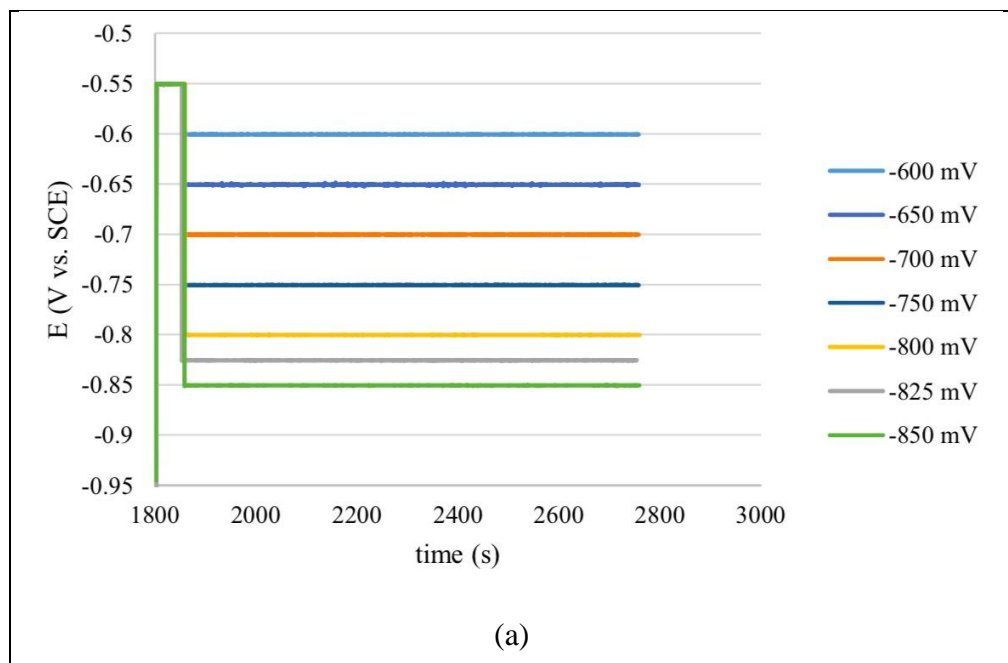


Figure 4.17. Applied potential versus time graph in 1 M NaCl solution for (a) DCC alloy  
(b) TRC alloy



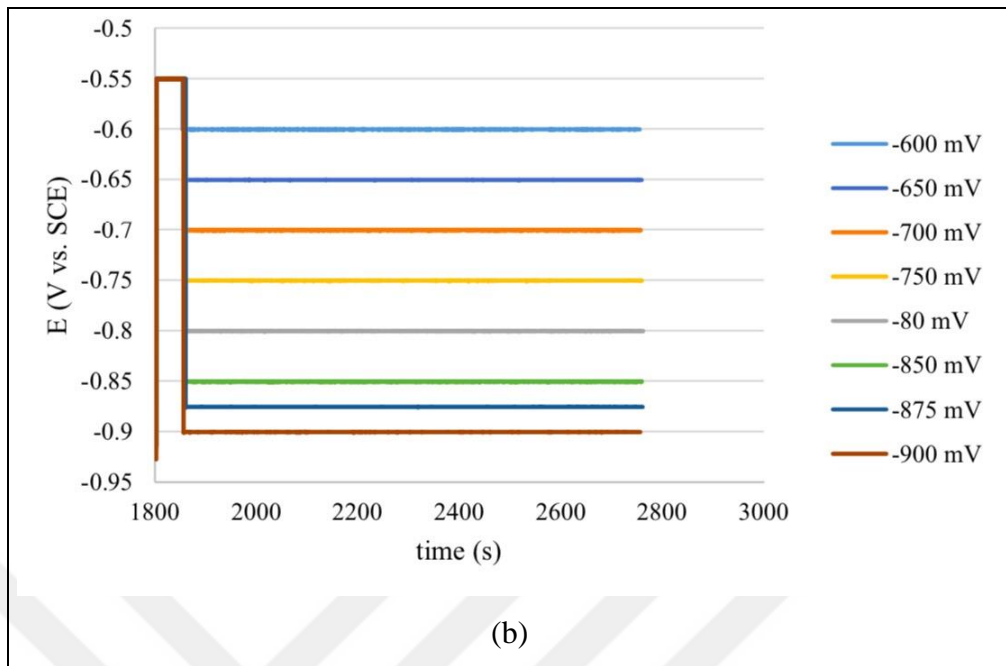
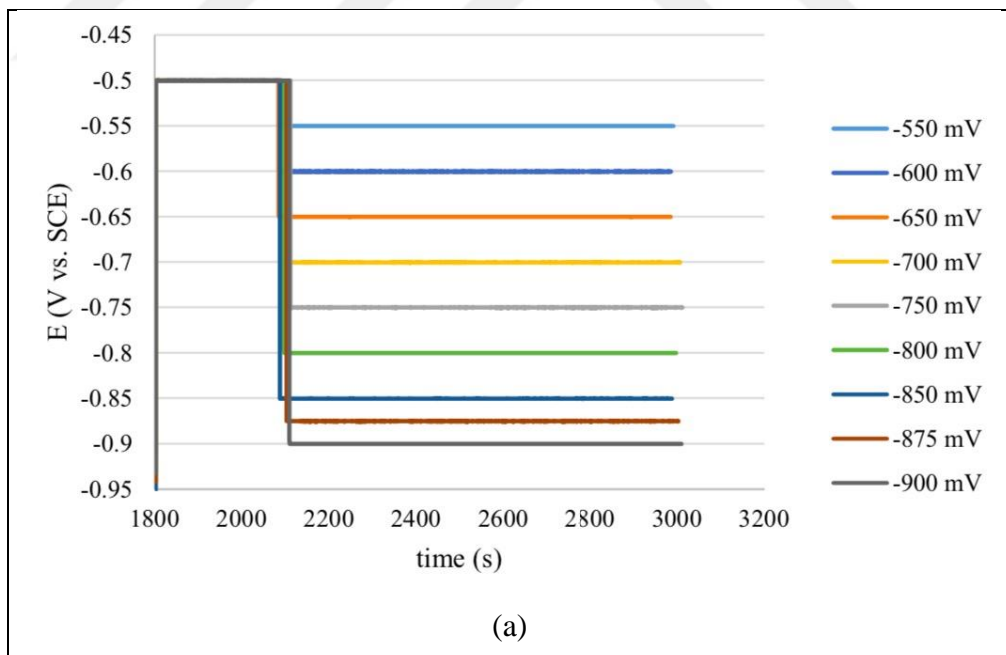


Figure 4.18. Applied potential versus time graph in 0.1 M NaCl solution for (a) DCC alloy  
(b) TRC alloy



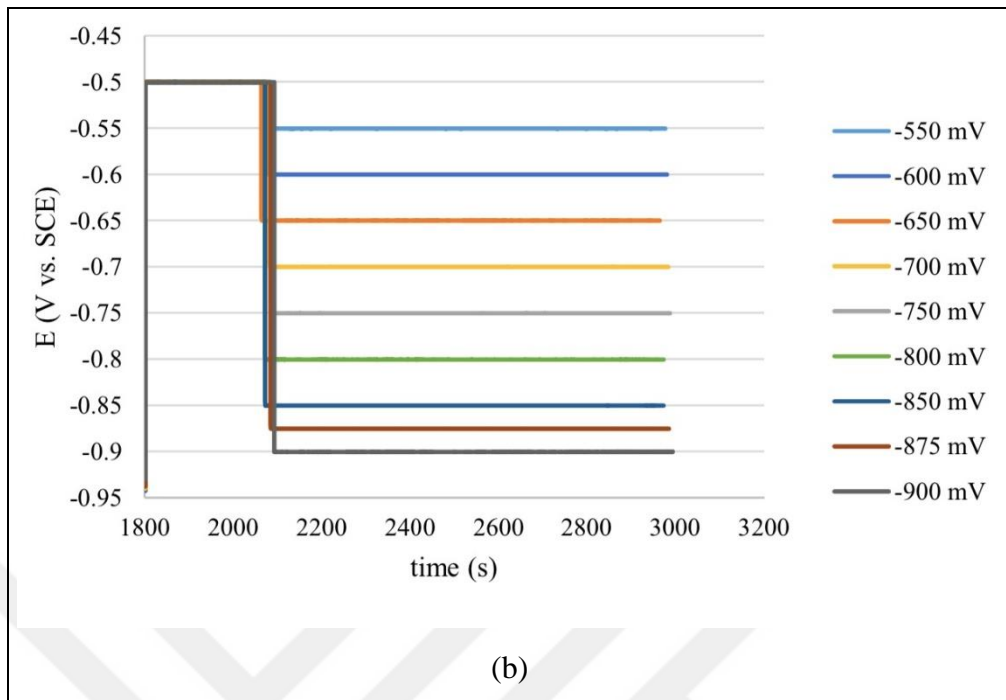
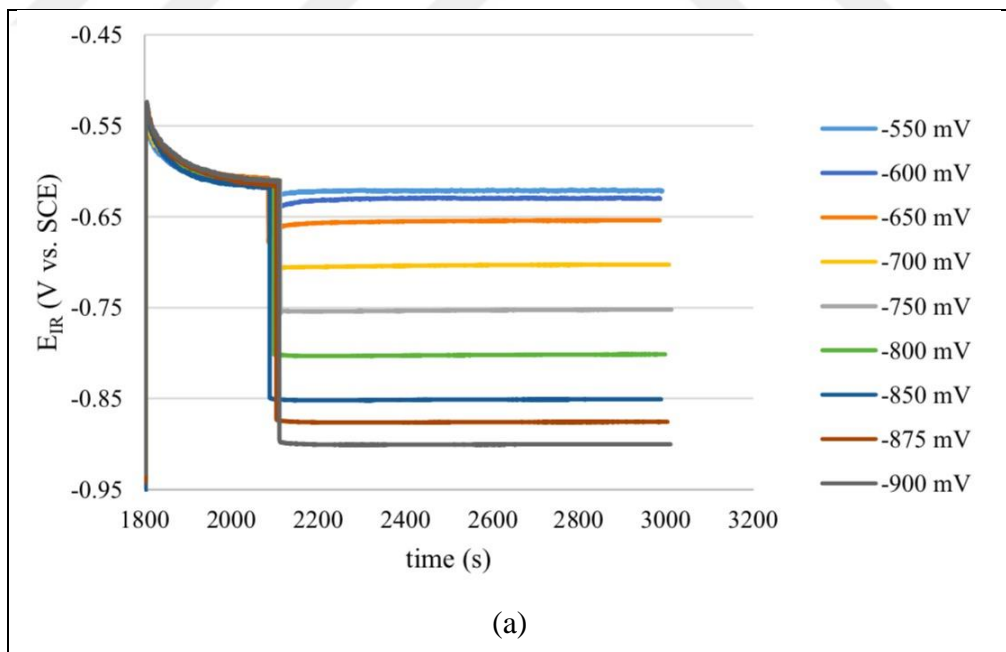


Figure 4.19. Applied potential versus time graph in 0.01 M NaCl solution for  
(a) DCC alloy (b) TRC alloy



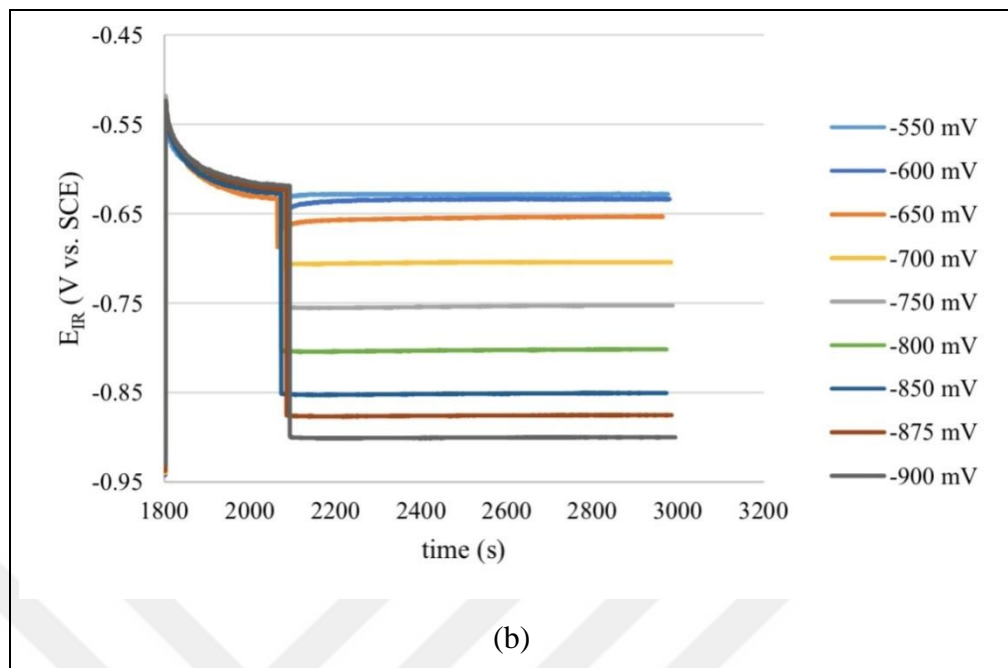


Figure 4.20. IR corrected potential,  $E_{IR}$ , versus time graph in 0.01 M NaCl solution for  
(a) DCC alloy (b) TRC alloy

During the experiments, potentiostat records the current. Current density versus time graphs are shown in Figure 4.21 to Figure 4.26. In these figures; (a) shows all results and (b) shows only those current density versus time plots near the  $1 \mu\text{A}/\text{cm}^2$  limit (shown as a horizontal line). At potentials that yields current densities below this limit, pits are assumed to passivate. The repassivation potential is between the most negative potential that yields a current density above this limit and the most positive potential that yields a current density below this limit. Thus, a potential range for the repassivation of the activated pits is determined. The current densities of the limits of the potential range for repassivation are given in (b) in these figures. Note that experiments of the potentials used to determine the repassivation range were repeated at least twice.

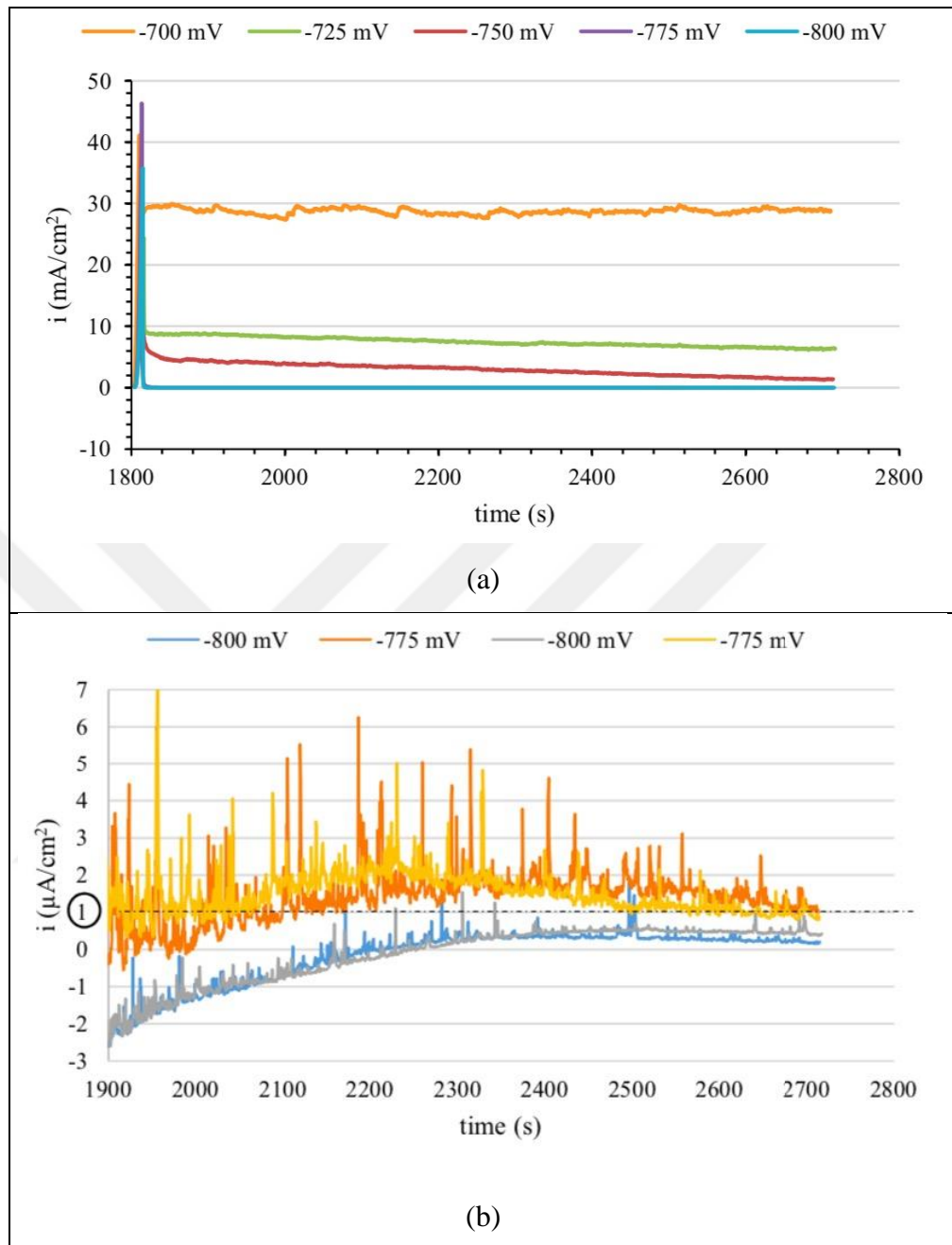


Figure 4.21. Current density vs time graph for DCC alloy in 1M NaCl solution (a) shows all results and (b) shows only those current density versus time plots near the 1  $\mu\text{A}/\text{cm}^2$  limit (shown as a horizontal line).



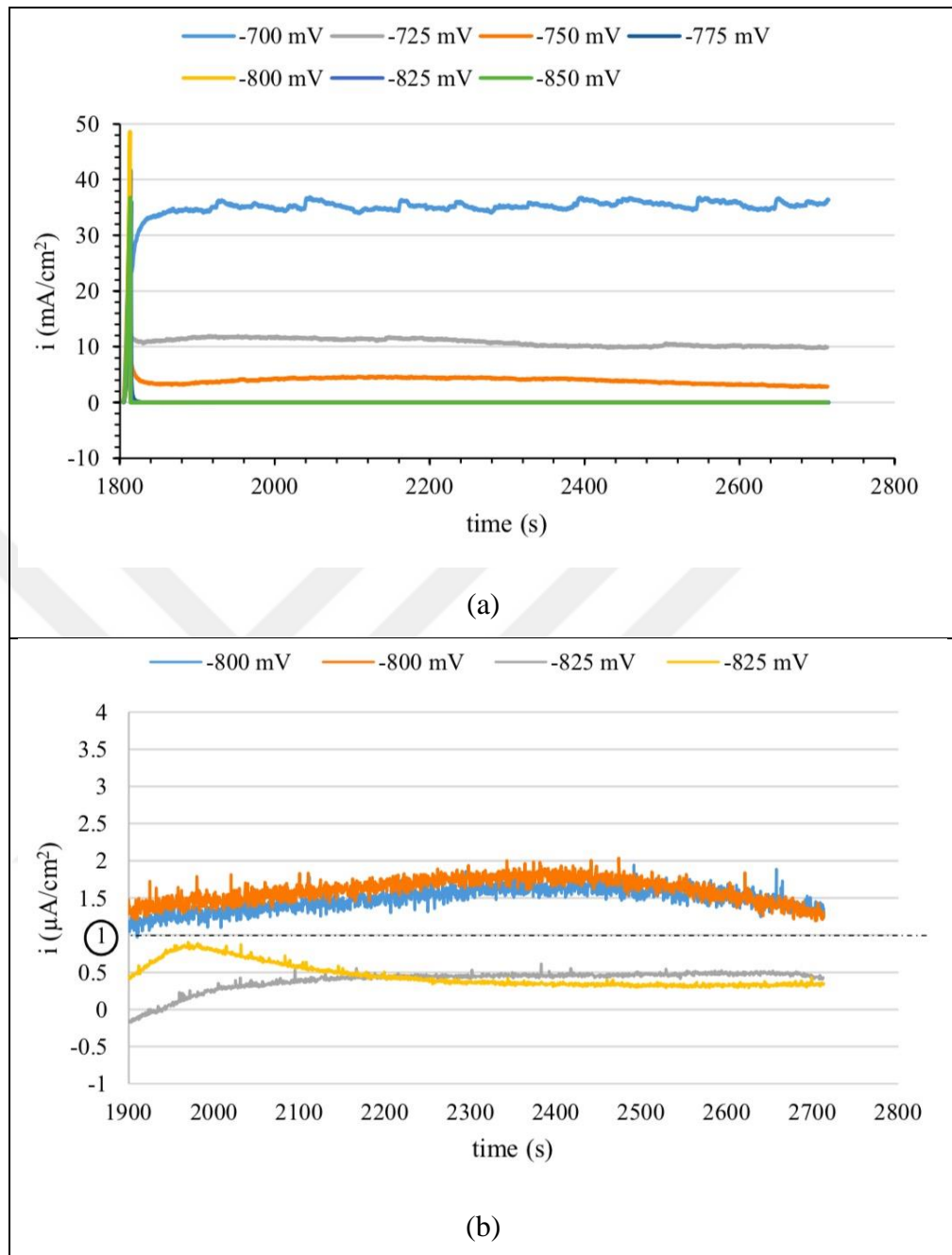


Figure 4.22. Current density vs time graph for TRC alloy in 1M NaCl solution (a) shows all results and (b) shows only those current density versus time plots near the 1  $\mu\text{A}/\text{cm}^2$  limit (shown as a horizontal line).

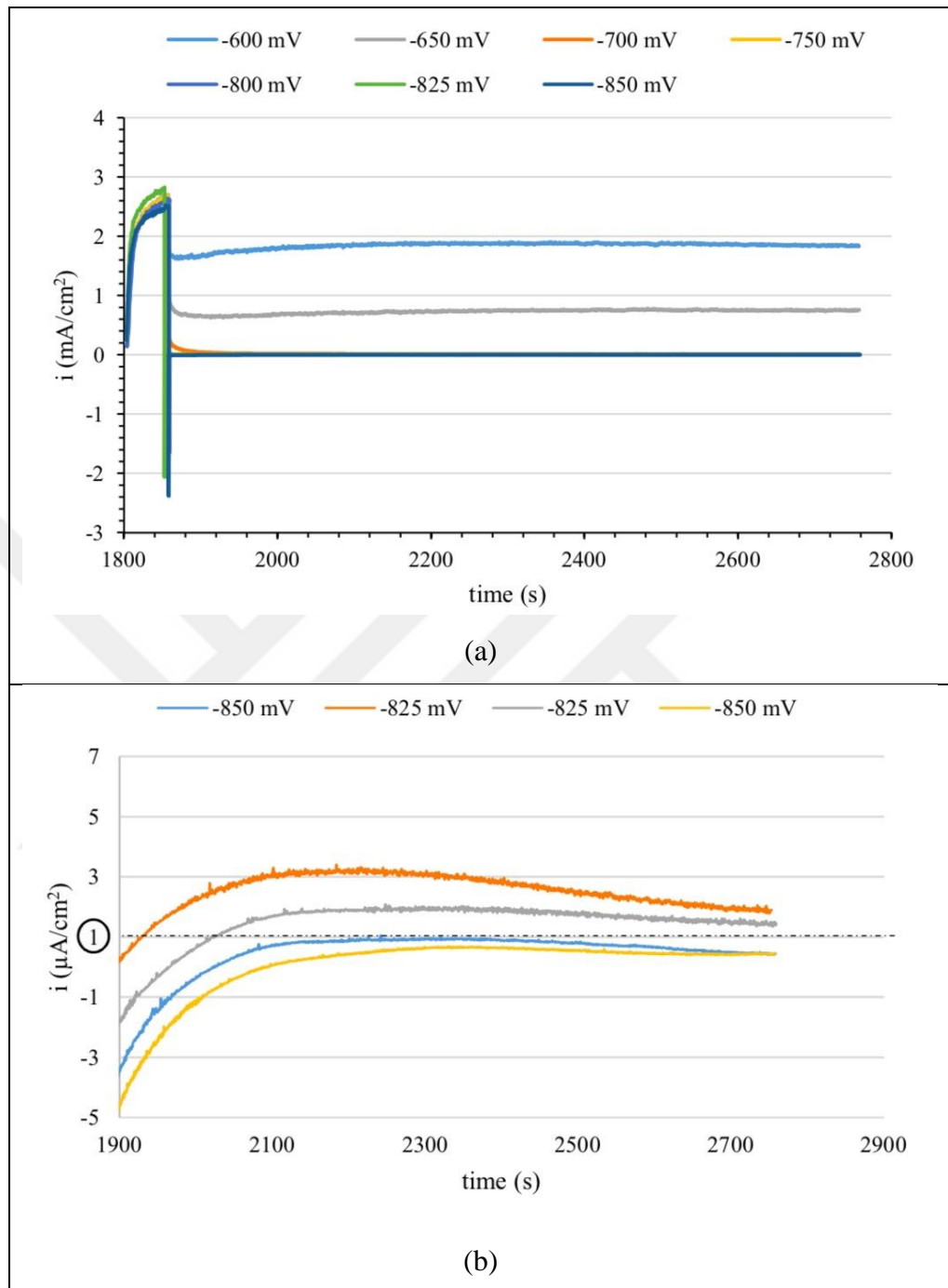


Figure 4.23. Current density vs time graph for DCC alloy in 0.1M NaCl solution (a) shows all results and (b) shows only those current density versus time plots near the 1  $\mu\text{A}/\text{cm}^2$  limit (shown as a horizontal line).

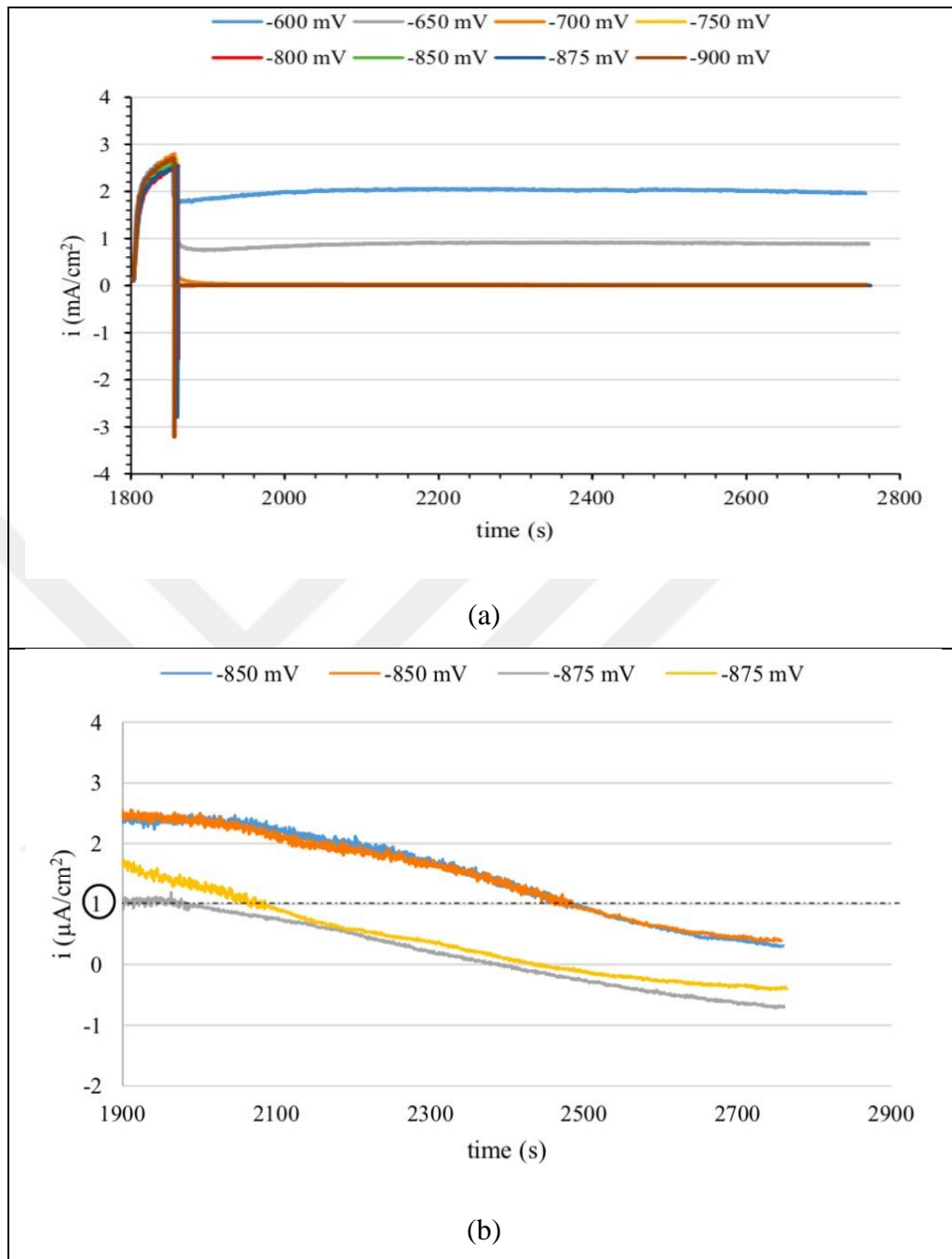


Figure 4.24. Current density vs time graph for TRC alloy in 0.1M NaCl solution (a) shows all results and (b) shows only those current density versus time plots near the 1  $\mu\text{A}/\text{cm}^2$  limit (shown as a horizontal line).

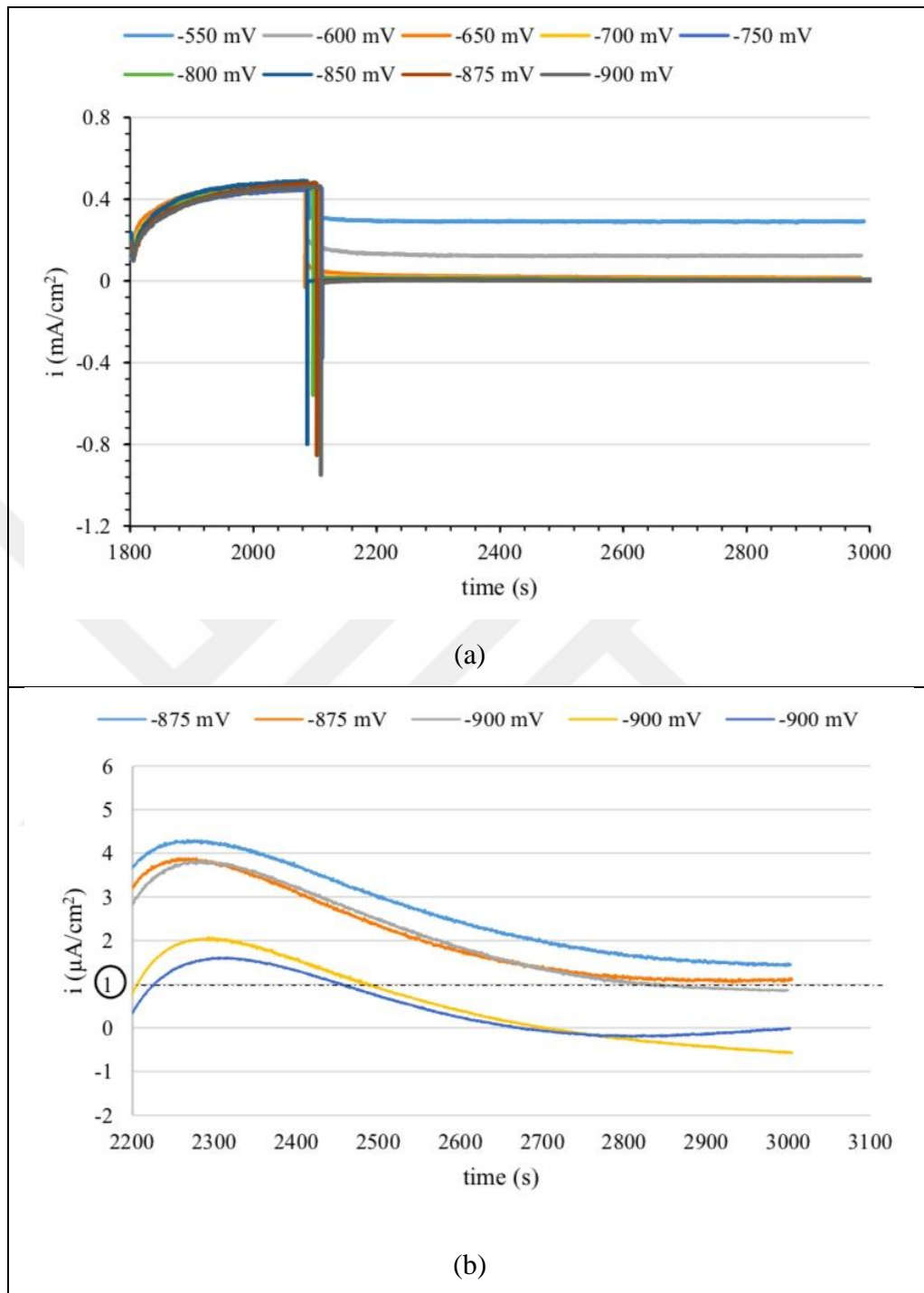


Figure 4.25. Current Density vs time graph for DCC alloy in 0.01M NaCl solution (a) shows all results and (b) shows only those current density versus time plots near the  $1 \mu\text{A}/\text{cm}^2$  limit (shown as a horizontal line).

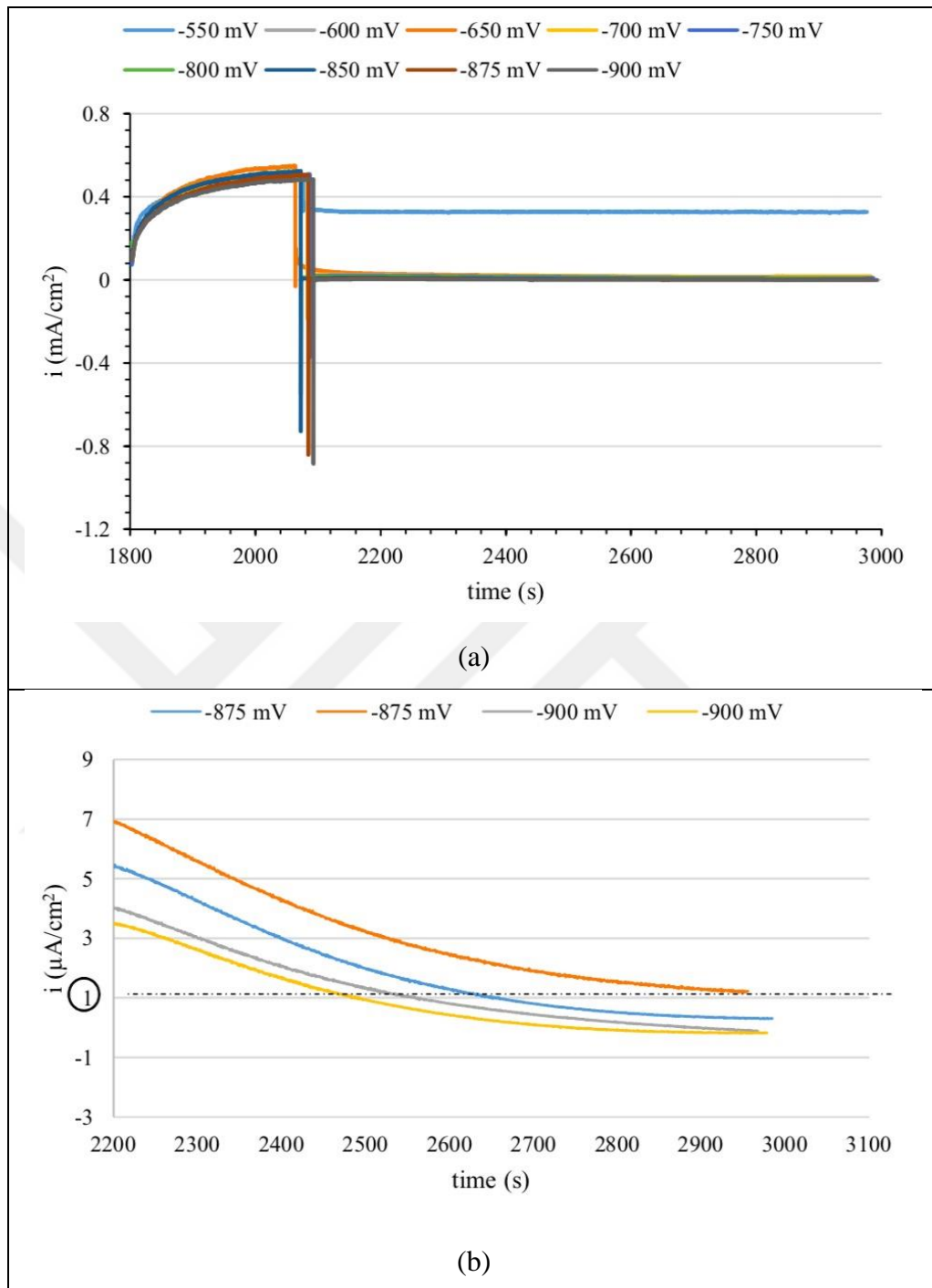


Figure 4.26. Current Density vs time graph for TRC alloy in 0.01M NaCl solution (a) shows all results and (b) shows only those current density versus time plots near the 1  $\mu\text{A}/\text{cm}^2$  limit (shown as a horizontal line).

Since the current densities were changing with time during potentiostatic steps, average current densities were calculated as follows. For 1 M NaCl solution average of the last 14.5 minutes, for 0.1 M NaCl solution average of the last 14 minutes and for 0.01 M NaCl solution average of the last 12 minutes was averaged.

Table 4.4 shows the repassivation potential results within a range of 25 mV. To make comparison, the potentials in the middles of the range will be taken as  $E_{\text{repass}}$  potentials.

Table 4.4. Repassivation potential range results

NaCl concentration (M)	Direct Casting, DCC	Twin-roll Casting, TRC
	mV vs. SCE	
1	$-775 < E_{\text{repass}} < -800$	$-800 < E_{\text{repass}} < -825$
0.1	$-825 < E_{\text{repass}} < -850$	$-850 < E_{\text{repass}} < -875$
0.01	$-875 < E_{\text{repass}} < -900$	$-875 < E_{\text{repass}} < -900$

From Table 4.4, it is seen that there is a little difference between the DCC and TRC alloys. TRC alloys have a little bit lower (25 mV)  $E_{\text{repass}}$  value than DCC ones except in 0.01 M NaCl solution. For 0.01 M, same range was found;  $-875 < E_{\text{repass}} < -900$ . It is also seen that  $E_{\text{repass}}$  decreases with decreasing chloride ion concentration.

These results could be also compared with the  $E_{\text{repass}}$  values found from CPP measurements (Table 4.2). For 1 M NaCl solution,  $E_{\text{repass}}$  value for a DCC alloy was found as -785 mV from CPP measurement which is in the range found from potentiostatic technique ( $-775 \text{ mV} < E_{\text{repass}} < -800 \text{ mV}$ ). Moreover for 0.1 M NaCl solution,  $E_{\text{repass}}$  for a TRC alloy was found as -861 mV from CPP and the  $E_{\text{repass}}$  range was defined as  $-850 \text{ mV} < E_{\text{repass}} < -875 \text{ mV}$ . On the other hand, this is not the case at lowest concentration; 0.01 M. It should be noted that, CPP is a potentiodynamic technique. Potentiodynamic techniques have several defects due to the applied parameters [88,89]. Evans and Rebak [90] also reported that at less aggressive media, the reproducibility of  $E_{\text{repass}}$  values produced by CPP technique may not be high due to scan rate effect.

After the experiments, the region of the test surface near the boundary of the electroplating tape were investigated using the optical microscopy for possible occurrence of corrosion spots (crevice corrosion). Such spots were seen as white structures (Figure 4.15). Table 4.5

shows the optical microscopy results. The number of marks in each box is the number of samples checked under those conditions. - mark: no corrosion spots were observed near the boundary; + mark: at least one is seen; × mark: at least one seen under the tape near the boundary. Grey scale in Table 4.5 indicates  $E_{\text{repass}}$  ranges determined (Table 4.4). It is seen that the  $E_{\text{repass}}$  measurements in 1 M concentration are not likely to be affected by crevice corrosion. Diversely, at lower concentrations, crevice corrosion most probably affected the measurements, particularly for the DCC alloy.

Table 4.5. Optical microscopy results after potentiostatic measurements

NaCl conc.	Potential (mV)	DCC alloy	TRC alloy
<b>1 M</b> (% 5.7)	-700	×	+
	-725	×	+
	-750	×	+
	-775	-, -	-, -, +
	-800	+, -	-, -
	-825		-, -
	-850		-, -
<b>0.1 M</b> (% 0.57)	-600	×	×
	-650	×	×
	-675		
	-700	-	+
	-750	-	+
	-800	-	+
	-825	-, -	
	-850	×, ×	+, -
	-875		-, +
	-900		-

<b>0.01 M (% 0.057)</b>	-550	×	×
	-600	×	×
	-650	×	+
	-700	+	-
	-750	×	-
	-800	×	×
	-825		
	-850	+	+
	-875	×, ×	+, -
	-900	+, +, +, ×	×, -, -

#### 4.6. GALVANO-STAIRCASE CYCLIC POLARIZATION (GSCP) MEASUREMENTS

The aim of this experiment is to determine the breakdown potential,  $E_{bd}$ , and the protection potential,  $E_{prot}$ , using the galvano-static technique [63]. As opposed to the techniques discussed before in Sections 4.4 and 4.5, current is the controlled variable in GSCP. The current is increased like a staircase and the potential data are collected [91]. Potential controlled methods are strongly affected by induction time, hysteresis, scan rate effect and a charge effect while current controlled methods are not [63]. Figure 4.27 illustrates the applied current density ( $i$ ) versus time graph in this measurement. The current density was calculated by dividing the applied current with the test surface area ( $0.5 \text{ cm}^2$ ). Figure 4.28 (a) shows the collected potential versus time graph for a TRC sample in 0.1 M NaCl solution and (b) shows the zoom of the last 10 seconds of potential data collected at  $20 \mu\text{A}/\text{cm}^2$ .



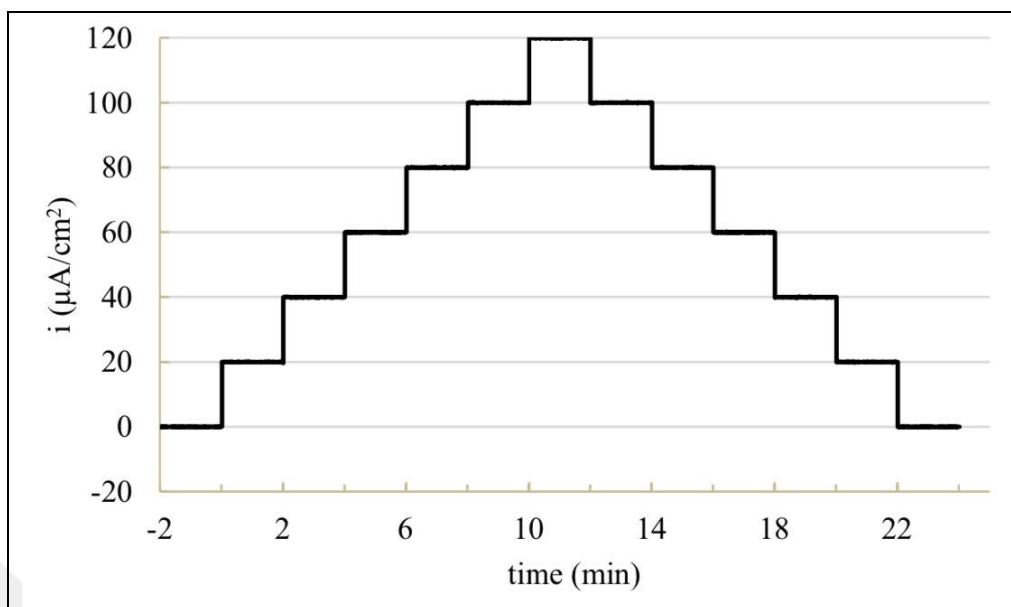
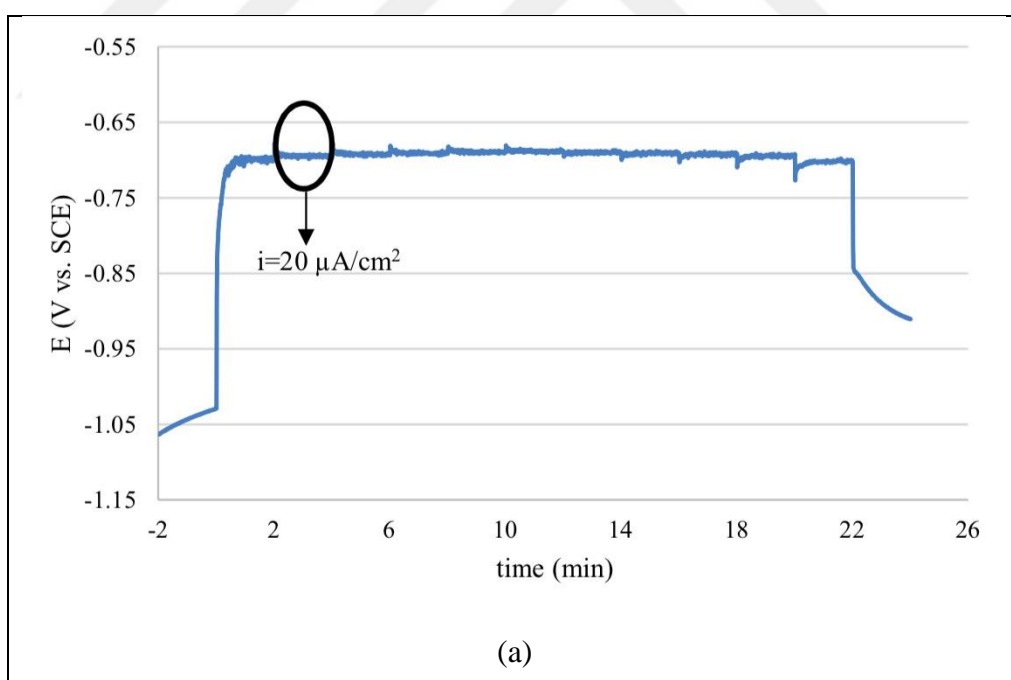


Figure 4.27. Representative current density graph for a GSCP measurement



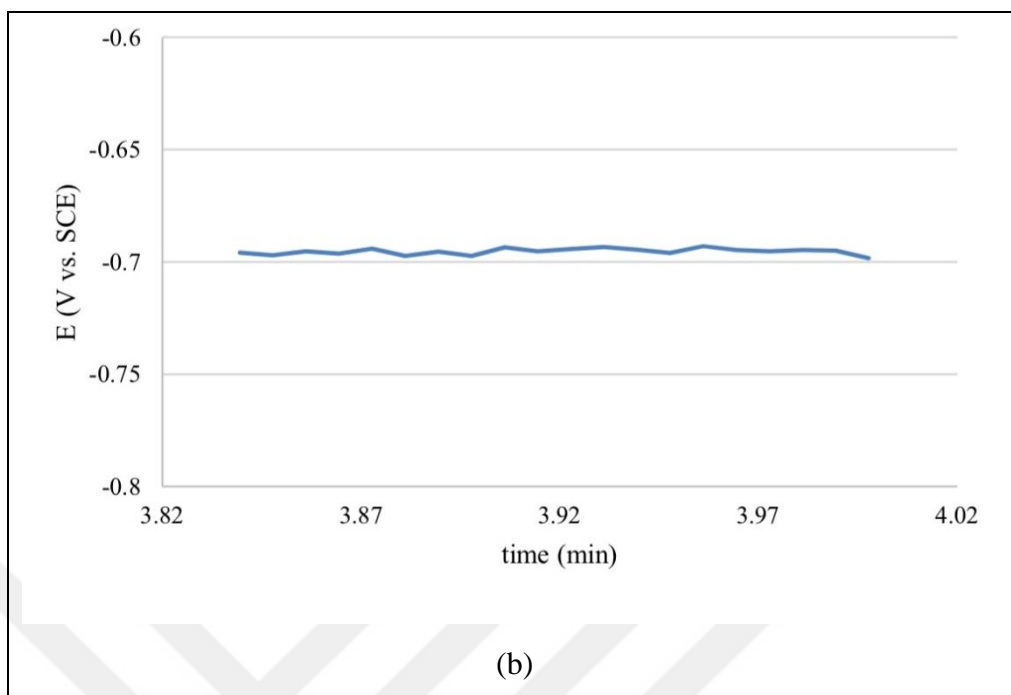


Figure 4.28.(a) Potential versus time graph for a TRC sample in 0.1 M NaCl solution and (b) shows the zoom of the last 10 seconds of potential data collected at  $20 \mu\text{A}/\text{cm}^2$

After each measurement, average potentials were calculated for the current steps by taking the arithmetic average of potential data recorded in the last ten seconds of the current step [91]. Figure 4.29 demonstrates the GSCP graph for the (a) DCC alloy and (b) TRC alloy in 1 M NaCl solution. The graph for 0.1 M and 0.01 M NaCl solutions are given in Figures 4.30 and 4.31, respectively. Each data point in these figures is an average potential calculated for the corresponding current step. Blue colour indicates the forward scan points and the orange colour indicates the reverse scan points. Five identical experiments were conducted for each alloy in each NaCl concentration. Graphs for the remaining four other measurements for each concentration are presented in Appendix B.

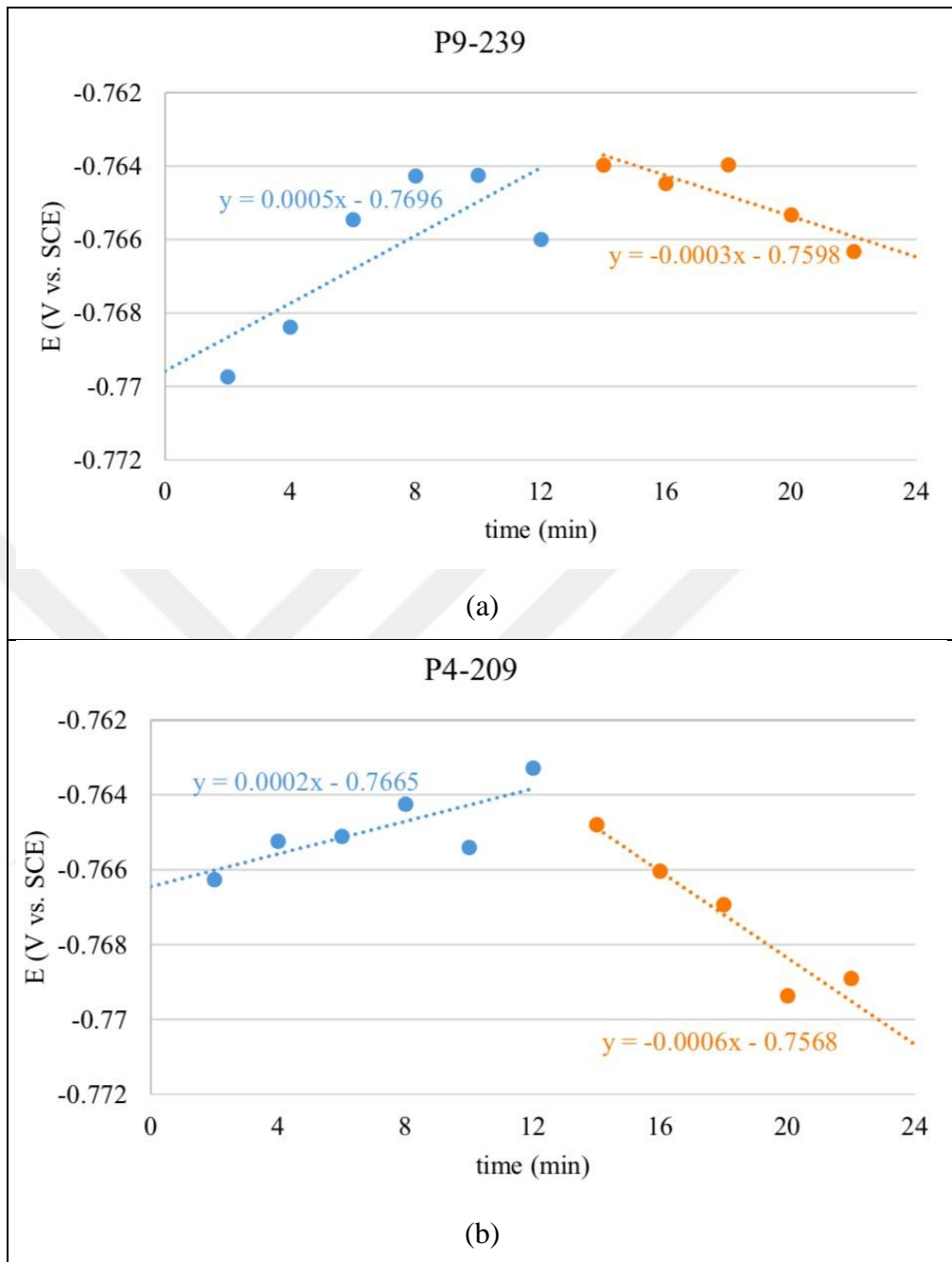


Figure 4.29. GSCP plot in 1 M NaCl solution for (a) DCC alloy (b) TRC alloy

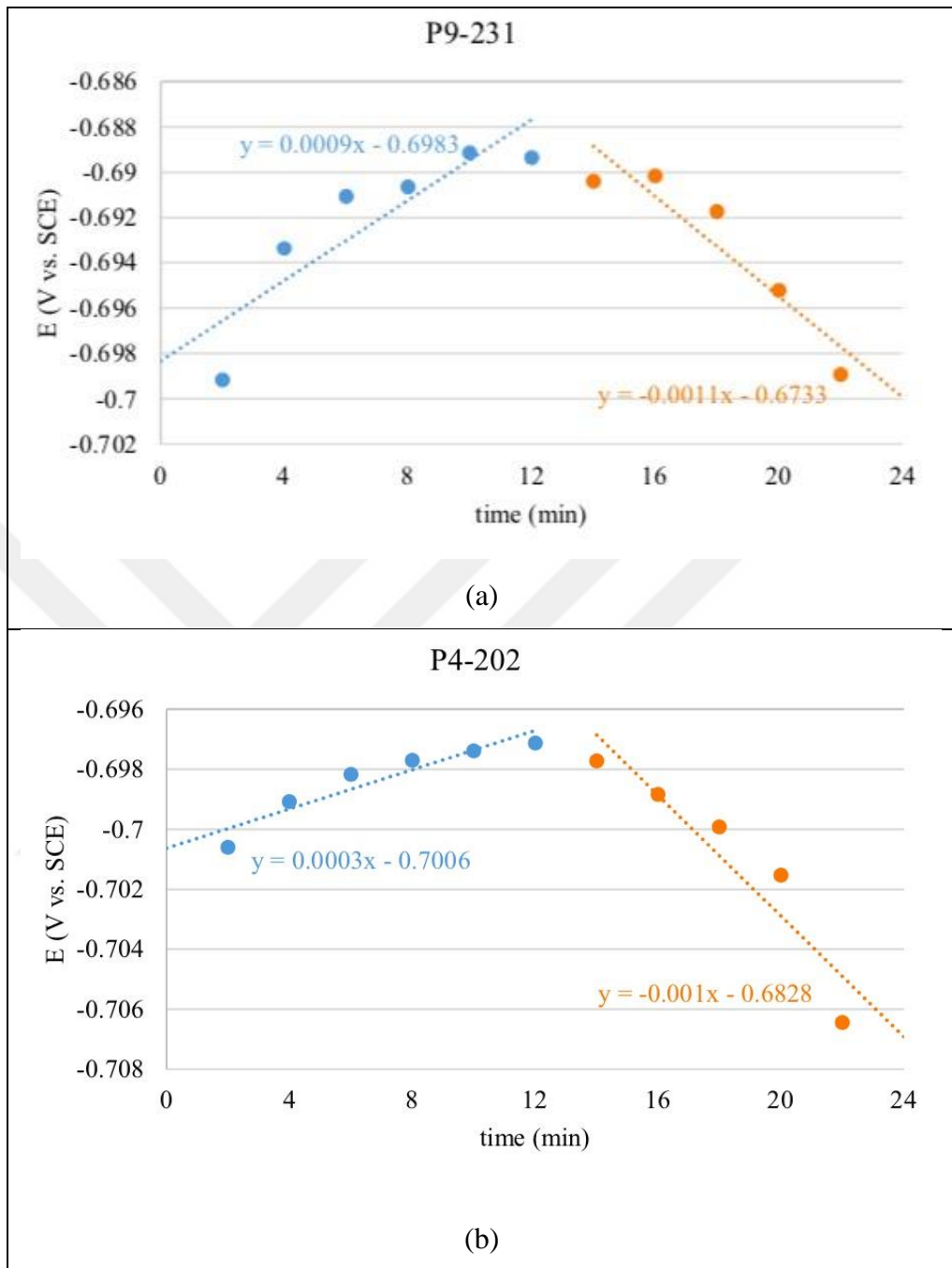


Figure 4.30. GSCP plot in 0.1 M NaCl solution for (a) DCC alloy (b) TRC alloy

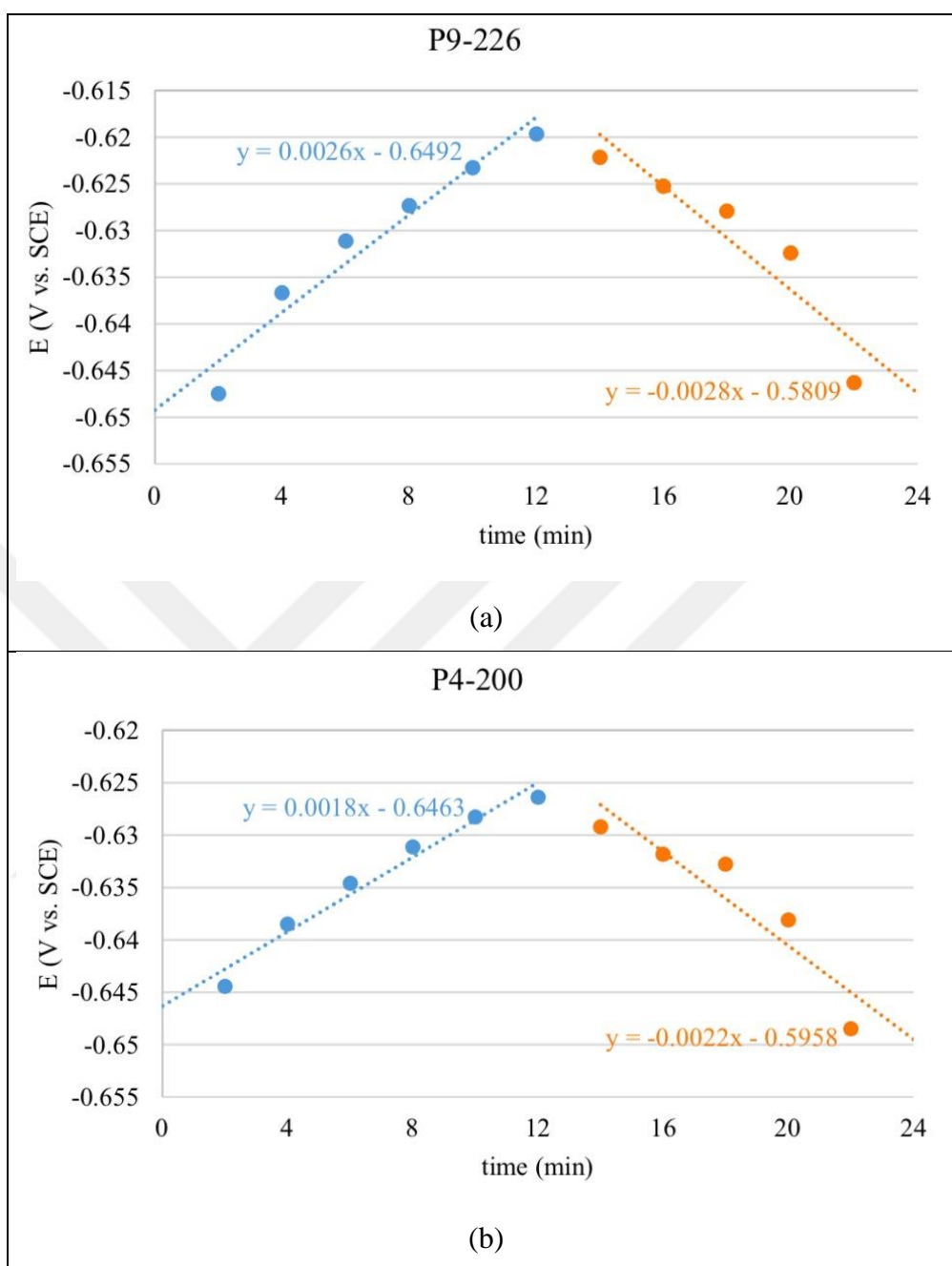


Figure 4.31. GSCP plot in 0.01 M NaCl solution for (a) DCC alloy (b) TRC alloy

After drawing GSCP graphs, the forward scan points were extrapolated to zero second to obtain breakdown potential,  $E_{bd}$ , and the reverse scan points were extrapolated to 24 minutes to obtain protection potential,  $E_{prot}$ . For instance, the breakdown potential was found as  $-0.701$  V and the protection potential was found as  $-0.702$  V for the TRC alloy in 0.1 M NaCl solution. The potentials  $E_b$  and  $E_{prot}$  are tabulated in Table 4.6. The results in Table 4.6 are the average of five measurements under the same conditions for each alloy in any concentration. For both the DCC alloy and the TRC alloy it can be said that both

breakdown potential and protection potential are decreased with decreasing the chloride ion concentration. It is well known from literature; chloride ions are highly aggressive ions that can degrade the passive film occurred on the electrode surface easier [12,79,80]. When the two alloys are compared with each other; there is not much more difference between their  $E_b$  and  $E_{prot}$  potentials. For example, in 1 M NaCl solution,  $E_{bd}$  for the DCC alloy was found as -765 mV and for the TRC alloy it was -766 mV while their  $E_{prot}$  values were found as -768 mV. It is also seen that the breakdown and protection potentials for a given alloy in any concentration are very close to each other. For instance, in 0.1 M NaCl solution, the difference between  $E_{prot}$  and  $E_b$  for a TRC alloy was only 3 mV. Hirozawa found similar result [63];  $E_{prot}$  and  $E_b$  for a metal or an alloy could be equivalent to each other when the medium is highly aggressive.

Table 4.6. Results obtained from GSCP measurement

NaCl conc.	Direct Casting, DCC		Twin-roll Casting, TRC	
	$E_b$ (V)	$E_{prot}$ (V)	$E_b$ (V)	$E_{prot}$ (V)
<b>1 M</b>	$-0.765 \pm 0.002$	$-0.768 \pm 0.004$	$-0.766 \pm 0.001$	$-0.768 \pm 0.001$
<b>0.1 M</b>	$-0.700 \pm 0.003$	$-0.704 \pm 0.006$	$-0.703 \pm 0.002$	$-0.706 \pm 0.003$
<b>0.01 M</b>	$-0.640 \pm 0.02$	$-0.648 \pm 0.01$	$-0.648 \pm 0.003$	$-0.656 \pm 0.007$

Another comparison could be done with breakdown potential found in GSCP measurement (Table 4.6) and pitting potential results found in CPP measurement (Table 4.2). Table 4.7 shows both results and the difference between these two potentials. As it can be understood from table, both methods gave close results. Highest difference was seen for a DCC alloy in 0.1 M NaCl solution which was 14 mV.

Table 4.7. Comparison of GSCP and CPP results

Type of an alloy	NaCl conc.	$E_b$ (V) found from GSCP	$E_{pit}$ (V) found from CPP	$\Delta E$ (mV)
<b>Direct Casting (DCC)</b>	<b>1 M</b>	$-0.765 \pm 0.002$	$-0.761 \pm 0.009$	4
	<b>0.1 M</b>	$-0.700 \pm 0.003$	$-0.686 \pm 0.010$	14
	<b>0.01 M</b>	$-0.640 \pm 0.02$	$-0.637 \pm 0.008$	3

<b>Twin-roll Casting (TRC)</b>	<b>1 M</b>	$-0.766 \pm 0.001$	$-0.754 \pm 0.006$	12
	<b>0.1 M</b>	$-0.703 \pm 0.002$	$-0.702 \pm 0.006$	1
	<b>0.01 M</b>	$-0.648 \pm 0.003$	$-0.642 \pm 0.012$	6

Table 4.8 shows the optical microscopy results done after the GSCP measurements for crevice corrosion control. The number of marks in each box is the number of samples checked under those conditions. - mark: no corrosion spots were observed; + mark: at least one seen on the periphery of the tape; × mark: at least one seen under the tape. Note that only three samples were examined at 0.1 M and 0.01 M chloride ion concentration. Although the critical potentials determined for the TRC alloy at 0.1 M and 0.01 M are not affected by the crevice effects, the DCC alloys seems to be effect. On the other hand, there seems to be no difference between the critical potentials of the two alloys in all three concentrations (Table 4.6).

Table 4.8. Optical microscopy results done after the GSCP measurements

<b>NaCl concentration</b>	<b>DCC alloy</b>	<b>TRC alloy</b>
1 M (% 5.7)	×, ×, ×, ×, ×	+, ×, +, ×, ×
0.1 M (% 0.57)	+, ×, ×	+, -, -
0.01 M (% 0.057)	+, ×, ×	-, -, -

#### **4.7. METASTABLE PITTING CORROSION MEASUREMENTS UNDER POTENTIOSTATIC CONDITIONS**

The aim of this experiment is to determine the number of metastable pits occurred at the electrode surface under potentiostatic conditions and to compare the two types of AA5005 alloys produced by different production techniques, DCC and TRC. A metastable pit is a pit grows for a limited period before repassivating. Metastable pits can form at potentials below  $E_{pit}$  and during the induction time before the onset of stable pitting [92]. Metastable pits cause small peaks of current above the background level during a potentiostatic run [65,82,93]. After a short time, the current returns to its base line. In other words, metastable pits grow for a short-time and then they repassivate. Metastable pits are studied extensively

since the probability of stable pitting is found to be related to the metastable pitting rate [94,95].

In this technique, three potentiostatic runs were done for each alloy type. Applied potentials were 50 mV, 75 mV and 100 mV below the pitting potentials of the alloys (Table 4.9). In other word, the alloys were compared at constant underpotentials (50 mV, 75 mV or 100 mV) with respect to their own  $E_{pit}$ . Gupta used this approach to compare the resistances to pitting corrosion of pure aluminium, AA2024, AA5005, AA5083, AA6022 and AA7075 alloys [64]. Note that, in highly aggressive media, there would be so many metastable pitting events, which could be hard to analyse. Hence, the measurements were done in relatively dilute solutions, which were 0.01 and 0.001 M NaCl solutions.

Table 4.9. Applied potentials ( $E_{app}$ ) depending on the pitting potentials

	<b>Applied Potential (mV)</b>			
	<b>AA5005 DCC</b>	<b>AA5005 TRC</b>	<b>AA5005 DCC</b>	<b>AA5005 TRC</b>
	<b>0.01 M NaCl</b>		<b>0.001 M NaCl</b>	
$E_{pit}$	-637	-642	-589	-596
50 mV below $E_{pit}$	-687	-692	-639	-646
75 mV below $E_{pit}$	-712	-717	-664	-671
100 mV below $E_{pit}$	-737	-742	-689	-696

Each potentiostatic run was repeated three times. It should be note that each repeat starts with, a new coupon and, hence, with a different surface. Therefore, there are differences between the repeats. Figure 4.32 shows the results for (a) DCC alloy and (b) TRC alloy in 0.01 M NaCl solution and Figure 4.33 presents the results in 0.001 M NaCl solution. Only one representative plot of the three identical experiments were given. Other two repetitions are given in Appendix C. Current density peaks above the base current densities in these figures shows metastable pitting events. As can be seen from these figures, the intensity of metastable pitting generally decreases as the applied potential was decreased. Similarly, Gupta et al. reported that, when the applied potential gets closer to  $E_{pit}$ , the intensity of the metastable pitting events increases [64]. Moreover, for all potentials, it is seen that metastable pitting activity was highest during about the initial 500 seconds. Figure 4.34 presents a zoom of Figure 4.32, and Figure 4.35 presents a zoom of Figure 4.33 to show



individual metastable pitting events. Arrows in each figure point out the representative metastable pitting events.

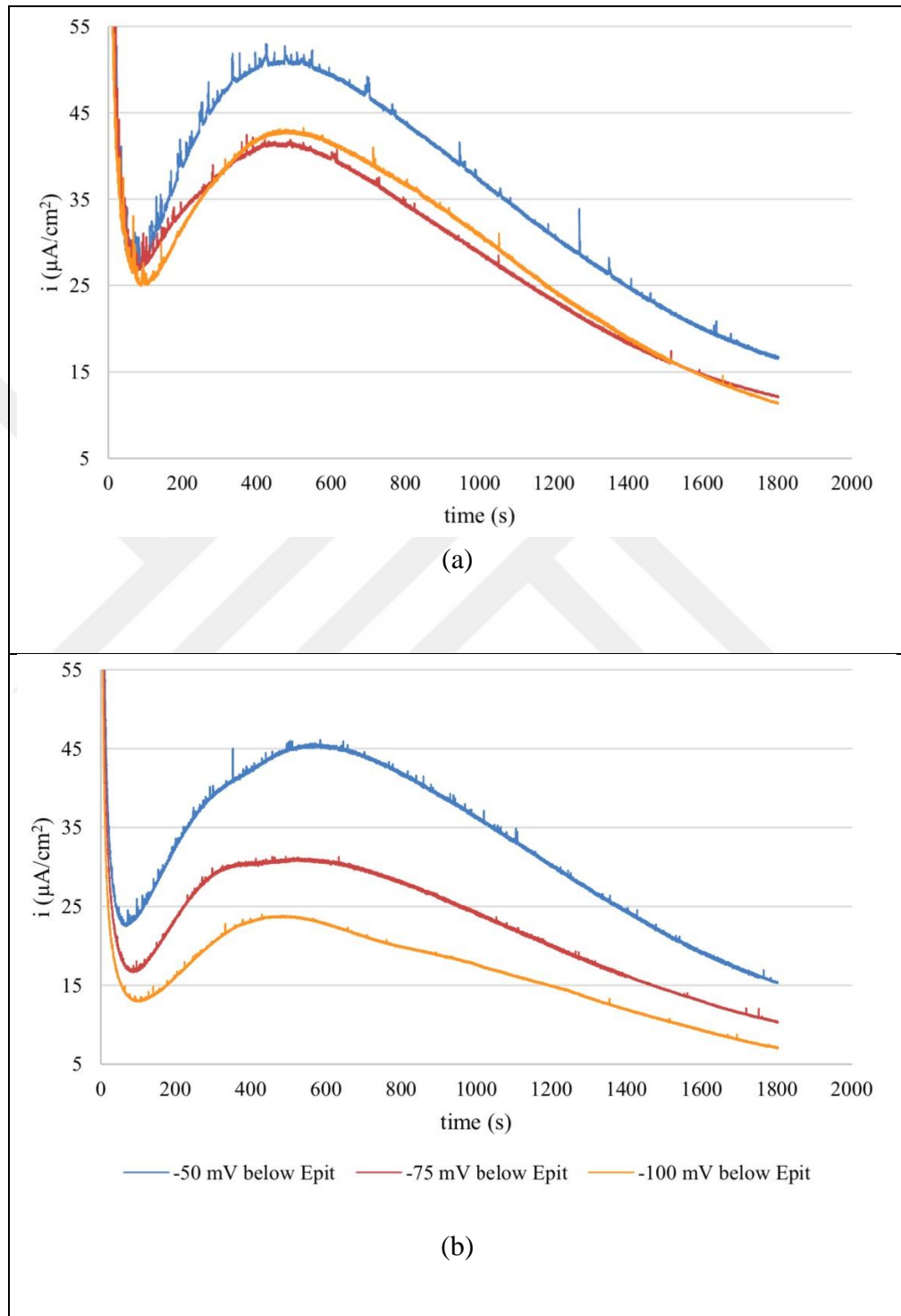


Figure 4.32. Metastable pitting corrosion measurement results in 0.01 M NaCl solution  
(a) DCC alloy (b) TRC alloy

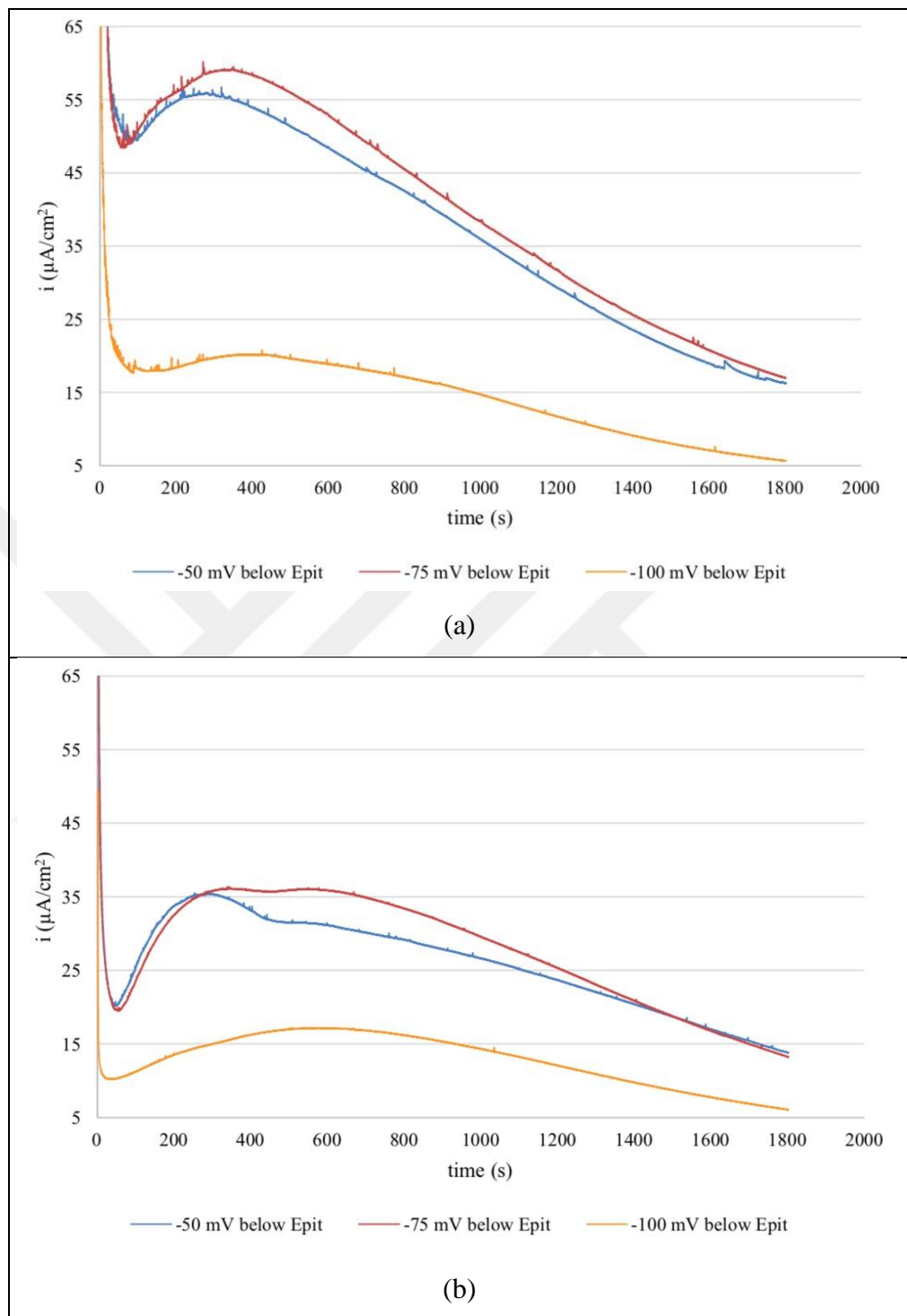


Figure 4.33. Metastable pitting corrosion measurement results in 0.001 M NaCl solution  
(a) DCC alloy (b) TRC alloy

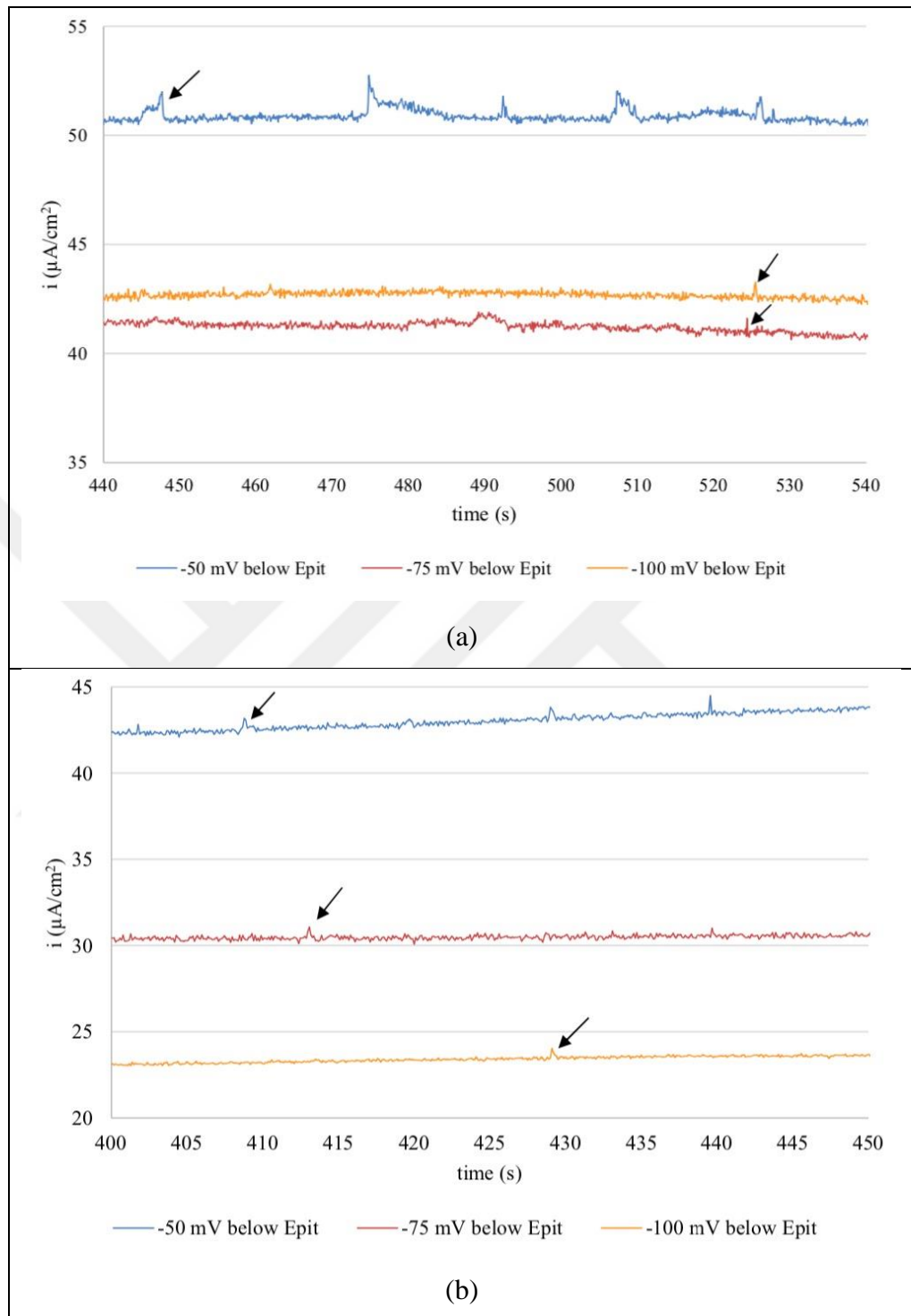


Figure 4.34. Zoom of current density data seen on Figure 4.32 in 0.01 M NaCl solution  
(a) DCC alloy (b) TRC alloy

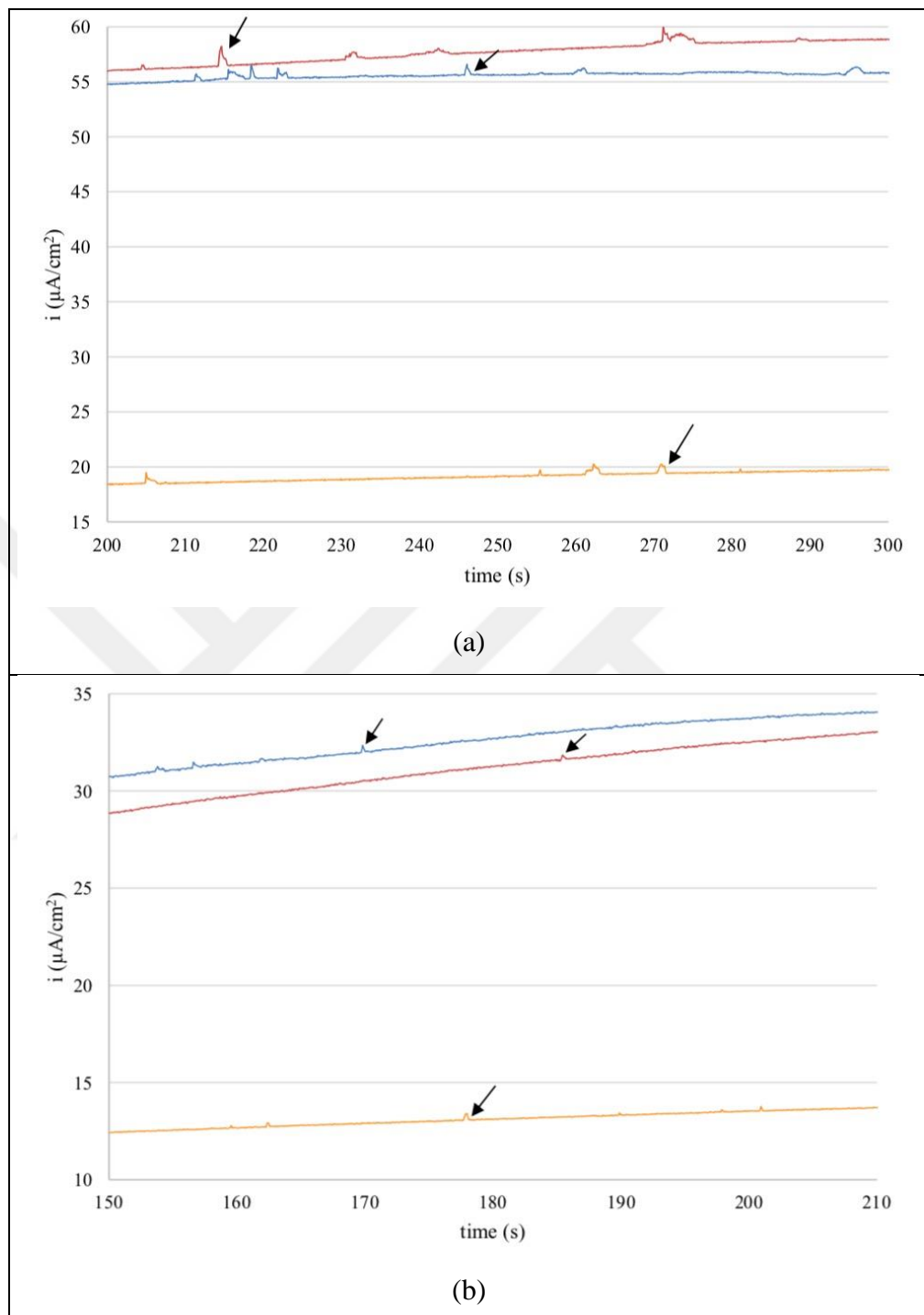


Figure 4.35. Zooming of current density data seen on Figure 4.33 in 0.001 M NaCl solution  
(a) DCC alloy (b) TRC alloy

After the experiments, metastable pits were counted depending on the criteria: to be counted as a metastable pit, a peak should have a current increase of at least 4 nano amperes and it has to return to the baseline. Figure 4.36 illustrates a schematic peak and some crucial parameters that were encountered during the pit analysis. Maximum point of a peak is denoted

by  $i_{\max}$ , starting time of a peak (also called pit initiation) is denoted by  $t_i$  and finishing time (also called pit termination) is denoted by  $t_f$ . The peak shown in Figure 4.36 has a current increase of  $4 \mu\text{A}/\text{cm}^2$ . Electrode area was  $0.03 \text{ cm}^2$ . So, it is equal to  $120 \text{ nA}$ . Thus, it could be said that it is a current transient of a metastable pit.

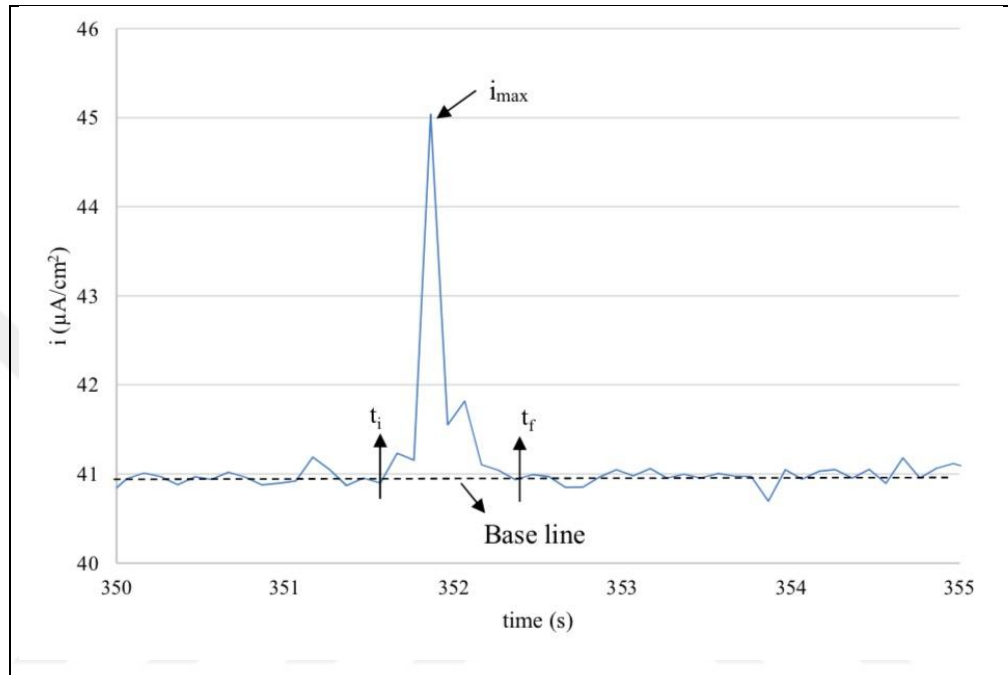


Figure 4.36. Schematic representation of a peak

First 10 seconds of the current data was not considered due to very fast change of the base current (Figure 4.32 and 4.33). Table 4.10 shows the number of metastable pits for both alloys in both solutions as a function of underpotentials. Note that average of the three measurements under the same conditions (but each with a new coupon) is reported. Depending on the Table 4.10, the number of metastable pits generally decreased with the increasing potential difference between  $E_{\text{app}}$  and  $E_{\text{pit}}$  (that is, as the underpotential increased).

Table 4.10. Number of metastable pits

	0.01 M NaCl		0.001 M NaCl	
	DCC alloy	TRC alloy	DCC alloy	TRC alloy
50 mV below $E_{\text{pit}}$	67	71	46	42
75 mV below $E_{\text{pit}}$	42	31	51	31
100 mV below $E_{\text{pit}}$	39	34	30	12

Metastable pitting rates (MPR, events/cm<sup>2</sup>/min) were also calculated. Metastable pitting rate was calculated by dividing the number of metastable pits by the surface area (0.03 cm<sup>2</sup>) and by the measurement period (30 minutes) [64]. Figure 4.37 presents the metastable pitting rate as a function of underpotential from E<sub>pit</sub>.

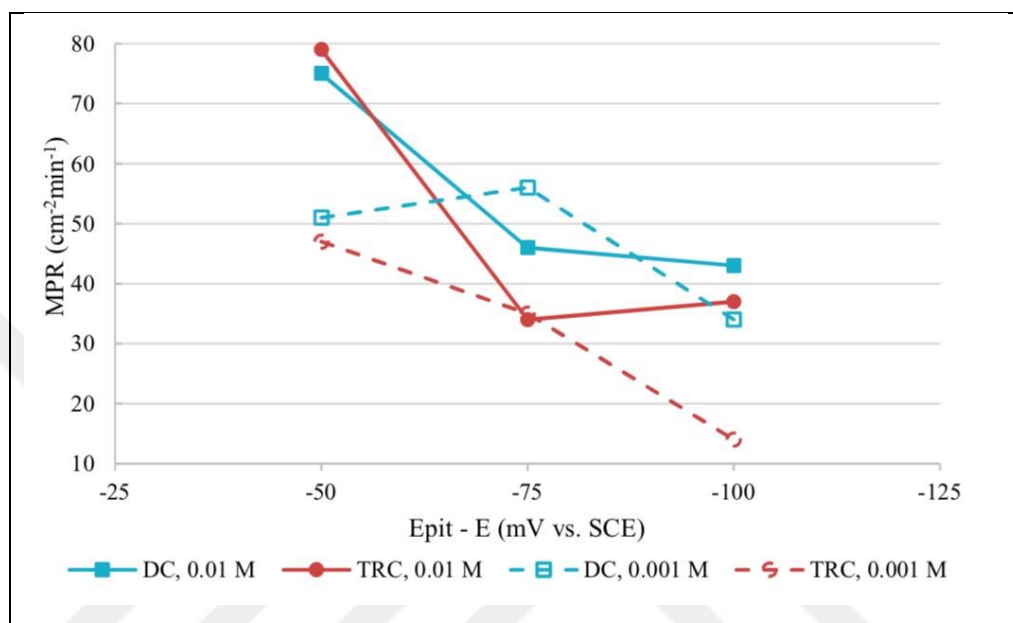


Figure 4.37. Metastable Pitting Rate (MPR) versus potential graph

From Figure 4.37, it is seen that metastable pitting events generally had higher intensity at 50 mV below E<sub>pit</sub>. The rate of metastable pitting is known to get lower as the potential is decreased [64]. For both concentrations, at the underpotential of 50 mV, there was not much more difference in the metastable pitting rates of the DCC alloy and the TRC alloy. However, at other underpotentials, the DCC alloy had a higher rate of metastable pitting for both 0.01 M and 0.001 M. Thus, since the DCC alloy have higher metastable pitting rate than its TRC counterpart, the TRC alloy may exhibit higher resistance to the pitting corrosion in 0.01 M and 0.001 M NaCl.

Another comparison was made between the alloys with respect to the total charges of the metastable pitting events. During the measurement, charge data was collected by software cumulatively. The charge of a metastable pitting event was found as the difference between the cumulative charge at the pit termination and that at the pit initiation (Figure 4.36). Then, the charge of all events in a current versus time data was determined and summed. Since

experiments were conducted three times under the same conditions, an average total charge was calculated. Results are shown in Figure 4.38.

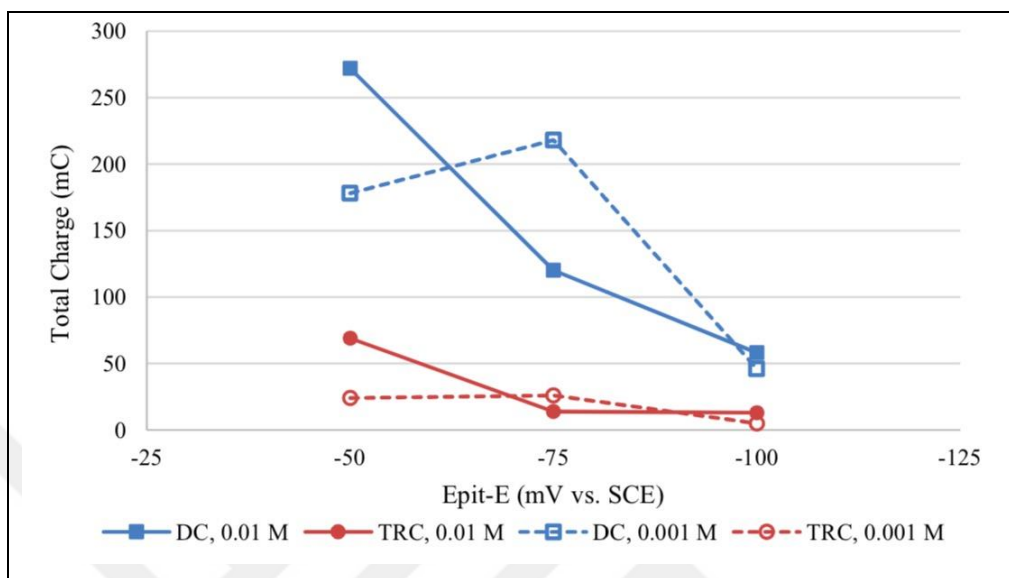


Figure 4.38. Total charge versus potential graph

It is seen from Figure 4.38 that under all conditions, the DCC samples had a higher total charge of metastable pitting. Since the rate of metastable pitting was higher for the DCC alloy, a higher total charge could be expected for the DCC alloy. Gupta reported that AA2024 alloy had a higher total charge of metastable pitting events compared to AA7075 [64]. Larger and deeper stable pits were seen in the AA2024. Besides, the metastable pitting rate was larger in the AA7075 and more stable pits formed on it.

#### 4.8. ELECTROCHEMICAL NOISE (EN) MEASUREMENTS OF GALVANIC COUPLE

EN analysis is one of the tests that can be chosen to measure the localized corrosion activity of a material. The main advantage of this analysis is that it can be performed without disturbing the metal being tested. When a passive metal or alloy is exposed to a corrosive environment, an electrochemical noise is generated due to local corrosion occurring on the surface of it. By analysing this noise, information can be obtained about the localized corrosion of the material tested.

In this thesis, electrochemical noise analysis was performed by galvanically interacting two sample coupons from the material to be tested in the test solution (0.1 M and 0.01 M NaCl solutions). The current between the two samples (electrochemical current noise, ECN) and the potential of these two samples (electrochemical potential noise, EPN) with respect to the RE were measured. This study consists of two types. In the first type, EN measurement was done after 10 minutes of immersion of the galvanically coupled electrodes in the test solution. EN data was collected for 3 hours. In the second type of measurement, EN measurement was done after 24 hours of waiting at OCP in the test solution. In this type, EN data was collected for 30 minutes. For both types, two repetitive experiments were done. Figure 4.39 and Figure 4.40 shows potential versus time graphs (electrochemical potential noise) of (a) DCC and (c) TRC alloys and current versus time graphs (electrochemical current noise) of (b) DCC and (d) TRC alloys collected after 10 minutes of immersion in 0.1 M NaCl and 0.01 M NaCl test solutions respectively. Note that the potential noise and current noise was collected simultaneous during a measurement. Thus, for instance, data in Figure 4.39 (a) and (b) belong to the same experiments. Since the experiments were repeated twice, two different colours were used to differentiate the results. For instance, the red line in Figure 4.39 (a) shows the EPN for an experiment. The corresponding ECN plot is given in Figure 4.39 (b). The blue lines in Figure 4.39 (a) and (b) are from the second experiment conducted under the same conditions. If Figure 4.39 (a) is considered, it is seen that the potential of DCC alloy first increased rapidly, then remained constant for a while, then dropped approximate to a potential between -0.85 V and -0.9 V. Furthermore, potential noise (oscillations in potential) were observed during about the first 6000 seconds of the measurements. On the other hand, the current noises of the corresponding measurement were more prominent as can be seen from Figure 4.39(b). The amplitudes of current oscillations were higher during the first 6000 seconds then decreased. The galvanic currents were between about 0 and 100 nA towards the end of the experiments. Potential data for the TRC alloy collected after 10 minutes of immersion (Figure 4.39(c)) increased from -0.9 V to -0.76 V during the first 4000 seconds. Afterwards, some decrease was observed. Current data of corresponding measurement (Figure 4.39(d)) shows that the current noise level remained almost constant. Overall Figure 4.39 shows that the TRC alloys exhibited less noise (noise with smaller amplitude). Similar observations could also be seen for the EN results collected after 10 minutes of immersion in 0.01 M NaCl solution (Figure 4.40). The DCC alloy samples had higher current noise amplitudes than TRC samples(Figure 4.40 (b))



and (d)). For instance, current noise amplitudes of the DCC alloy were as high as 100 nA in size whilst those of the TRC alloy were much lower.

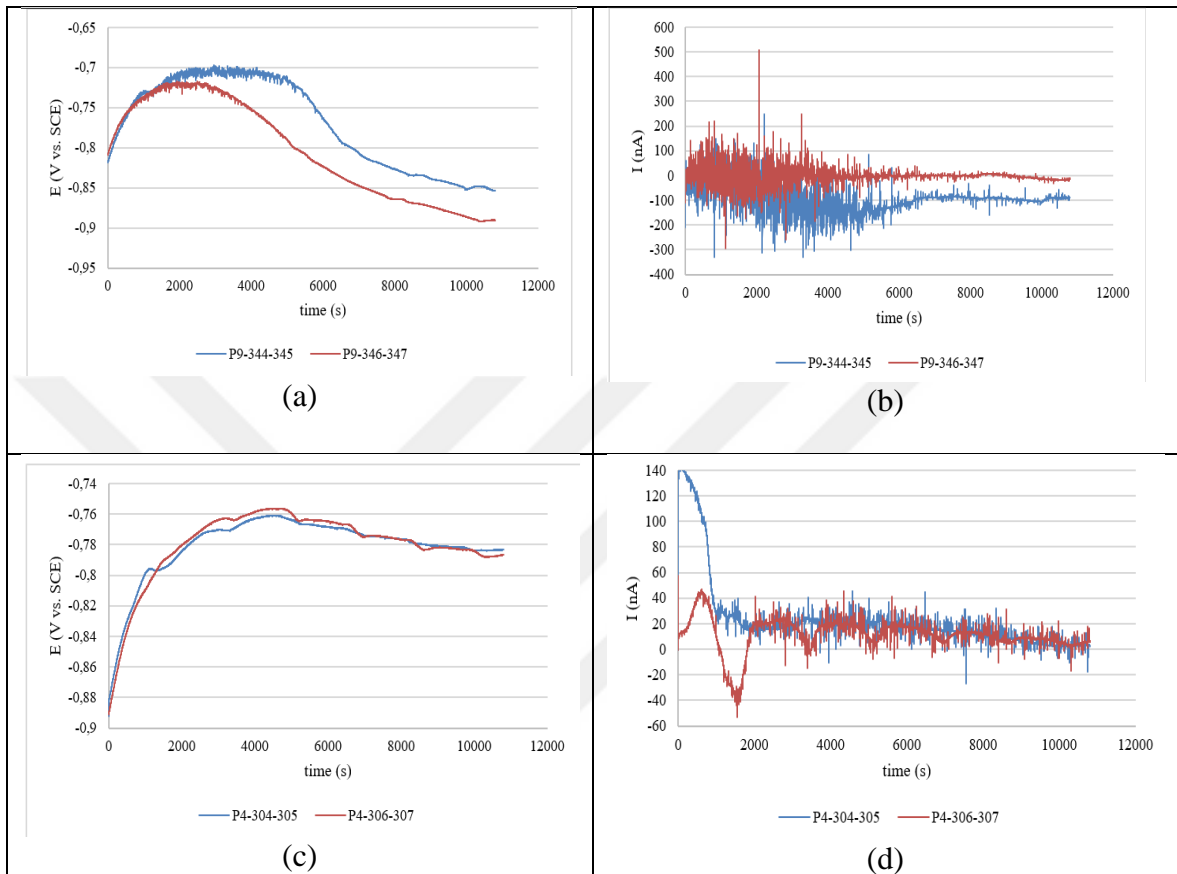
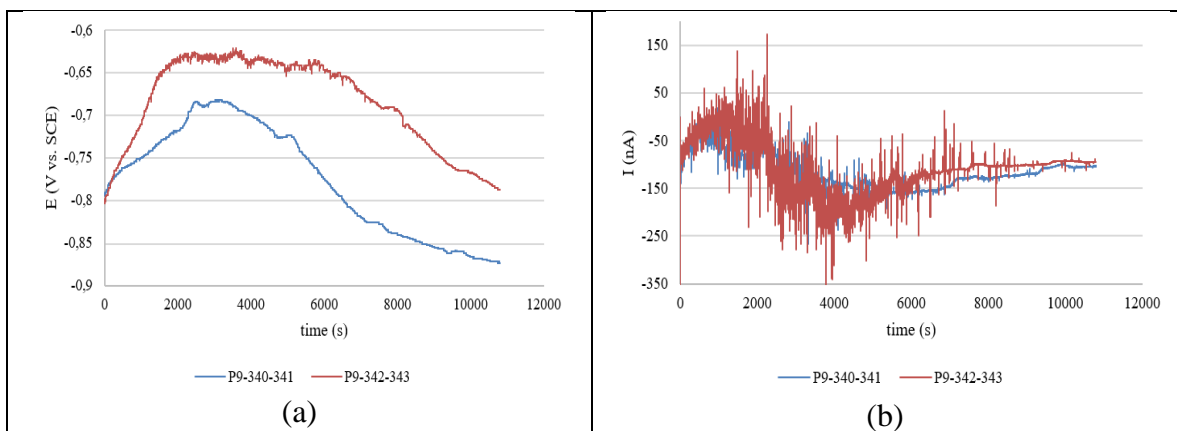


Figure 4.39. (a) EPN and (b) ECN results for DCC alloy and (c) EPN and (d) ECN results for TRC alloy collected after 10 minutes of immersion in 0.1 M NaCl solution



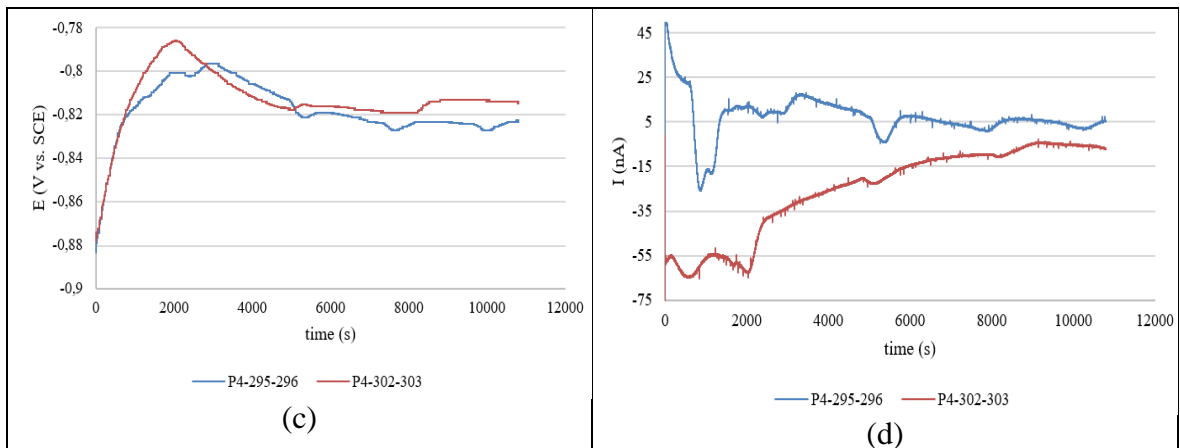
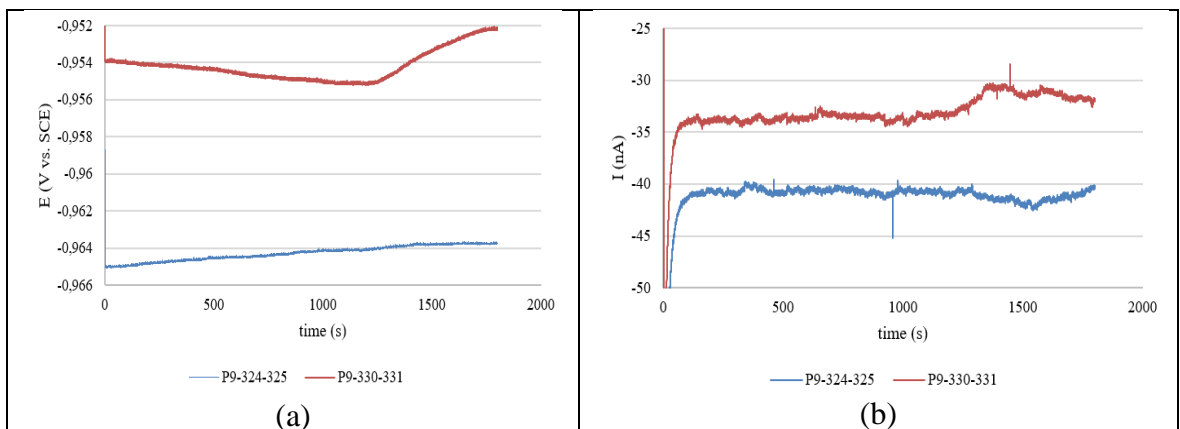


Figure 4.40. (a) EPN and (b) ECN results for DCC alloy and (c) EPN and (d) ECN results for TRC alloy collected after 10 minutes of immersion in 0.01 M NaCl solution

Figure 4.41 and Figure 4.42 shows potential versus time graphs (electrochemical potential noise) of (a) DCC and (c) TRC alloys and current versus time graphs (electrochemical current noise) of (b) DCC and (d) TRC alloys collected after 24 hours of waiting at OCP in 0.1 M NaCl and 0.01 M NaCl test solutions, respectively. In this type, the electrodes were immersed into the solution and waited for a day. Therefore, the cathodic and anodic reactions occurring on the electrodes surfaces reached steady state. In both concentrations, the DCC alloy had more negative potentials compared to the TRC alloy, probably, due to its higher magnesium content (Figure 4.41(a) and (c); Figure 4.42(a) and (c)). Both the potential and the current noise levels were low compared to the results compared after 10 minutes of immersion. Some metastable pitting events were seen in both alloys.



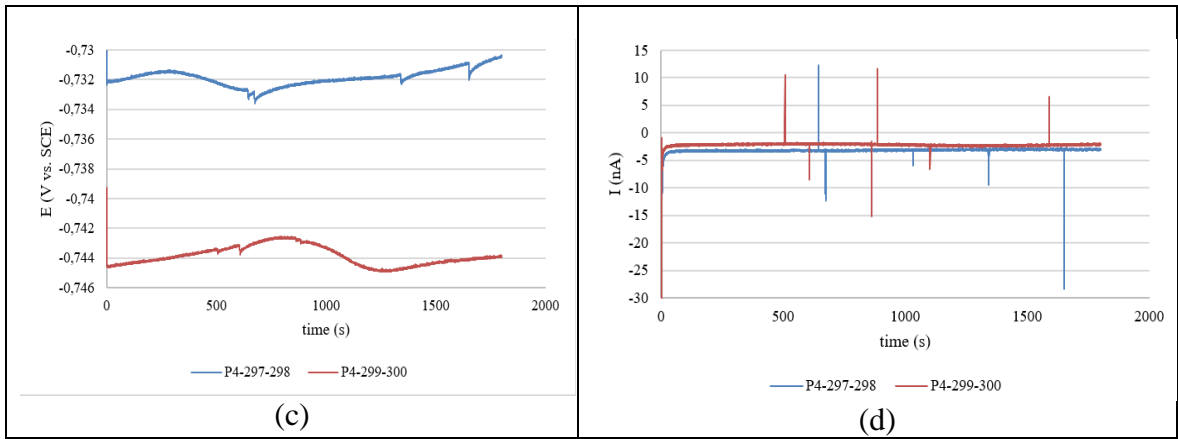


Figure 4.41. (a) EPN and (b) ECN results for DCC alloy and (c) EPN and (d) ECN results for TRC alloy collected after 24 hours of waiting at open circuit potential 0.1 M NaCl solution

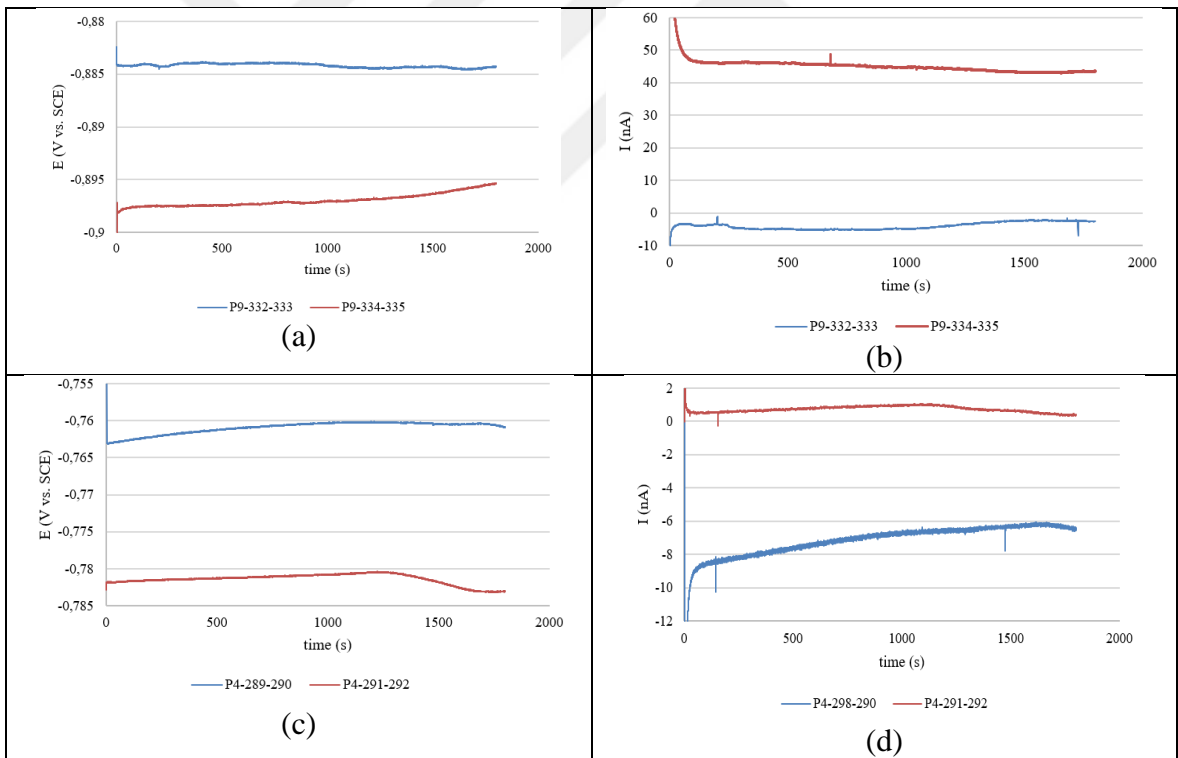


Figure 4.42. Figure 4.43. (a) EPN and (b) ECN results for DCC alloy and (c) EPN and (d) ECN results for TRC alloy collected after 24 hours of waiting at open circuit potential 0.01 M NaCl solution

In addition to examining the current and potential time series data, there are different techniques for analysing electrochemical noise. In this thesis, pitting index (PI; also known as localization index; LI) and spectral power density (PSD) techniques were used. Pitting index is statistical quantity. It is calculated by dividing the standard deviation of the current noise to the square root average of the current. The pitting index has a value between 0 and 1. If the PI is smaller than 0.05; it indicates uniform corrosion, if PI is between 0.05 and 0.1; it defines mixed corrosion (uniform and localized) and values of PI higher than 0.1 indicates localized corrosion [96]. PI was calculated for all experiments. In the cone of measurements done 10 minutes after immersion, three parts of 1000 seconds were examined separately. These parts were chosen as (1) between 1000 and 2000 seconds, (2) between 5000 and 6000 seconds and (3) between 9800 and 10800 seconds. As it can be understood from the definition of PI, the PI is a strong function of the mean current. Therefore, when making comparisons, the mean current of both current time series should be comparable. For instance, for 0.1 M NaCl solution, PI of the DCC sample (shown as a red line in Figure 4.39 (b)) between 5000 and 6000 seconds was calculated as 0.91 which indicates a pitting corrosion. PI of the TRC sample (shown as a red line in Figure 4.39 (d)) between 5000 and 6000 seconds was found as 0.35 which indicates a mixed corrosion. They have similar mean currents of approximately 20 – 30 nA. Another comparison could be done between the DCC sample (shown as a red line in Figure 4.40 (b)) and the TRC sample (shown in red line in Figure 4.40 (d)) with a time interval 1000 and 2000 seconds in 0.01 M NaCl solution. Pitting indexes were found as 0.56 and 0.04 respectively. The DCC alloy shows a pitting corrosion behaviour while the TRC alloy shows a uniform corrosion with metastable pitting activity. Therefore, it can be understood from the PI results, the DCC samples have higher PI indexes than TRC ones.

Second analysis was power spectral density (PSD) plots. There are different transformation techniques in literature but the fast Fourier transform (FFT) is the common one for EN studies [97,98]. PSD plots were performed using European operative Group on Corrosion Monitoring of Nuclear Materials (ECG-Comon) PSD calculation program [99]. This program uses a Hanning windowing and does a linear trend removal. Trend removal is important to eliminate the contribution of the drift. If the trend is not removed, incorrect and new frequency components may occur [97]. Moreover, to do a transformation from time domain to frequency domain using this program; the data to be transformed should be a

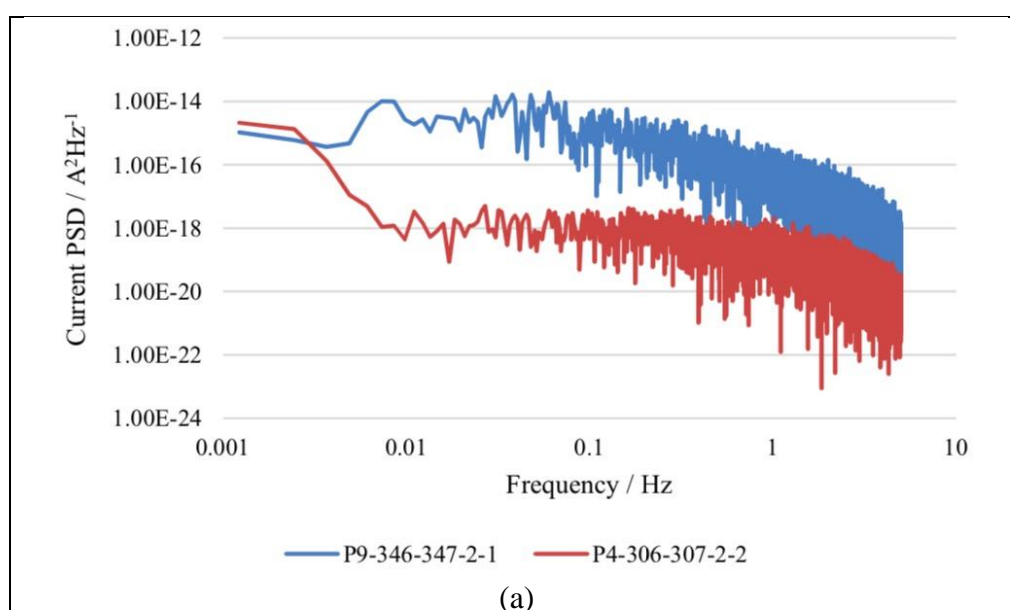
power of 2. Complete information about the program could be found in journal written by Ritter et al [100]. Comparing the potential noise and the current noise data, it is seen that amplitudes of current noise collected after 10 minutes of immersion were more pronounced. Therefore, only current data collected after 10 minutes of immersion (shown in Figure 4.39 (b), (d) and Figure 4.40 (b), (d)) were considered. As already mentioned, the data collected after 10 minutes of immersion were divided into three parts: data between (a) 1000 – 2000 seconds, (b) 5000 – 6000 seconds and (c) 9800 – 10800 seconds. However, in order to make better comparison, the regions with the high intensity of the current noise were chosen for both alloys. High electrochemical current noise intensities were observed between 1000 – 2000 seconds for the DCC alloy and 5000-6000 seconds for the TRC alloy. After all transformations were done, current PSD versus frequency graphs were plotted as shown in Figure 4.43 in (a) 0.1 M NaCl solution and in (b) for 0.01 M NaCl solution. In this figure, the blue lines indicate the PSDs for the DCC alloy whereas the red lines indicate PSDs for the TRC alloy.

If the PSD graphs were analysing, it is seen that the energy spectrum of the DCC alloy sheets were higher than that of the TRC alloy sheets in both concentrations. In other words, the DCC alloy have higher noise activity than the TRC alloy. Current spectrum density of the DCC alloy started from  $10^{-15} \text{ A}^2/\text{Hz}$ . The density remained nearly constant up to about a frequency of 0.1 Hz in both concentrations. However, this was not seen for the TRC alloy. It did not have a plateau in the low frequency region.

Some characteristics of the PSD plots supply information about corrosion activities. Homborg et al. stated that a PSD graph can have two regions [97]; a low frequency plateau and the high frequency region with a roll of slope. Low frequency part is defined as a horizontal section of PSD which shows PSD has almost no variation with frequency. On the other hand, in the higher frequency part, PSD decreases exponentially. The slope of the high frequency part is called as roll-off slope. When the PSD versus frequency data are plotted on a log-log scale, straight roll-off slope occurs. The frequency that separates these two parts is called as cut-off or roll-off frequency [101,102].

If the Figure 4.43 was examined, it is seen that roll of slopes could be measured only for the DCC alloy samples (blue lines for both graphs) because of the low frequency part could not be observed for the TRC alloy samples. Note that before calculating the slopes, first cut-off frequencies were determined. Cut-off frequency for DCC alloy in both concentrations was

chosen as 0.1 Hz. Then, low frequency part was omitted and  $\log(\text{PSD})$  versus  $\log(\text{frequency}; f)$  graphs were plotted [103]. Slope of the current PSD graph for the DCC alloy in 0.1 M NaCl solution was calculated as -2.30 where the slope of the current PSD graph for the DCC alloy in 0.01 M NaCl solution was found as -2.41. It is seen that slopes have negative signs. This is due to the energy signal of the corrosion processes decreases with increasing frequency. On the other hand, roll of slopes decreased with decreasing the chloride ion concentration. Some researches represent that the level of low frequency part give an information about the corrosion type [104] and some others support that the magnitude of the roll-off slope (slope of high frequency part) helps to understand the corrosion processes in the electrochemical system [97,105,106]. However, conflicting results from roll-of slopes have been also reported [97,98,107]. Cottis et al. [107] compared the noise measurements of pure aluminum in borate buffer solution (pH = 6.4) and 0.1 M NaCl solution. It is reported that the aluminum is in the passive state in the buffer solution; while it exhibits a pitting corrosion at a NaCl concentration of 0.1 M. When the current PSD graphs in these two different cases were compared, the roll-off slope was found to be steeper for the pit corrosion condition. The roll-off slope for the passive case is horizontal. Referring to Figure 4.43, a steeper slope was seen for the DCC alloy at frequencies greater than 0.1 Hz. As a result, higher corrosion activity in the DCC alloy for comparative time intervals led to steeper roll-off slopes in current PSDs.



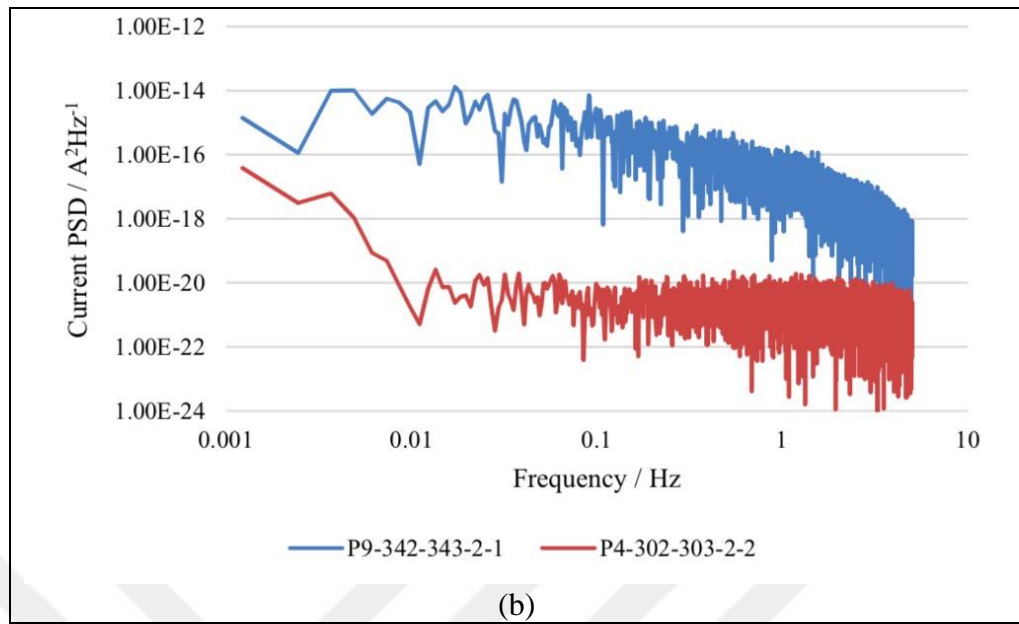


Figure 4.44. Current PSD versus frequency graphs for DCC and TRC alloys in (a) 0.1 M NaCl solution and (b) 0.01 M NaCl solution

## 5. CONCLUSION

In this study, the resistance to pitting corrosion of AA5005 sheets produced by direct chill casting (DCC) was compared with that of AA5005 sheets produced by the twin-roll casting (TRC). The conclusions of the study are as follows:

- According to microstructure investigations, it is seen that larger intermetallic particles are seen in the DCC alloy. On the other hand, the TRC alloy has a larger number of intermetallics. Intermetallics in both alloys contained Al, Fe, Si and, to a lesser amount, Mg.
- Surfaces of the both alloys were investigated using optical profilometry and SEM after a week of immersion in 0.01 M NaCl solution. Both optical profilometry and SEM investigations showed that pits of larger diameter were found in the DCC alloy compared to the TRC alloy.
- Depending on the OCP results, open circuit potentials increased rapidly after the immersion for both DCC and TRC alloys. Nearly steady open circuit potential ( $E_{ocp}$ ) values were obtained for all types of alloys after about 6000 seconds of immersion for all concentrations. After 3 hours, the approximate difference between two alloys were 100 mV vs SCE. The AA5005 alloy produced by TRC technique presented more positive potentials, most probably because of its lower Mg content.
- Depending on the CPP results, two critical potentials were obtained; the pitting potentials ( $E_{pit}$ ) and the repassivation potentials ( $E_{repass}$ ).  $E_{pit}$  of two types of AA5005 alloys are found to be close to each other for all NaCl concentrations. Generally, AA5005 DCC alloys have more positive  $E_{pit}$  values than TRC ones. The highest difference between the alloys was found as 16 mV at 0.1 M NaCl solution. Moreover, with decreasing chloride ion concentration  $E_{pit}$  values became more positive for both types of alloys.  $E_{repass}$  generally decreased with decreasing chloride ion concentration for both AA5005 alloys.
- $E_{repass}$  determination was detected within a range of 25 mV under potentiostatic conditions. If the middles of the ranges are taken as  $E_{repass}$  potentials, the TRC alloy has  $E_{repass}$  values that are 25 mV lower than those of the DCC alloy at 1 M and 0.1 M NaCl



solutions. There is no difference between the  $E_{\text{repass}}$  values of the alloys of the two production techniques at 0.01 M.

- From the galvanostatic cyclic polarization (GSCP) measurements, the breakdown potential,  $E_{\text{bd}}$ , and the protection potential,  $E_{\text{prot}}$ , were found for the alloys.  $E_{\text{bd}}$  values for both AA5005 alloys were found to be very close to each other. Likewise,  $E_{\text{prot}}$  values for both alloys were very close to each other. For both  $E_{\text{bd}}$  and  $E_{\text{prot}}$ , the highest differences between two alloys were found at 0.01 M as 8 mV. Results show that DCC alloys have only slightly more positive  $E_{\text{bd}}$  than TRC ones for all concentrations tested. For both alloys (DCC and TRC) both  $E_{\text{bd}}$  and  $E_{\text{prot}}$  potentials decreased with decreasing chloride ion concentration.
- Metastable pitting corrosion measurements were done under three potentiostatic conditions; 50, 75 and 100 mV below the  $E_{\text{pit}}$  of each AA5005 alloy type (DCC or TRC). Metastable pitting activities were higher during the first 500 seconds of the measurements for both AA5005 alloy types. The highest metastable pitting activities were seen at 50 mV below  $E_{\text{pit}}$  for both alloys. Generally, the DCC alloy had a higher rate of more metastable pitting at all concentrations. The total charge of metastable pitting was also higher for the DCC alloy.
- Electrochemical noise (EN) measurements were performed by galvanically interacting two samples from the material to be tested (either two AA5005 DCC samples or two AA5005 TRC samples) with two different test procedures. Depending on the noise data collected after 10 minutes of immersion, it was seen that, the DCC alloy have higher corrosion activity than the TRC alloy for both concentrations. This is probably due to the higher magnesium content and the presence of larger intermetallic particles in the DCC alloy. Moreover, this high corrosion activity decreased with time. On the other hand, for the measurements done after 24 h of immersion, for both the DCC and the TRC alloys, data was much less noisy with metastable pitting activities. PSD plots were plotted using fast Fourier transform (FFT) technique. Steeper slopes were seen for the DCC alloy at frequencies greater than 0.1 Hz. As a result, higher corrosion activity in the DCC alloy led to steeper roll-off slopes in current PSDs.
- Based on the  $E_{\text{pit}}$  values found from CPP experiments and  $E_{\text{repass}}$  values determined potentiostatically, the two alloys showed similar resistances to the pitting corrosion.

## REFERENCES

1. Koch GH, Brongers MPH, Thompson NG, Virmani YP, Payer JH. *Corrosion costs and preventive strategies in the United States*. Texas: Nace International; 2001.
2. Mazhar AA, Arab ST, Noor EA. The role of chloride ions and pH in the corrosion and pitting of Al-Si alloys. *Journal of Applied Electrochemistry*. 2001;31(10):1131–40.
3. Dillon CP. *Forms of corrosion: recognition and prevention*. Texas: Nace International; 1982.
4. Prentice GA. *Electrochemical engineering principles*. New Jersey: Prentice Hall; 1990.
5. Winston Revie R, Uhlig HH. *Corrosion and corrosion control, an introduction to corrosion science and engineering*. New Jersey: John Wiley and Sons; 2008.
6. McCafferty E. *Introduction to corrosion science*. Virginia: Springer; 2010.
7. Foroulis ZA, Uhlig HH. Effect of impurities in iron on corrosion in acids. *Journal of The Electrochemical Society*. 1965;112(12):1177-9.
8. Revie RW. *Uhlig's corrosion handbook*. New Jersey: Wiley and Sons; 2011.
9. Beck TR. Initial oxide growth rate on newly generated surfaces. *Journal of the Electrochemical Society*. 1982;129(11):2500–1.
10. Roberge PR. *Corrosion engineering: principles and practice*. New Jersey: McGraw-Hill; 2008.
11. Heusler KE, Fischer L. Kinetics of pit initiation at passive iron. *Materials and Corrosion*. 1976;27(8):551–6.
12. Szklarska-Smialowska Z. Pitting corrosion of aluminum. *Corrosion Science*. 1999;41(9):1743–67.
13. Sedriks AJ. *Corrosion of stainless steels*. New York: Wiley and Sons; 1996.

14. Davis GD, Moshier WC, Long GG, Black DR. Passive film structure of supersaturated Al-Mo alloys. *Journal of The Electrochemical Society*. 1991;138:3194-7.
15. Frankel GS, Newman RC, Jahnes C V., Russak MA. On the pitting resistance of sputter-deposited aluminum alloys. *Journal of The Electrochemical Society*. 1993;140:2192-5.
16. Chao CY, Lin LF, MacDonald DD. A point defect model for anodic passive films. *Journal of The Electrochemical Society*. 1981;128:1187-8.
17. Krishnakumar R, Szklarska-Smialowska Z, MacDougall BR, Awitt RS, Ramanarayanan TA. Passivation characteristics of sputtered metastable Al-Cr and Al-Ta alloy films - an impedance study. *Proceedings Symposium Oxide Films on Metals and Alloys*. 1992: The Electrochemical Society.
18. Wang JB, Wang JM, Shao HB, Cao CN, Zhang JQ. The corrosion and electrochemical behaviour of pure aluminium in alkaline methanol solutions. *Journal of Applied Electrochemistry*. 2007;37:753-8.
19. Doche ML, Rameau JJ, Durand R, Novel-Cattin F. Electrochemical behaviour of aluminium in concentrated NaOH solutions. *Corrosion Science*. 1999;41:805-26.
20. Vijh AK. The corrosion potentials of some common metals in oxygenated solutions in relation to semi-conductivity of the corrosion films. *Corrosion Science*. 1972;12:105-7.
21. Kobotiatis L, Kioupis N, Koutsoukos PG. Electronic properties of passive films grown on Al 7075 in solutions containing oxalate and chromate. *Corrosion*. 1997;53:562-4.
22. Szklarska-Smialowska Z. Insight into the pitting corrosion behavior of aluminum alloys. *Corrosion Science*. 1992;33:1193-4.
23. Natishan PM, Mccafferty E, Hubler GK. The effect of pH of zero charge on the pitting potential. *Journal of the Electrochemical Society*. 1986;1061-2.
24. Intermetallic compound. 1998 [cited 2019 29 July]. Available from:

<https://www.britannica.com/science/metal-chemistry>

25. Birbilis N, Cavanaugh MK, Buchheit RG, Harlow DG, Wei RP. *Applications of materials science to military systems*. Pennsylvania: The Mineal, Metals and Materials Society; 2005.
26. Davis JR. *Corrosion of aluminium and aluminium alloys*. Ohio: ASM International; 1999.
27. Birbilis N, Buchheit RG. Electrochemical characteristics of intermetallic phases in aluminum alloys an experimental survey and discussion. *The Electrochemical Society*. 2005;152:140–51.
28. Nişancıoğlu K. Electrochemical behavior of aluminum-base intermetallics containing iron. *Journal of the Electrochemical Society*. 1990;137:69-74.
29. Zamin M. The role of Mn in the corrosion behavior of Al-Mn alloys. *Corrosion*. 1981;37:627–32.
30. Ren W Da, Li JF, Zheng ZQ, Chen WJ. Localized corrosion mechanism associated with precipitates containing Mg in Al alloys. *Transactions of Nonferrous Metals Society of China (English Edition)*. 2007;17(4):727–32.
31. Ezuber H, El-Houd A, El-Shawesh F. A study on the corrosion behavior of aluminum alloys in seawater. *Materials and Design*. 2008;29(4):801–5.
32. Abelle A, Bethencourt M, Botana F, Cano M, Marcos M. Localized alkaline corrosion of alloy AA5083 in neutral 3.5% NaCl solution. *Corrosion Science*. 2001;43:1657–74.
33. Bethencourt M, Botana F, Calvino J, Marcos M, Perez J, Redriques M. Electrochemical impedance spectroscopy study of the behavior of lanthanide-rich films formed on aluminum–magnesium alloys. *Materials Science Forum*. 1998;289–292:567–74.
34. Abelle A, Bethencourt M, Botana F, Cano M, Marcos M. ENM study on the influence of surface polishing on Al–Mg alloy corrosion behavior. *Past Successes - Future Challenges EUROCORR 2000*. 2000: Universidad de Cadiz.

35. Abelle A, Bethencourt M, Botana F, Cano M, Marcos M. Influence of the cathodic intermetallics distribution on the reproducibility of the electrochemical measurements on AA5083 alloy in NaCl solutions. *Corrosion Science*. 2003;45:161–80.
36. Abelle A, Bethencourt M, Botana F, Marcos M. CeCl<sub>3</sub> and LaCl<sub>3</sub> binary solutions as environment-friendly corrosion inhibitors of AA5083 Al–Mg alloy in NaCl solutions. *Journal of Alloys and Compounds*. 2001;323–324:855–8.
37. Abelle A, Bethencourt M, Botana F, Marcos M, Sanchez-Amaya J. Influence of the degree of polishing of alloy AA5083 on its behavior against localized alkaline corrosion. *Corrosion Science*. 2004;46:1909–20.
38. Engler O, Marioara CD, Hentschel T, Brinkman HJ. Influence of copper additions on materials properties and corrosion behaviour of Al-Mg alloy sheet. *Journal of Alloys and Compounds*. 2017;710:650–62.
39. Ghali E. *Corrosion resistance of aluminum and magnesium alloys, understanding, performance and testing*. New York: John Wiley and Sons; 2010.
40. Zeng R, Zhang J, Huang W, Dietzel W, Kainer KU, Blawert C, Ke W. Review of studies on corrosion of magnesium alloys. *Transactions of Nonferrous Metals Society of China*. 2006;16:763–71.
41. Ghali E, Dietzel W, Kainer KU. General and localized corrosion of magnesium alloys: a critical review. *Journal of Materials Engineering and Performance*. 2004;13(1):7–23.
42. Oktay G, Ürgen M. Corrosion behaviour of magnesium AZ31 sheet produced by twin roll casting. *Corrosion Engineering, Science and Technology*. 2014;50(5):380–9.
43. Kurt K, Dursun A, Dilsizo B, Anger G, Ürgen M. Comparison of the corrosion behaviors of twin-roll Cast and DC cast AA6016 and AA6082 for automotive applications. *The Minerals, Metals and Materials Society*. 2006;79–87.
44. Birol F, Birol Y. Corrosion behavior of twin-roll cast al-mg and al-mg-si alloys. *Materials Forum*. 2004;28:338–44.
45. Soltis J, Laycock NJ, Krouse D. Temperature dependence of the pitting potential of

- high purity aluminium in chloride containing solutions. *Corrosion Science*. 2011;53(1):7–10.
46. Ernst P, Moayed MH, Laycock NJ, Newman RC. Prediction of pitting potentials and critical pitting temperatures using localized dissolution kinetics. *Passivity of Metals and Semiconductors*. 1999;665–74.
  47. Beljajew AI, Firsanowa LA, Rapaport MB. *Metallurgy of aluminium*. İstanbul: Turkish Chamber of Mechanical Engineering; 1998.
  48. Sanders RE. Continuous casting for aluminum sheet: a product perspective. *Journal of the Minerals*. 2012;64(2):291–301.
  49. Aluminum Association I. *Rolling aluminum: from the mine through the mill*. Virginia: The Aluminum Association; 2008.
  50. Büyükbaş F. Çift merdaneli sürekli levha döküm yöntemi ile üretilmiş AA3003 alaşımlı alüminyum levhalarda proses parametrelerinin özelliklere etkisi [dissertation]. İstanbul Technical University; 2001.
  51. Barekar NS, Dhindaw BK. Twin-roll casting of aluminum alloys – an overview. *Materials and Manufacturing Processes*. 2014;29(6):651–61.
  52. Zhao YM, Morris JG. Comparison of the texture evolution of direct chill and continuous cast AA5052 hot bands during isothermal annealing. *Metallurgical and Materials Transactions*. 2005;36A:2505–15.
  53. Slámová M, Karlík M, Robaut F, Sláma P, Véron M. Differences in microstructure and texture of Al–Mg sheets produced by twin-roll continuous casting and by direct-chill casting. *Materials Characterization*. 2003;49(3):231–40.
  54. Yu XF, Zhao YM, Wen XY, Zhai T. A study of mechanical isotropy of continuous cast and direct chill cast AA5182 Al alloys. *Materials Science and Engineering*. 2005;A394:376–84.
  55. Kim K. The effect of melt conditioning on segregation of solute elements and nucleation of aluminum grains in a twin roll cast aluminum alloy. *Metallurgical and Materials Transactions*. 2014;A45:4538–48.

56. Lockyer SA, Yun M, Hunt JD, Edmonds D V. Micro- and macrodefects in thin sheet twin-roll cast aluminum alloys. *Materials Characterization*. 1996;37:301–10.
57. Yun M, Lockyer SA, Hunt JD. Twin roll casting of aluminium alloys. *Materials Science and Engineering*. 2000;A280:116–23.
58. Das S, Lim NS, Seol JB, Kim HW, Park CG. Effect of the rolling speed on microstructural and mechanical properties of aluminum-magnesium alloys prepared by twin roll casting. *Materials and Design*. 2010;31(3):1633–8.
59. Keles O, Dundar M. Aluminum foil: its typical quality problems and their causes. *Journal of Materials Processing Technology*. 2007;186:125–37.
60. Karlík M, Slámová M, Janeček M, Homola P. Microstructure evolution of twin-roll cast Al-Mg alloys during downstream processing. *Kovove Materialy*. 2002;40:330–40.
61. ASTM G69-12 Standard test method for measurement of corrosion potentials of aluminum alloys. 2013 [cited 2019 10 July]. Available from: <https://www.astm.org/Standards/G69.htm>
62. Huang IW, Buchheit RG. Uniform corrosion dependence on temperature and pH of aluminum alloys 2024-T3. *ECS Transactions*. 2015;97–107.
63. Hirozawa ST. Galvanostaircase polarization. *Journal of the Electrochemical Society*. 1984;131(10):2452–4.
64. Gupta RK, Sukiman NL, Cavanaugh MK, Hinton BRW, Hutchinson CR, Birbilis N. Metastable pitting characteristics of aluminium alloys measured using current transients during potentiostatic polarisation. *Electrochimica Acta*. 2012;66:245–54.
65. Pride ST. Metastable pitting of aluminum and criteria for the transition to stable pit growth. *Journal of the Electrochemical Society*. 1994;141(11):3028-30.
66. Cavanaugh MK. Modeling the environmental dependence of localized corrosion evolution in AA7075-T651 [dissertation]. Ohio State University. 2009.
67. Ambat R, Davenport AJ, Scamans GM, Afseth A. Effect of iron-containing intermetallic particles on the corrosion behaviour of aluminium. *Corrosion Science*.

- 2006;48(11):3455–71.
68. Nişancioğlu K. Electrochemical behavior of aluminum-base intermetallics containing iron. *Journal of The Electrochemical Society*. 1990;137(1):69-73.
  69. Aziz PM, Godard HP. Pitting corrosion characteristics of aluminum. *National Association of Corrosion Engineers*. 1954;10:269–72.
  70. Brillas E, Cabot PL, Centellas F, Garrido JA, Pérez E, Rodríguez RM. Electrochemical oxidation of high-purity and homogeneous Al-Mg alloys with low Mg contents. *Electrochimica Acta*. 1998;43(7):799–812.
  71. Sukiman NL, Shi H, Gupta RK, Buchheit RG, Birbilis N. Electrochemical and corrosion response of commercially pure aluminum alloyed with binary additions of strontium. *Journal of the Electrochemical Society*. 2013;160(8):C299–304.
  72. Wang Y, Gupta RK, Sukiman NL, Zhang R, Davies CHJ, Birbilis N. Influence of alloyed Nd content on the corrosion of an Al-5Mg alloy. *Corrosion Science*. 2013;73:181–7.
  73. Gupta RK, Hinton BRW, Birbilis N. The effect of chromate on the pitting susceptibility of AA7075-T651 studied using potentiostatic transients. *Corrosion Science*. 2014;82:197–207.
  74. Zaid B, Saidi D, Benzaid A, Hadji S. Effects of pH and chloride concentration on pitting corrosion of AA6061 aluminum alloy. *Corrosion Science*. 2008;50(7):1841–7.
  75. Comotti IM, Trueba M, Trasatti SP. The pit transition potential in the repassivation of aluminium alloys. *Surface and Interface Analysis*. 2013;45(10):1575–84.
  76. Yasuda M. Pitting corrosion of Al and Al-Cu single crystals. *Journal of The Electrochemical Society*. 1990;137(12):3708-10.
  77. ASTM G61-86 Standard test method for conducting cyclic potentiodynamic polarization measurements to determine the corrosion susceptibility of iron-, nickel-, or cobalt-based alloys. 2001 [cited 2019 10 July]. Available from: <https://www.astm.org/Standards/G61.htm>



78. Amin MA. Pitting of Al and Al-Si alloys in KSCN solutions and the effect of light. *Arabian Journal of Chemistry*. 2013;6(1):87–92.
79. Cicolin D, Trueba M, Trasatti SP. Effect of chloride concentration, pH and dissolved oxygen, on the repassivation of 6082-T6 Al alloy. *Electrochimica Acta*. 2014;124:27–35.
80. Foley RT. Localized corrosion of aluminum alloys - a review. *Corrosion*. 1986;42(5):277–88.
81. Trueba M, Trasatti SP. Study of Al alloy corrosion in neutral NaCl by the pitting scan technique. *Materials Chemistry and Physics*. 2010;121(3):523–33.
82. Trueman AR. Determining the probability of stable pit initiation on aluminium alloys using potentiostatic electrochemical measurements. *Corrosion Science*. 2005;47(9):2240–56.
83. Takeyama T, Shibata T. Stochastic theory of pitting corrosion. *Corrosion*. 1977;33(7):243–51.
84. Nişancioğlu K, Holtan H. The protection potential of aluminium. *Corrosion Science*. 1978;18:1011–23.
85. Wang B, Liu J, Yin M, Xiao Y, Wang XH, He JX. Comparison of corrosion behavior of Al-Mn and Al-Mg alloys in chloride aqueous solution. *Materials and Corrosion*. 2015:1–9.
86. McCafferty E. The electrode kinetics of pit initiation on aluminum. *Corrosion Science*. 1995;37(3):481–92.
87. Kelly RG. *Corrosion tests and standards, application and interpretation*. Philadelphia: ASTM International; 1995.
88. Smialowska ZS. Pitting corrosion of aluminum. *Corrosion Science*. 1999;41(9):1743–67.
89. Pessall N, Liu C. Determination of critical pitting potentials of stainless steels in aqueous chloride environments. *Electrochimica Acta*. 1971;16:1987-9.

90. Evans KJ, Rebak RB. Measuring the repassivation potential of alloy 22 using the potentiodynamic-galvanostatic-potentiostatic method. *ASTM Special Technical Publication*. 2009;1506.
91. ASTM G100-89 Standard test method for conducting cyclic galvanostaircase polarization. 2010 [cited 2019 10 July]. Available from: <https://www.astm.org/Standards/G100.htm>
92. Bettini EL. *Progress in corrosion research*. New York: Nova Science Publishers; 2007.
93. Cavanaugh MK, Birbilis N, Buchheit RG. Modeling pit initiation rate as a function of environment for Aluminum alloy 7075-T651. *Electrochimica Acta*. 2012;59:336–45.
94. Williams DE, Stewart J, Balkwill PH. The nucleation, growth and stability of micropits in stainless steel. *Corrosion Science*. 1994;36(7):1213–35.
95. Williams DE. Stochastic models of pitting corrosion of stainless steels. *Journal of the Electrochemical Society*. 1985;132(8):1804-10.
96. Padilla-Viveros A, Garcia-Ochoa E, Alazard D. Comparative electrochemical noise study of the corrosion process of carbon steel by the sulfate-reducing bacterium *Desulfovibrio alaskensis* under nutritionally rich and oligotrophic culture conditions. *Electrochimica Acta*. 2006;51(18):3841–7.
97. Homborg AM, Tinga T, Van Westing EPM, Zhang X, Ferrari GM, De Wit JHW, Mol JMC. A critical appraisal of the interpretation of electrochemical noise for corrosion studies. *Corrosion*. 2014;70(10):971–87.
98. R.A. Cottis. Interpretation of electrochemical noise data. *Corrosion*. 2001;57(3):265–85.
99. Huet F. PSD Calculator. European Cooperative Group on Corrosion Monitoring of Nuclear Materials (ECG-COMON). [cited 2019 21 January]. Available from: <http://www.ecg-comon.org>
100. Ritter S, Huet F, Cottis RA. Guideline for an assessment of electrochemical noise

- measurement devices. *Materials and Corrosion*. 2012;63(4):297–302.
101. Lafront AM, Safizadeha F, Ghali E, Houlachi G. Study of the copper anode passivation by electrochemical noise analysis using spectral and wavelet transforms. *Electrochemistry Communications*. 2010;55(7):2505–12.
  102. Aballe A, Bethencourt M, Botana FJ, Marcos M. Wavelet transform-based analysis for electrochemical noise. *Electrochemistry Communications*. 1999;1(7):266–70.
  103. Lee CC, Mansfeld F. Analysis of electrochemical noise data for a passive system in the frequency domain. *Corrosion Science*. 1998;40(6):959–62.
  104. Kim JJ. Wavelet analysis of potentiostatic electrochemical noise. *Materials Letters*. 2007;61(18):4000–2.
  105. Du G, Li J, Wang WK, Jiang C, Song SZ. Detection and characterization of stress-corrosion cracking on 304 stainless steel by electrochemical noise and acoustic emission techniques. *Corrosion Science*. 2011;53(9):2918–26.
  106. Aballe A, Bethencourt M, Botana FJ, Marcos M. Using wavelets transform in the analysis of electrochemical noise data. *Electrochimica Acta*. 1999;44(26):4805–16.
  107. Cottis RA, Homborg AM, Mol JMC. The relationship between spectral and wavelet techniques for noise analysis. *Electrochimica Acta*. 2016;202:277–87.

## APPENDIX A: GRAPHICS FOR CYCLIC POTENTIAL POLARIZATION (CPP) MEASUREMENT

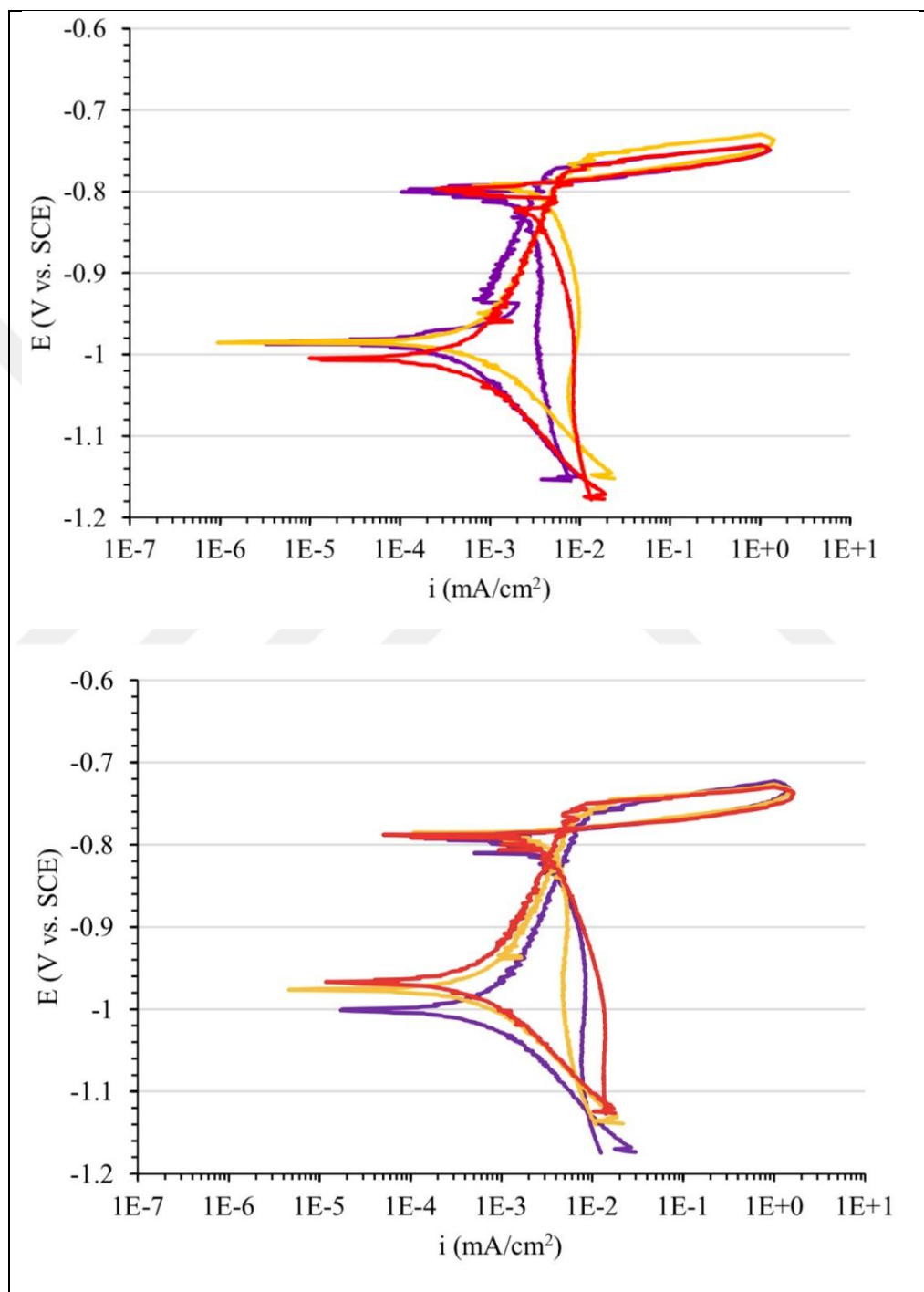


Figure A.1. CPP curves of DCC alloy sheets in 1 M NaCl solution

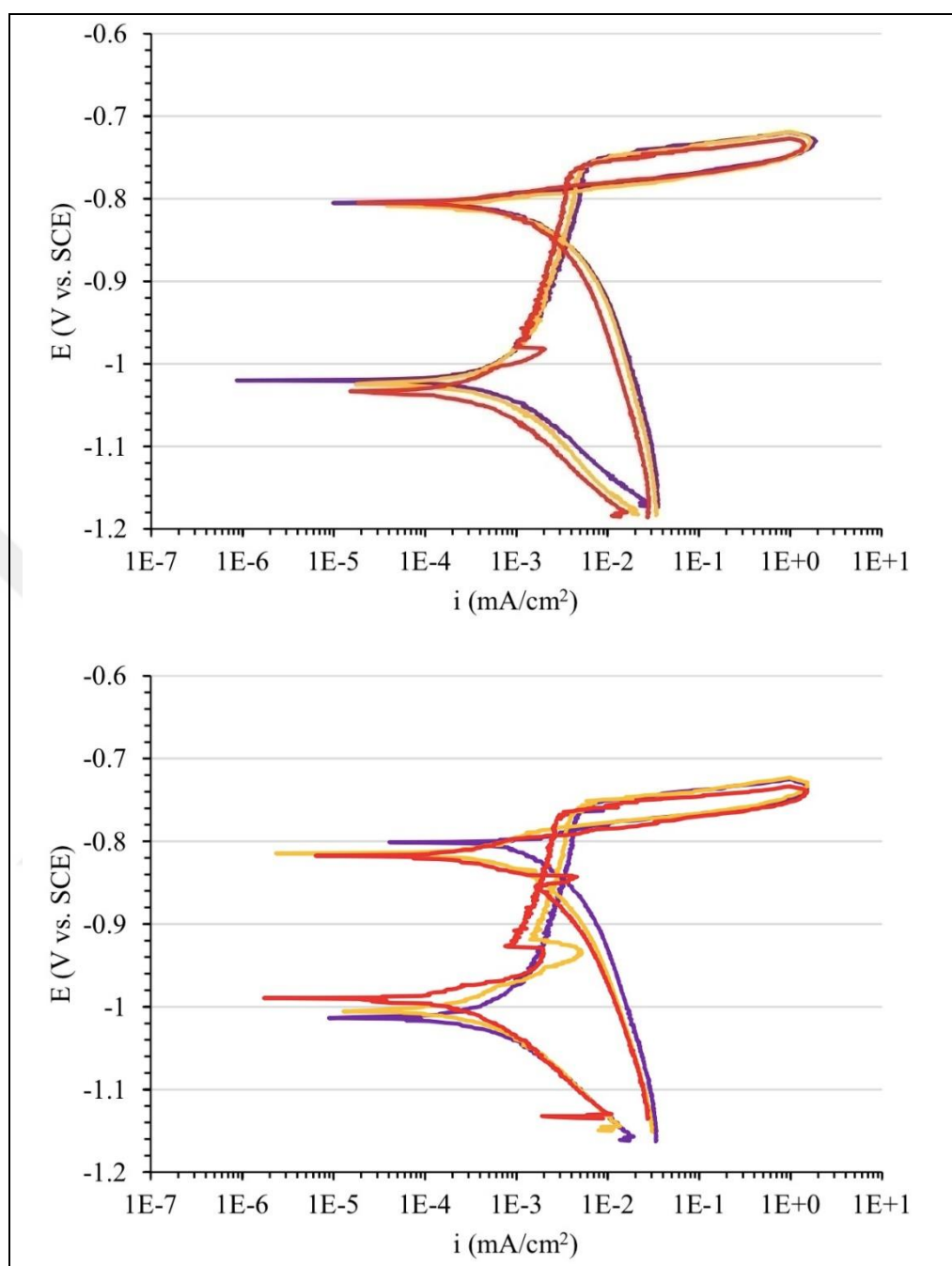


Figure A.2. CPP curves of TRC alloy sheets in 1 M NaCl solution

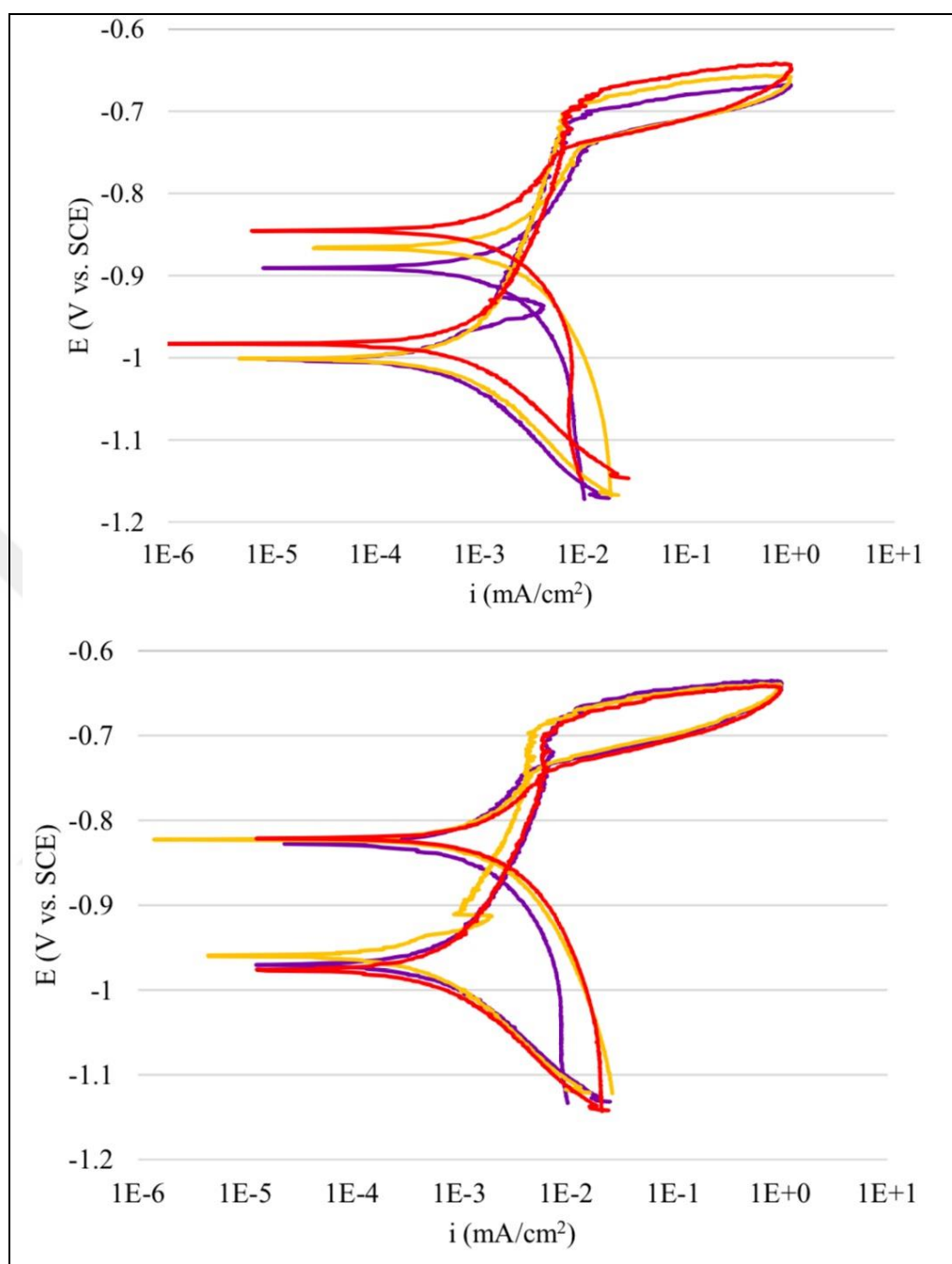


Figure A.3. CPP curves of DCC alloy sheets in 0.1 M NaCl solution

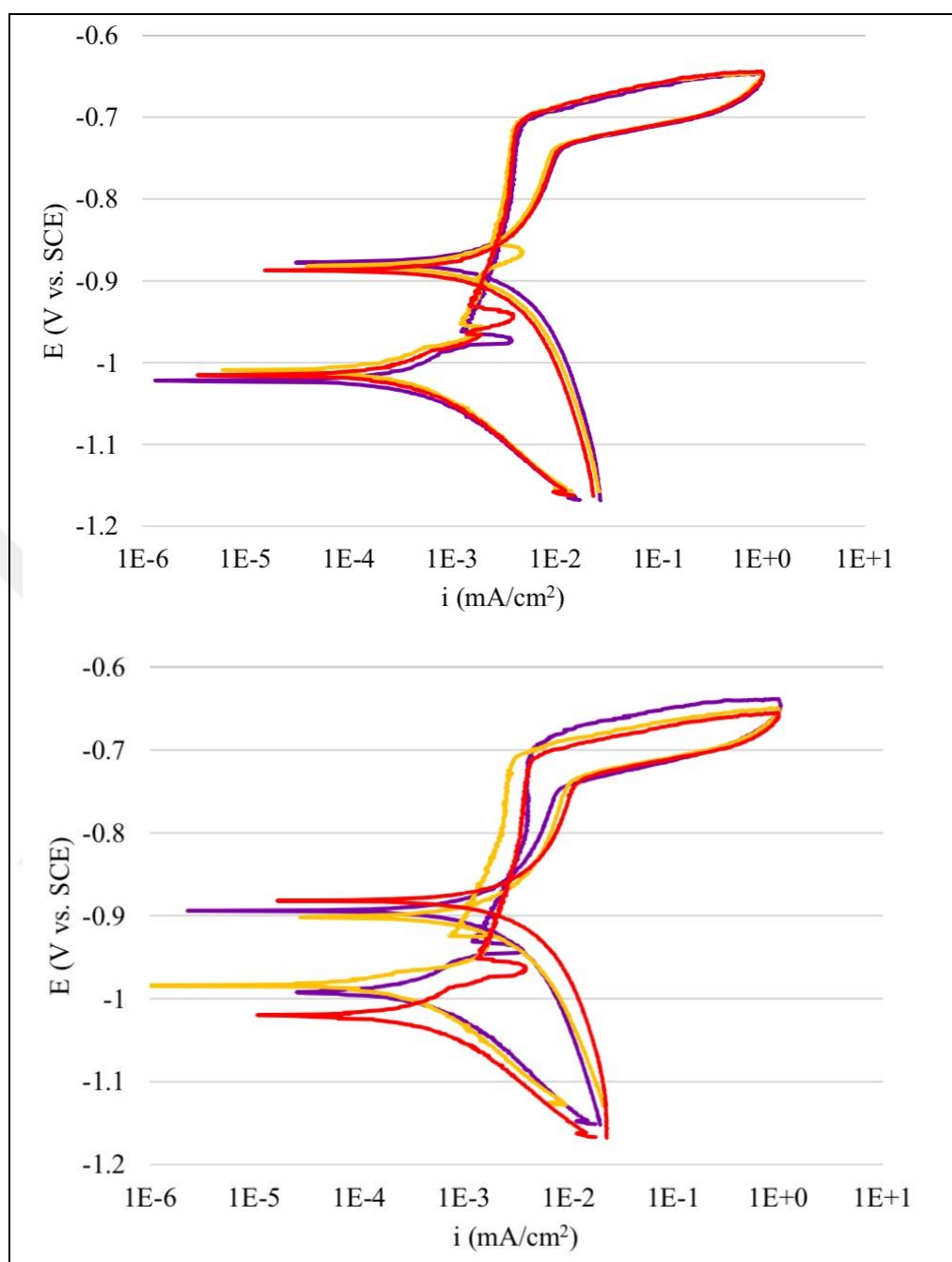


Figure A.4. CPP curves of TRC alloy sheets in 0.1 M NaCl solution

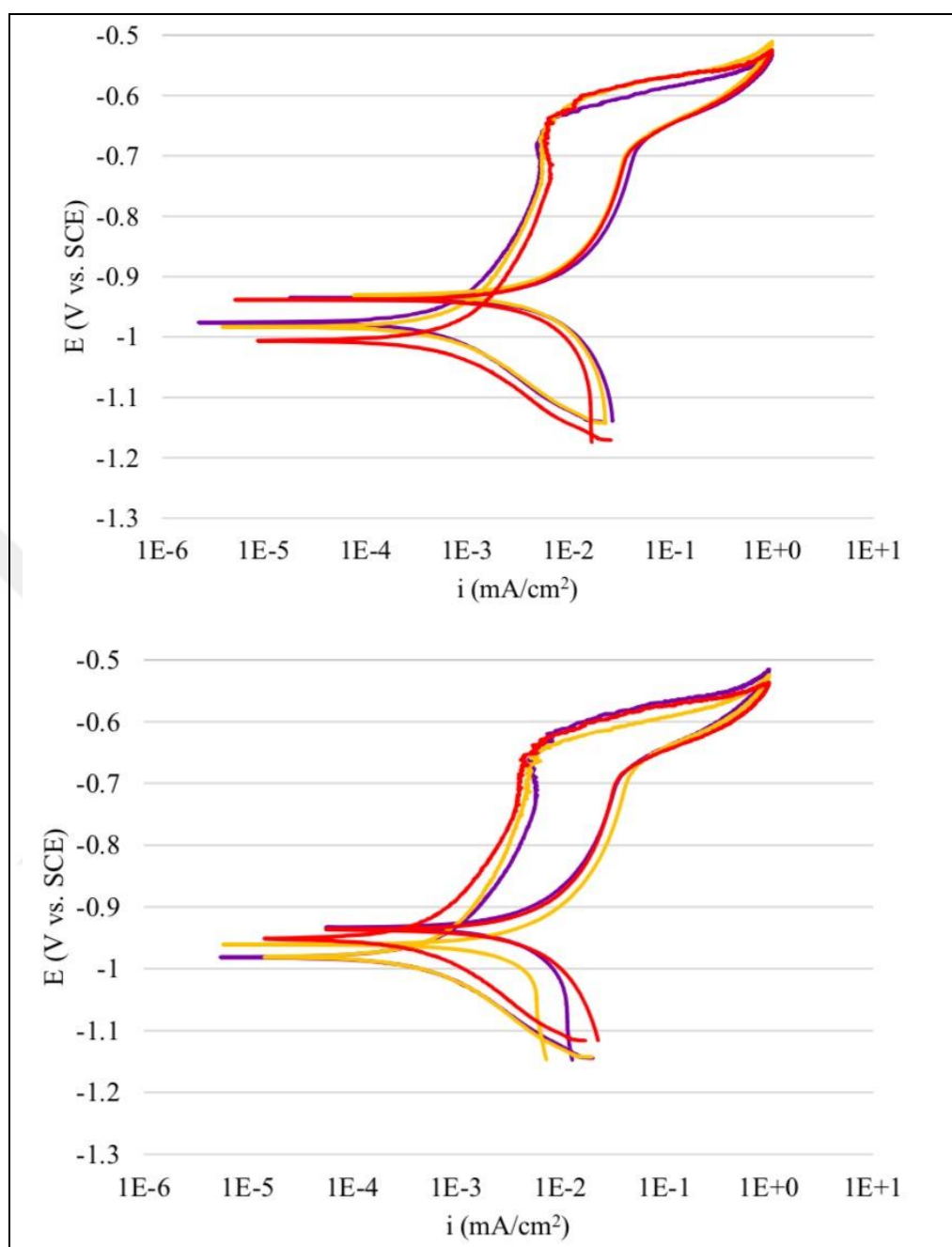


Figure A.5. CPP curves of DCC alloy sheets in 0.01 M NaCl solution



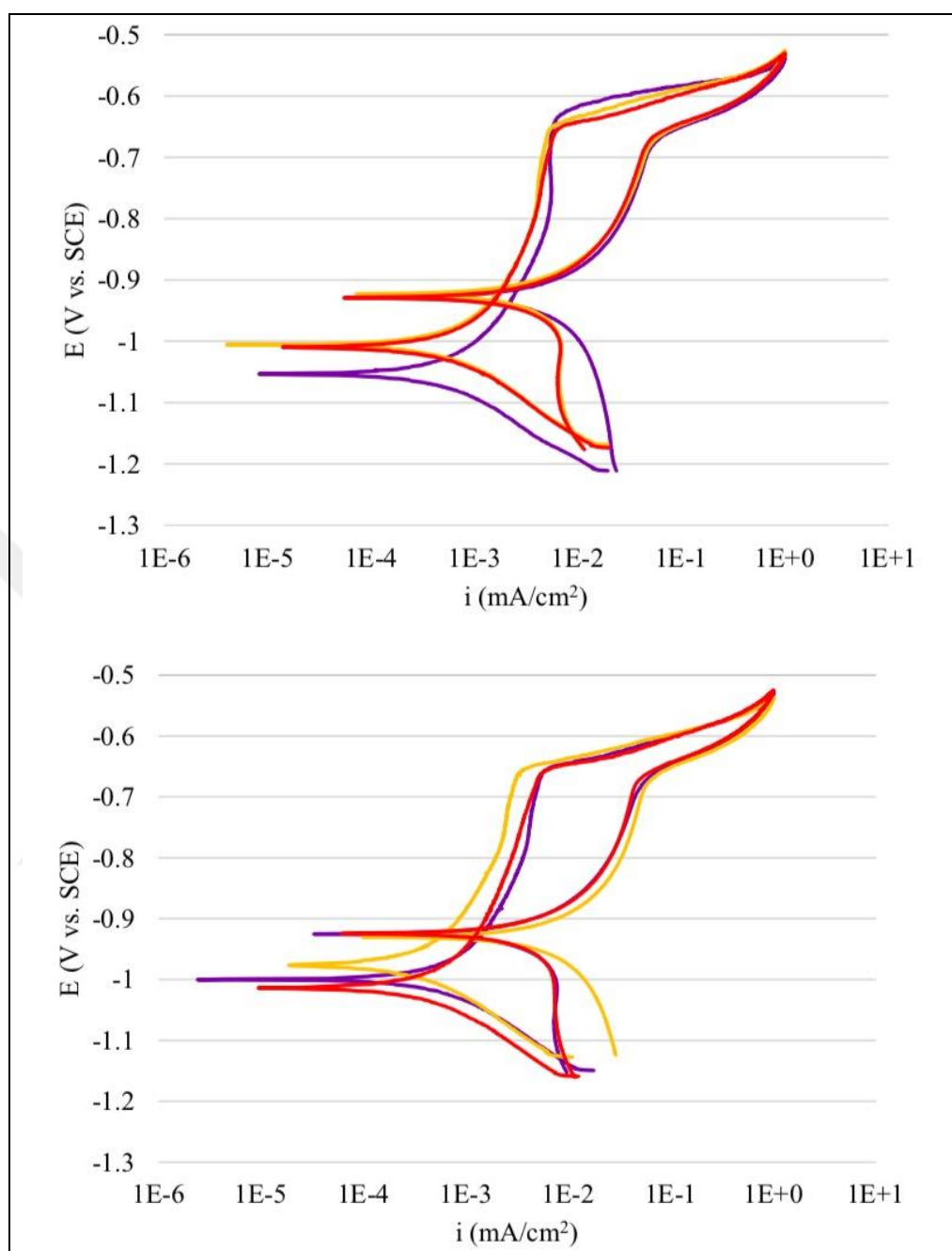


Figure A.6. CPP curves of TRC alloy sheets in 0.01 M NaCl solution

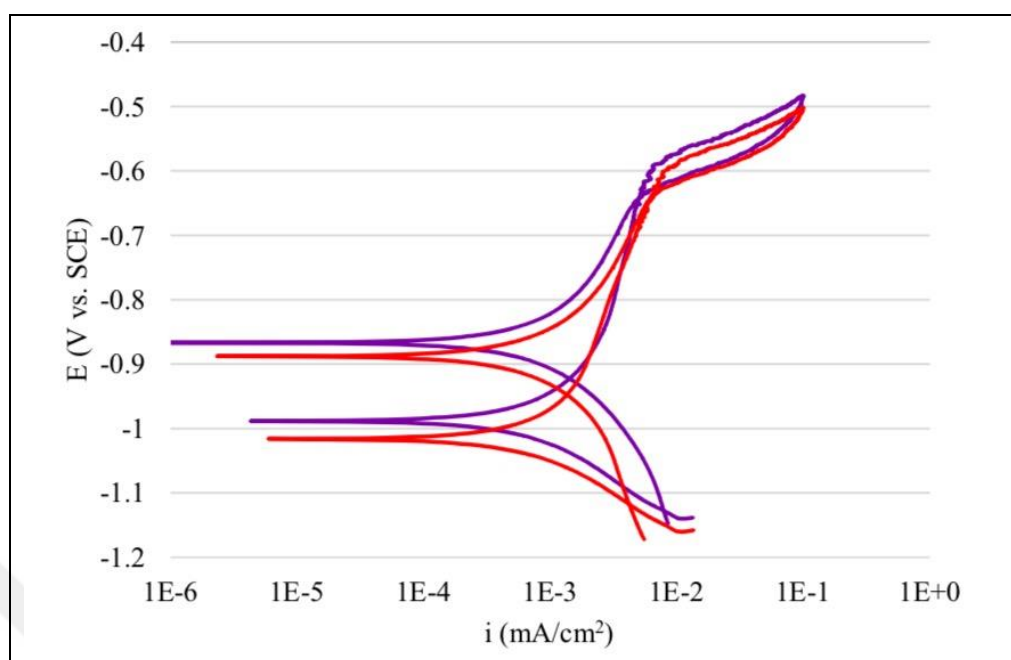


Figure A.7. CPP curves of DCC alloy sheets in 0.001 M NaCl solution

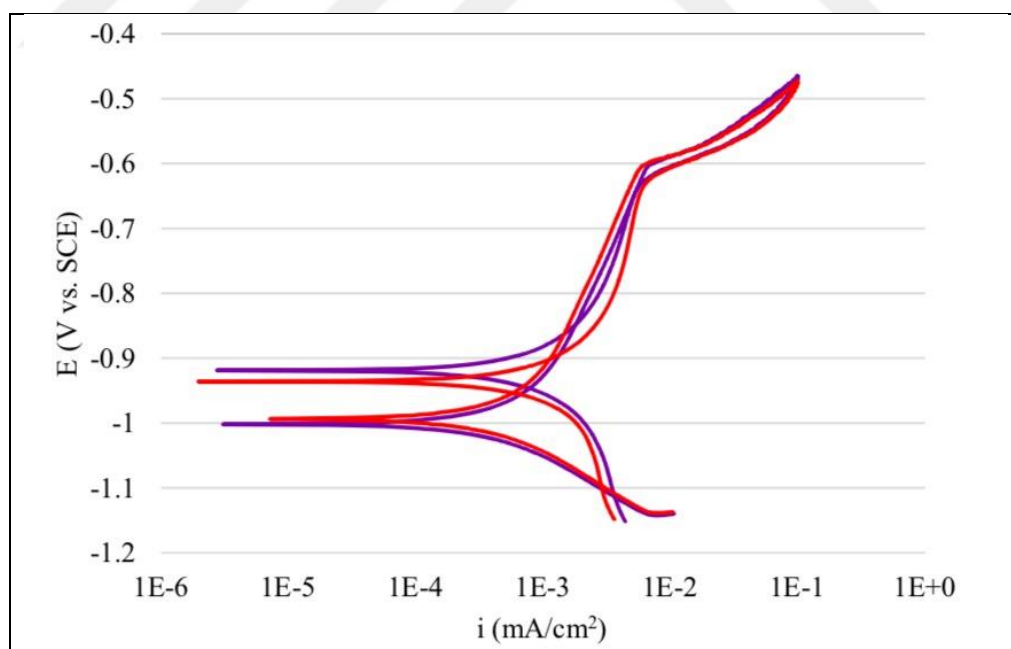


Figure A.8. CPP curves of TRC alloy sheets in 0.001M NaCl solution

## APPENDIX B: GRAPHICS FOR GALVANO-STAIRCASE CYCLIC POLARIZATION (GSCP) MEASUREMENTS

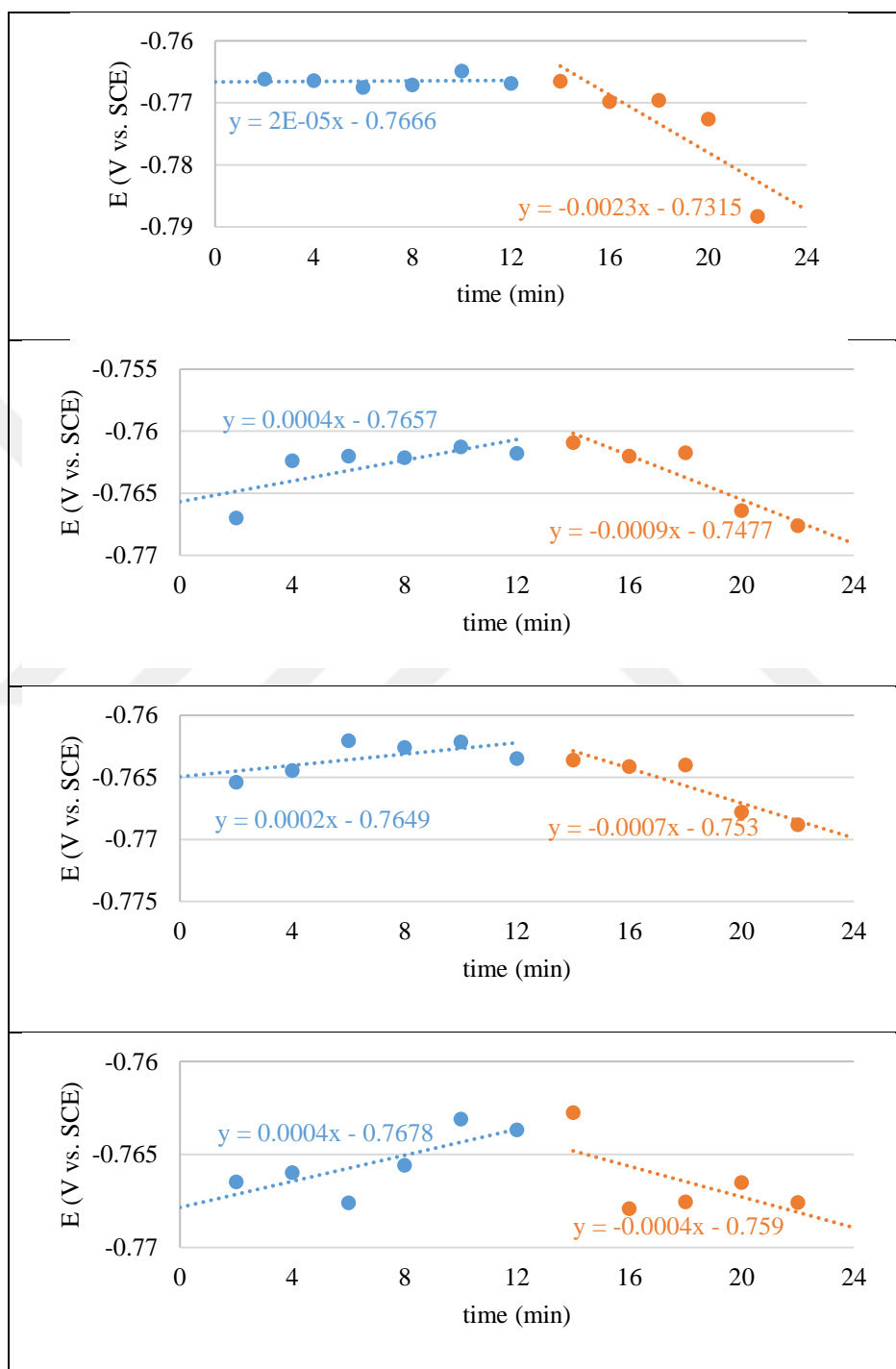


Figure B.1. GSCP results for DCC alloys in 1 M NaCl solution

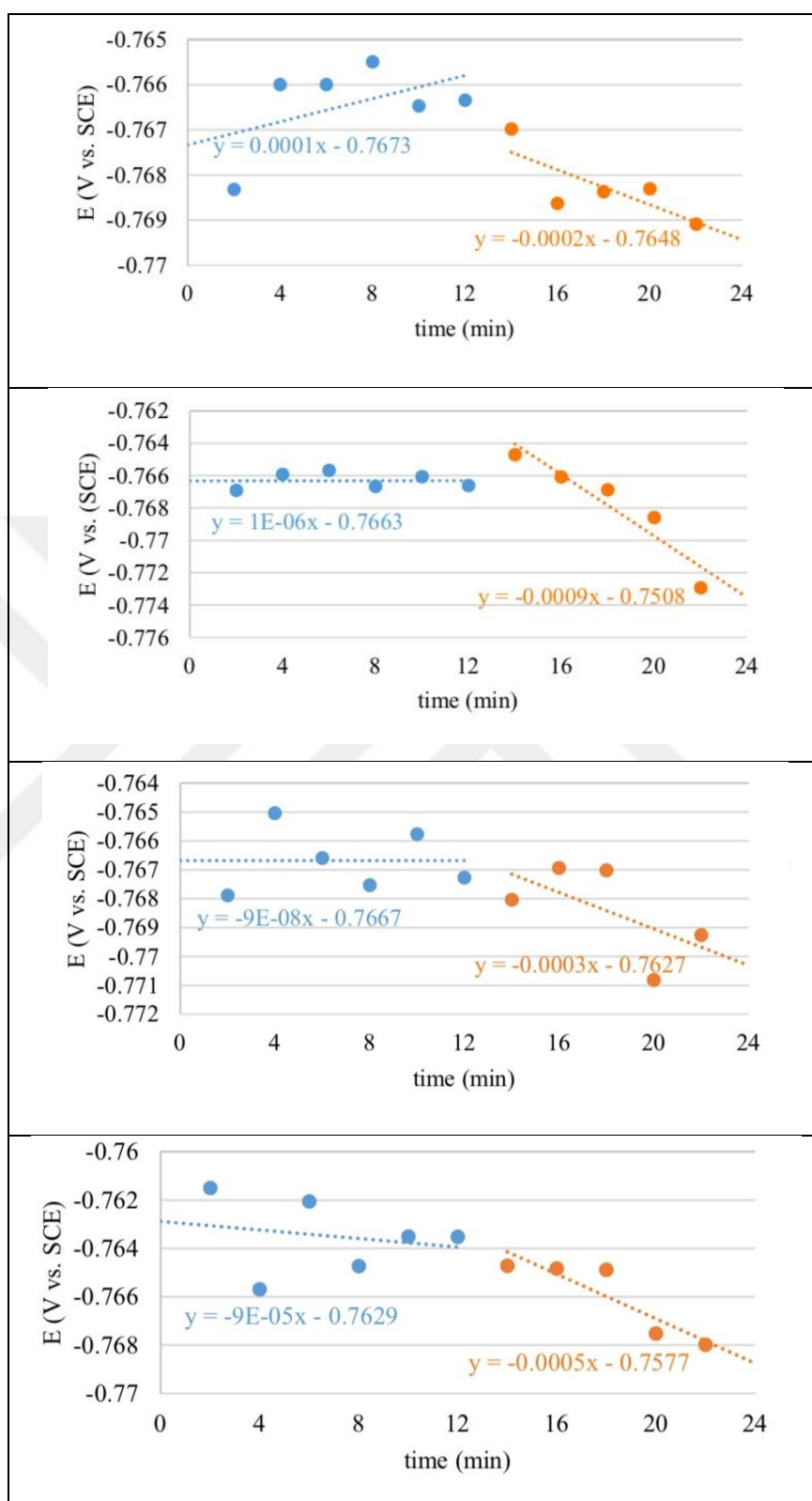


Figure B.2. GSCP results for TRC alloys in 1 M NaCl solution

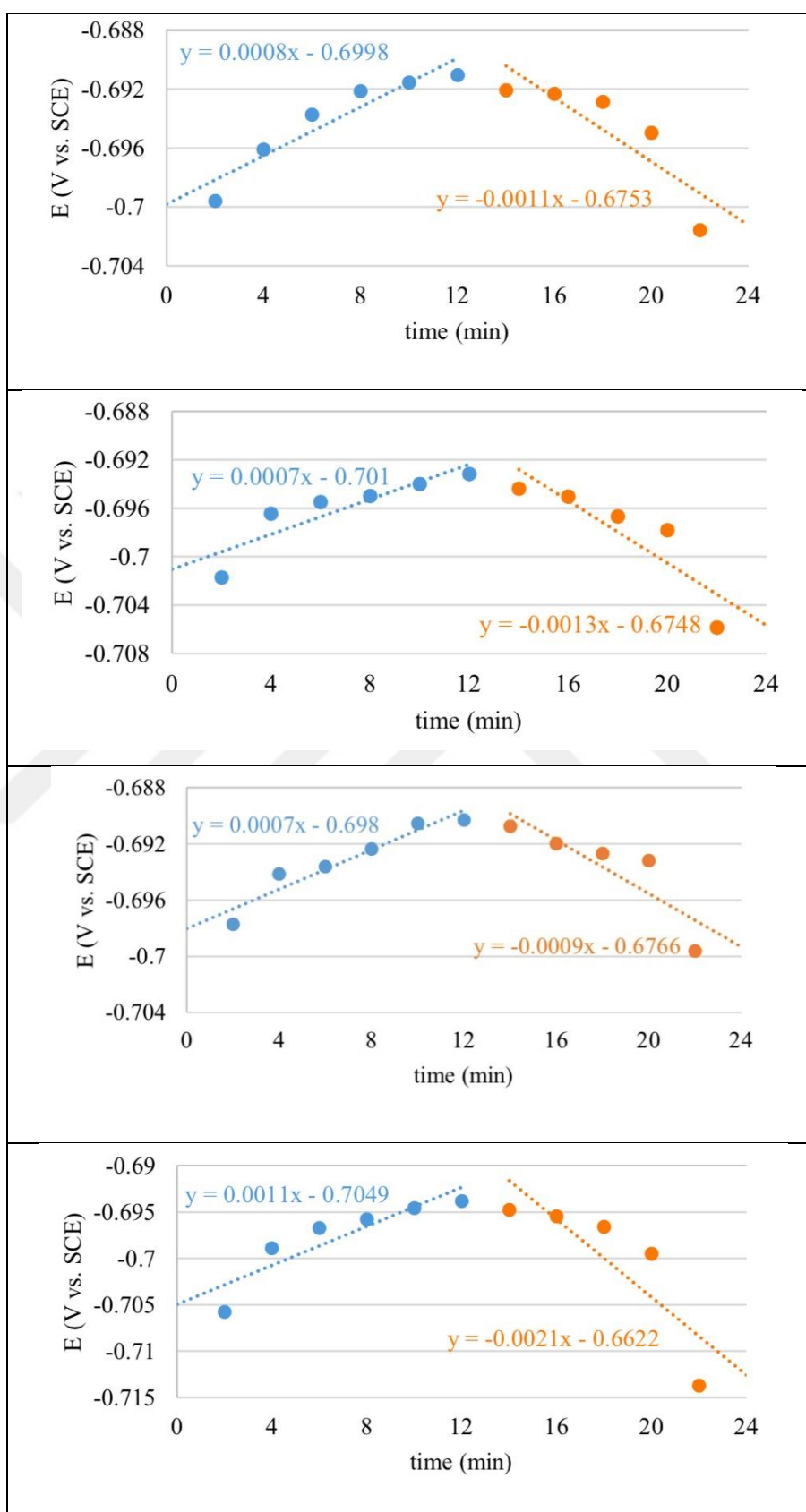


Figure B.3. GSCP results for DCC alloys in 0.1 M NaCl solution

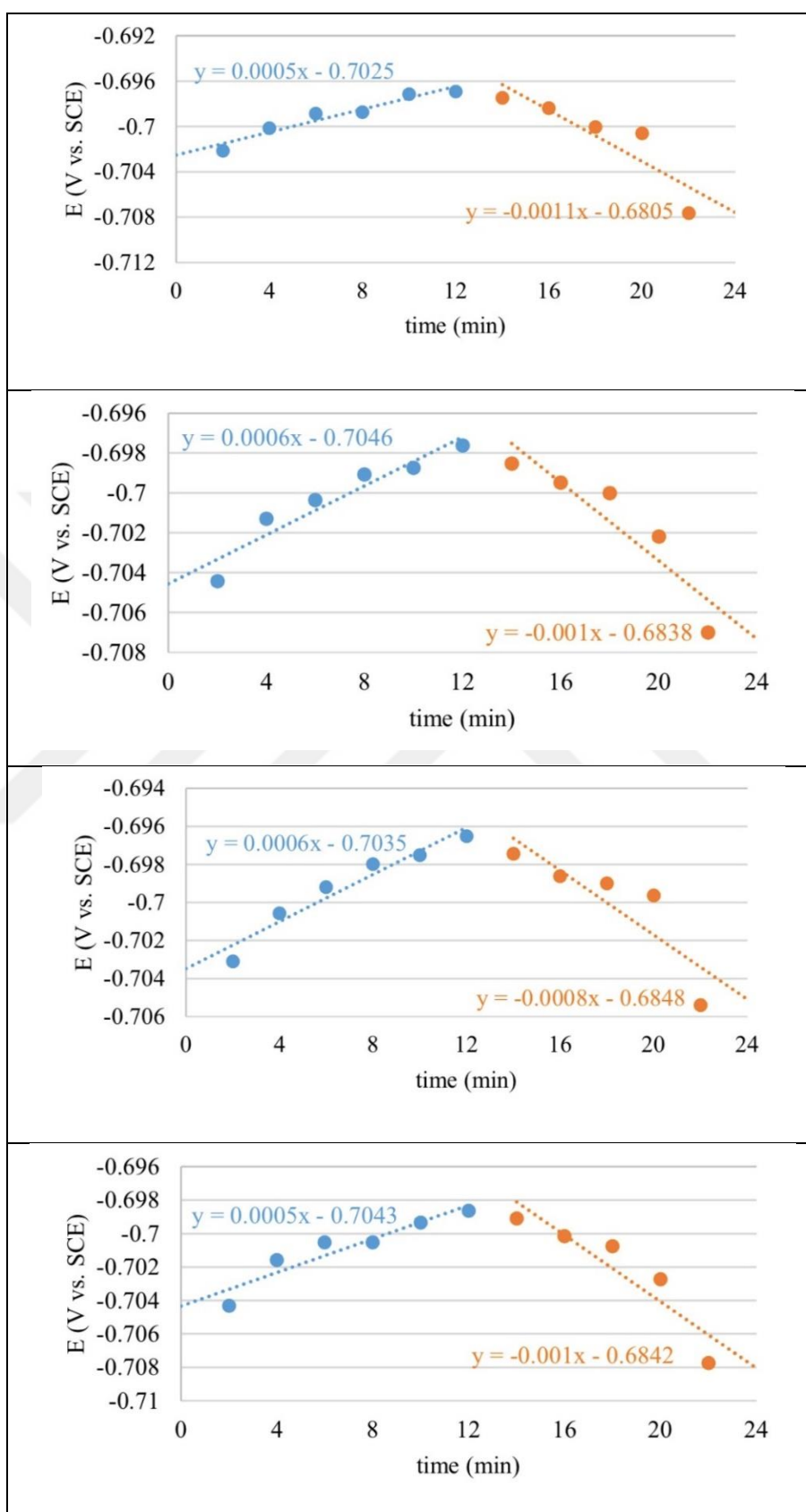


Figure B.4. GSCP results for TRC alloys in 0.1 M NaCl solution

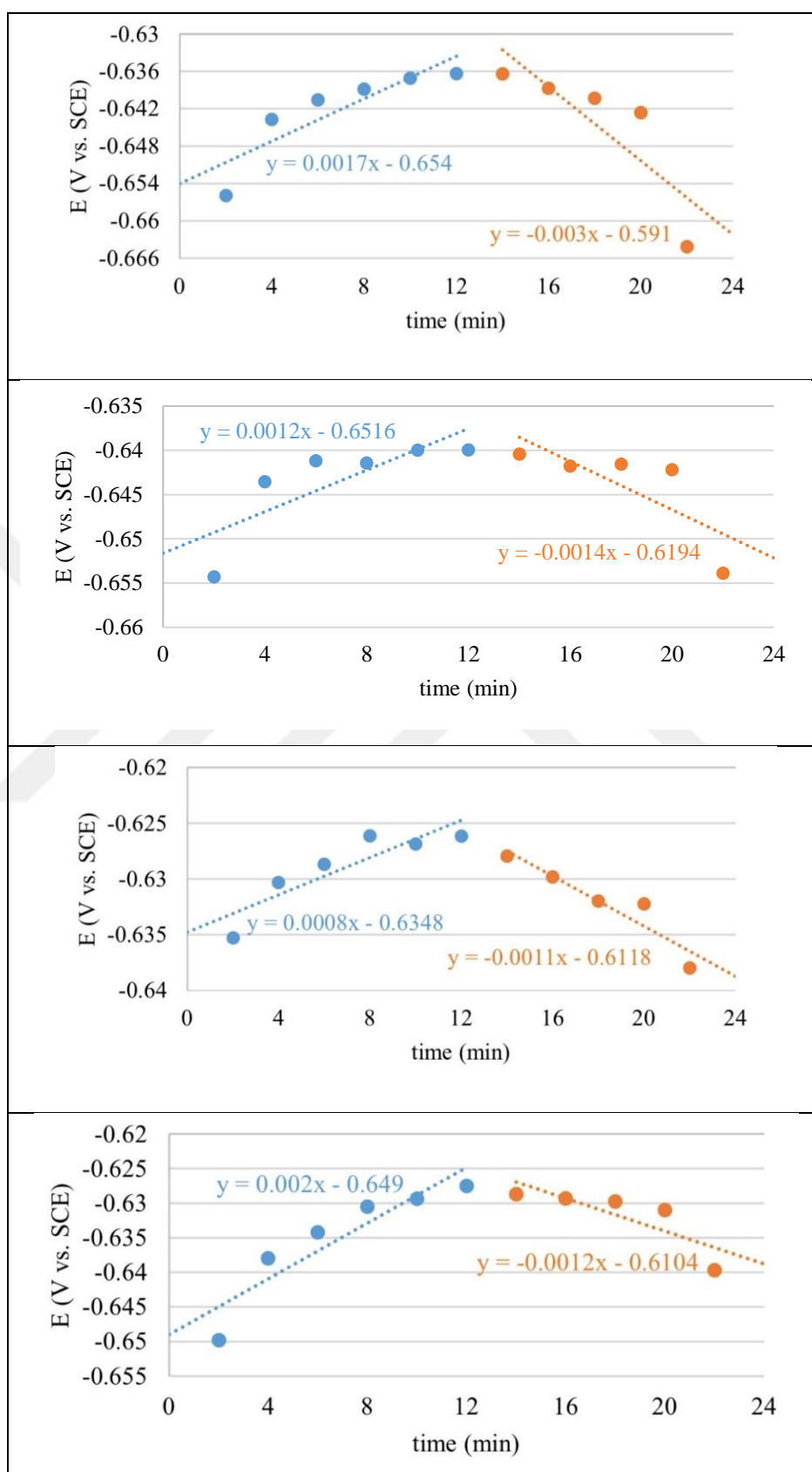


Figure B.5. GSCP results for DCC alloys in 0.01 M NaCl solution

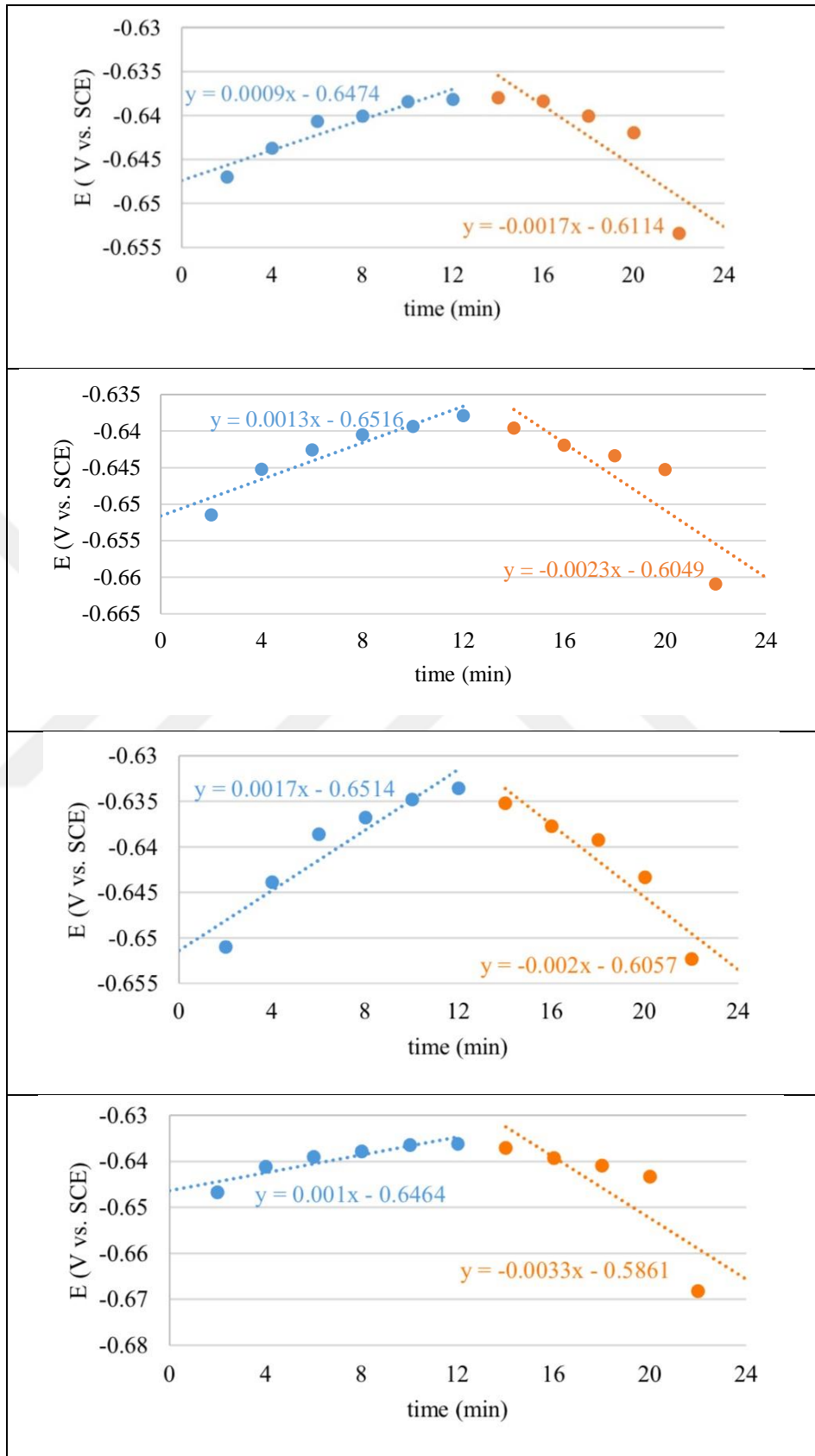


Figure B.6. GSCP results for TRC alloys in 0.01 M NaCl solution



## APPENDIX C: RESULTS FOR METASTABLE PITTING CORROSION MEASUREMENTS UNDER POTENTIOSTATIC CONDITIONS

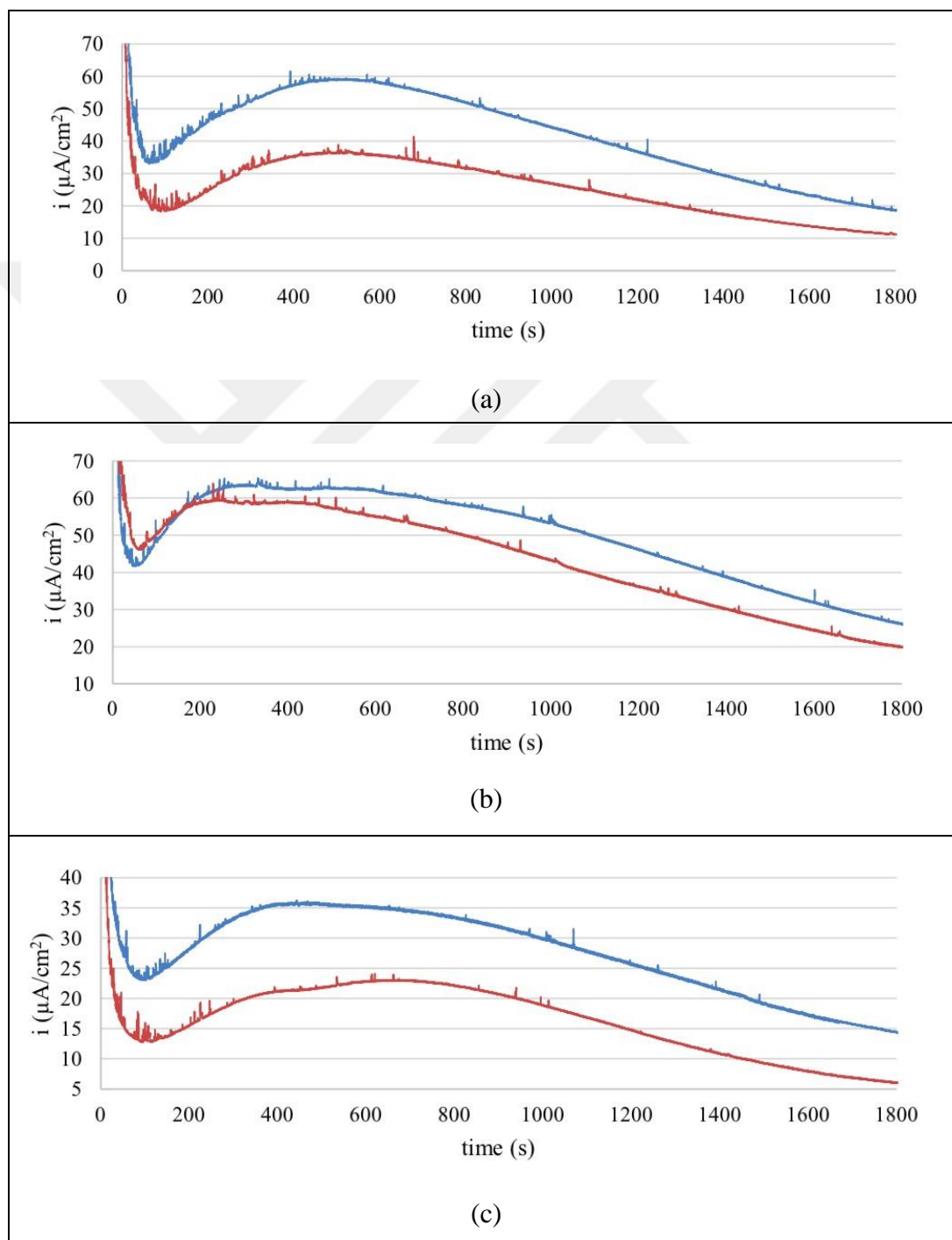


Figure C.1. Metastable pitting corrosion measurement results for DCCalloy in 0.01 M NaCl solution (a) -50 mV (b) -75 mV and (c) -100 mV below  $E_{\text{pit}}$

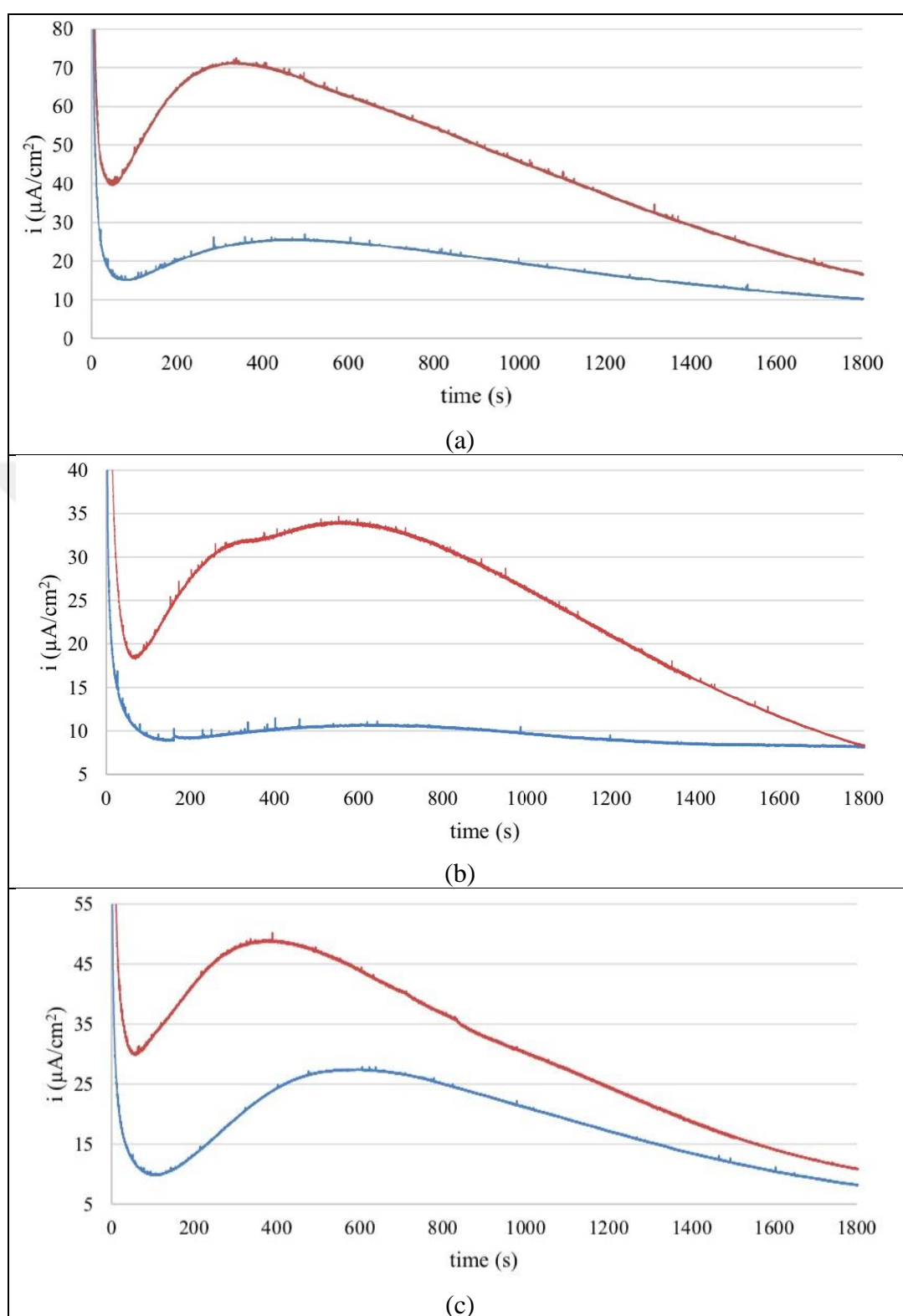


Figure C.2. Metastable pitting corrosion measurement results for TRC alloy in 0.01 M NaCl solution (a) -50 mV (b) -75 mV and (c) -100 mV below  $E_{\text{pit}}$

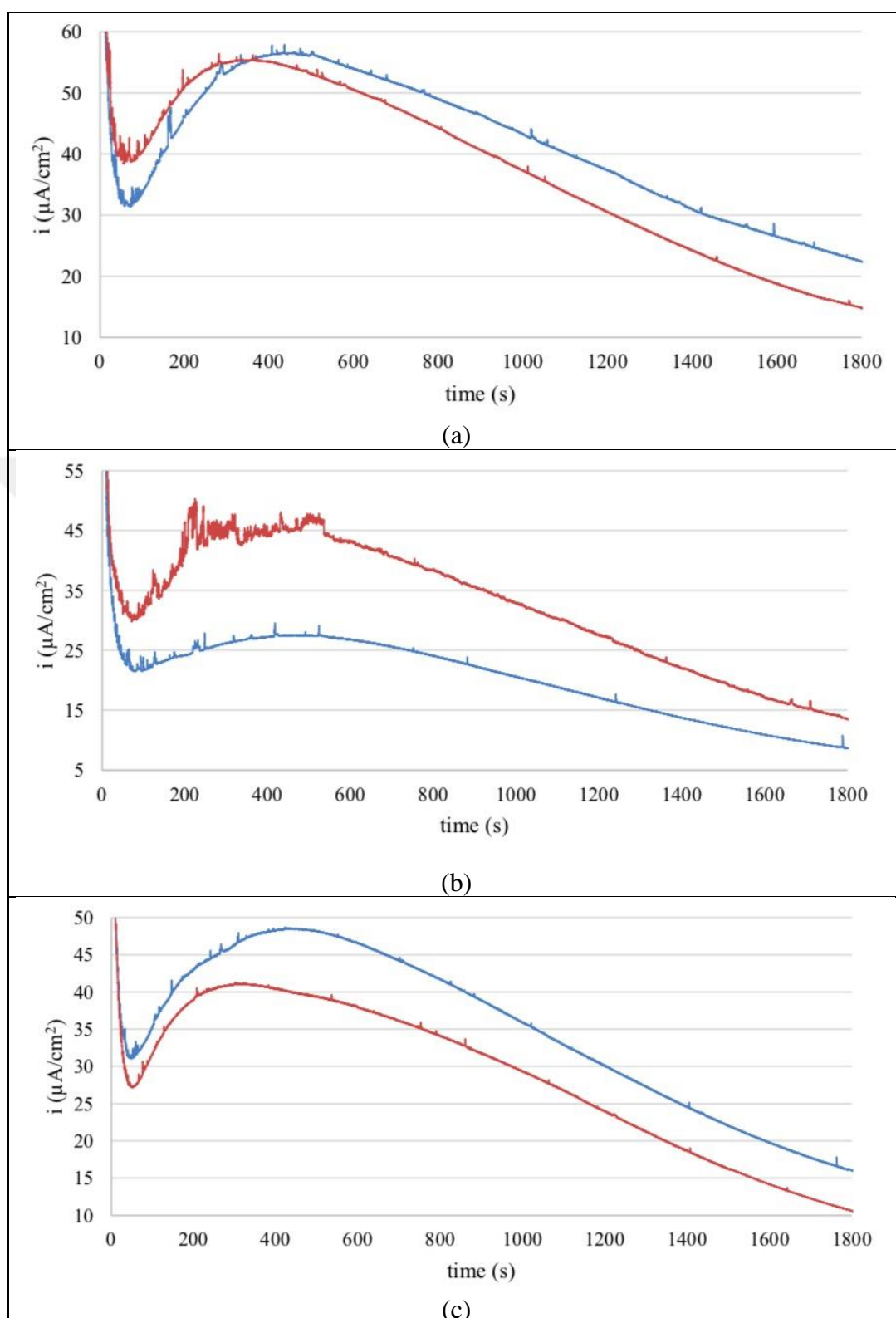


Figure C.3. Metastable pitting corrosion measurement results for DCC alloy in 0.001 M NaCl solution (a) -50 mV (b) -75 mV and (c) -100 mV below  $E_{\text{pit}}$

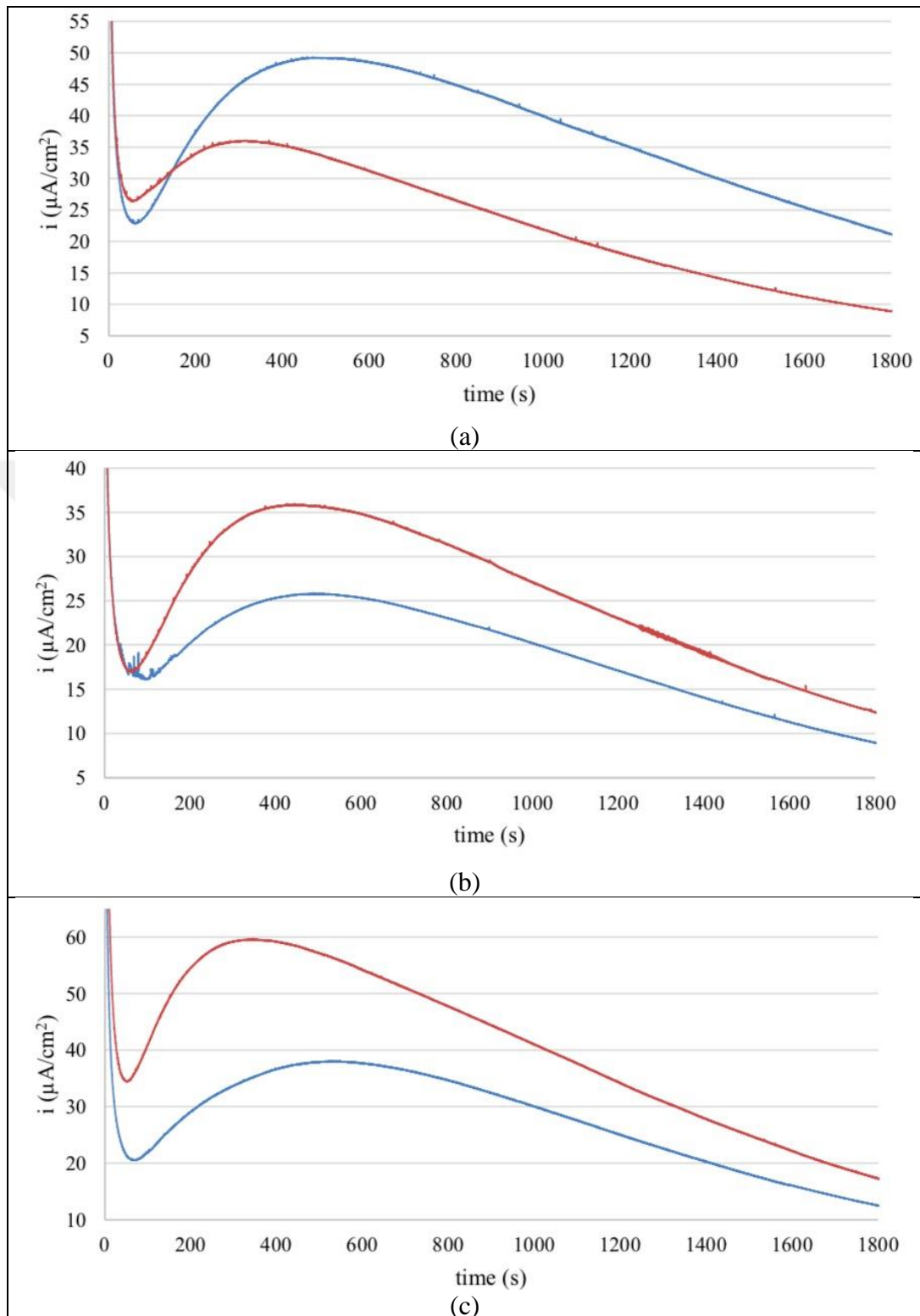


Figure C.4. Metastable pitting corrosion measurement results for TRC alloy in 0.001 M NaCl solution (a)  $-50$  mV (b)  $-75$  mV and (c)  $-100$  mV below  $E_{\text{pit}}$